Department of Precision and Microsystems Engineering

Temperature distribution modeling and novel filament clamp design of a hot-filament chemical vapor deposition setup

Joop Andriesse

Report no	: 2025.063
Coach	: Dr. J.G. Buijnsters
Professor	: Dr. J.G. Buijnsters
Specialisation	: Micro and Nano Engineering (MNE)
Type of report	: Thesis
Date	: 11 September 2025

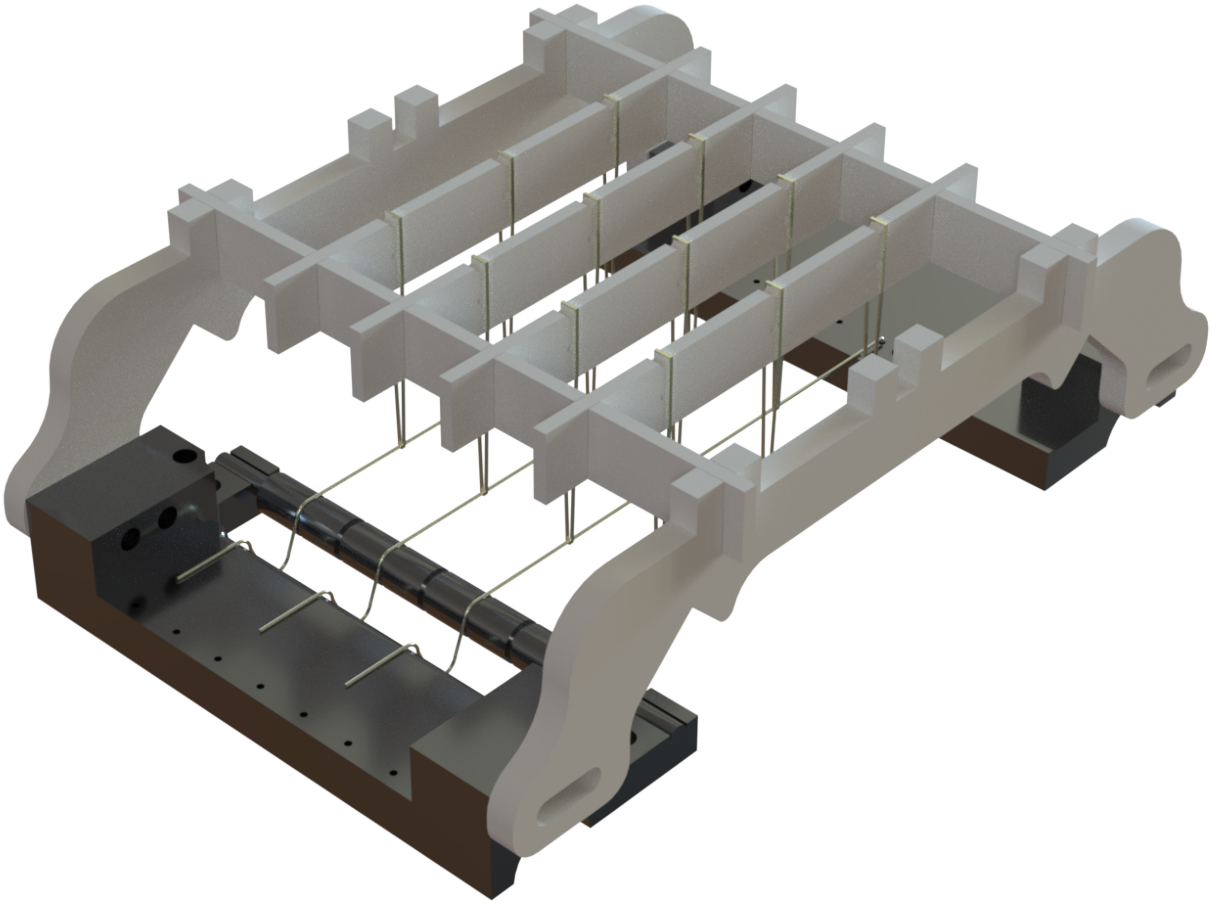

TU Delft Delft University of Technology

Challenge the future

Temperature distribution modeling and novel filament clamp design of a hot-filament chemical vapor deposition setup

Author:
Joop Andriesse
5367190

Thesis supervisor:
Dr. J.G. Buijnsters

Thesis commitee:
Dr. J.G. Buijnsters
Dr. A. Hunt
Dr. M. Kabatas

Precision and Microsystems Engineering department
The Netherlands
September 2025

Joop Andriesse : *Temperature distribution modeling and novel filament clamp design of a hot-filament chemical vapor deposition setup* (2025)
An electronic version of this thesis is available at `http://repository.tudelft.nl/`

I acknowledge the use of ChatGPT (`https://chat.openai.com/`) to proofread my work. I used it to check grammar and spelling, as well as to assist in generating LaTeX figures and tables. All outputs were subsequently reviewed and modified to better reflect my own style and intentions.

The work in this thesis was carried out in the:

Dept. Precision and Microsystems Engineering
Delft University of Technology

Supervisor: Dr. J.G. Buijnsters

I Acknowledgments

First, I would like to express my sincere graditude to my supervisor, Dr Ivan Buijnsters. His enthusiasm in teaching about diamond inspired me to take on this project. Troughtout the project, he offered plenty of constructive feedback on my work, which allowed me to better myself as a student. I am truly grateful for the opportunity to work with him as a supervisor.

I would also like to thank the technical staff of the Department of Precision and Microsystems Engineering, in particular Gideon Emmaneel and Bradley But. Gideon's advice on manufacturing and his help with ordering the custom ceramic parts were essential to the progress of this work. Bradley, in turn, was always around to give explanations on practical stuff regarding the reactor.

My gratitude also extends to the scientists and students of the dept. Precision and Microsystems Engineering. The weekly lunch meetings provided a great opportunity for inspiration and discussion. The opportunity to present in front of them twice was not only an excellent opportunity to improve my presentation skills but also to receive insightful feedback and suggestions.

I am equally thankful to my fellow MSc students for their companionship and encouragement during my time in Delft. Studying together provided motivation, and witnessing their progress inspired me to keep improving my own work. Our shared experiences made this journey especially meaningful.

Finally, I must express my gratitude to my parents, my girlfriend, and my sister for providing continuous support and encouragement throughout my studies. Their patience, understanding, and willingness to listen whenever I faced challenges in my studies and in this thesis meant a lot to me.

Joop Andriesse
Houten, September 2025

II Abstract

Hot-filament chemical vapor deposition (HFCVD) has become the commercially most widely used technique for producing diamond thin-film coatings due to its scalability and relatively low cost. Maintaining the geometrical stability of the hot filament, however, is challenging since filament deformation varies the distance between the filament and the substrate. This study presents a dual optimization strategy for a newly developed HFCVD reactor, combining mechanical stabilization with computational modeling.

Multiple novel hot filament clamp concepts were explored. From this, a novel hot filament clamp using tungsten support loops suspended from alumina (Al_2O_3) crossbeams was designed. Thermal simulations confirmed its feasibility, with alumina components reaching a maximum of 1250 °C, safely below the working temperature of this ceramic. 3D-printed prototypes allowed for the use of tab-and-slot connections with slight tolerances. The clamp was ultimately manufactured and assembled, although reactor maintenance prevented experimental evaluation of its influence on diamond deposition.

Hereafter, a COMSOL Multiphysics model of the reactor was developed. The substrate temperature distribution is modeled as a function of deposition parameters. Achieving more even substrate temperature distributions is beneficial for diamond quality. Parametric sweeps of key deposition parameters revealed that filament-filament spacing (D) had the strongest influence on substrate temperature uniformity. When $D < 8.25$ mm, the temperature range across the substrate increases. In contrast, when $D > 8.25$ mm, the average substrate temperature decreases, and the amplitude of periodic temperature fluctuations grows. Additionally, simulations of sagged filaments showed a significant increase in standard deviation of substrate temperature, from $\mu = 3.67$ °C to $\mu = 5.33$ °C, highlighting the importance of maintaining filament geometry.

This work provides a mechanical solution to filament sagging and a framework for optimizing reactor parameters through simulation. The findings offer a pathway towards scalable, high-quality diamond film deposition in this setup.

Contents

1 Introduction

Diamond thin films have attracted attention because of their exceptional mechanical, thermal, and chemical properties, making them useful in both scientific and industrial applications. These include wear-resistant coatings, heat sinks, optical windows, and more. Hot-filament chemical vapor deposition (HFCVD) is a widely recognized technique for synthesizing polycrystalline diamond films. It offers several advantages to other diamond synthesis methods in terms of low-cost equipment and scalability.

Despite its advantages, HFCVD faces several issues that limit its performance and reliability. One issue is filament degradation and sagging during prolonged deposition runs. Filament sagging alters the filament-substrate distance, leading to non-uniform temperature and gas phase activation distributions across the substrate surface. This non-uniformity negatively influences diamond film quality and growth rate. Additionally, the reactor operating conditions, which include high temperatures and reactive gas environments, lead to filament carburization. Filament carburization can lead to premature mechanical failure, further reducing process stability and reliability.

To address this issue, a novel filament clamping mechanism was designed. This design was developed by comparing various concepts through thermal simulations and component prototypes. The final filament clamp utilizes tungsten loops to support the hot filament at several points, minimizing the sagging effect. The clamping mechanism was built out of alumina (Al_2O_3) 99.7%, but has yet to be tested.

Due to the inability to test the new clamping mechanism experimentally, another way to optimize the HFCVD setup was approached. Digital modeling tools offer a powerful approach to predict and optimize thermal and flow conditions inside the reactor. By developing a multiphysics simulation model of the specific reactor using COMSOL, deposition parameters can be optimized without the need for extensive experimental trials. Parametric sweeps for filament spacing, radius, and substrate heating power have been performed. Furthermore, the impact of filament sagging on substrate temperature distributions was modeled and interpreted.

The remainder of this report is structured as follows. Chapter 2 provides a literature review on diamond properties, synthesis methods, and HFCVD reactor design principles. Chapter 3 defines the research focus, including the problem statement, objectives, and research questions. Chapter 4 includes the methodology, explaining the design of the new clamp and the setup of the COMSOL simulations. Chapter 5 offers results and discussion. The final clamp is presented, along with the simulation results. Finally, Chapter 6 concludes the thesis with key findings and recommendations for future work.

2 Literature review

2.1 Diamond

This subsection introduces diamond as a material, starting with a comparison of its microstructure to that of graphite. It then explains how these structural differences give rise to diamond's unique properties. Finally, this part explores key applications of thin-film diamond across various industries.

2.1.1 Structure of diamond and graphite

Graphite and diamond are allotropes of carbon, by explaining the difference between them, the extraordinary properties of diamond can be explained. In diamond, a carbon atom is bonded to four other carbon atoms, while in graphite, a carbon atom is bonded to three other carbon atoms. The tetrahedral bond of diamond is 3-dimensional, with an angle of 109.5 degrees between the atoms. While the graphite's trigonal structure is planar, with a 120-degree angle between the atoms [1].
Diamond is sp^3 hybridized, and the sp^3 structure consists of strong σ bonds. Graphite is sp^2 hybridized, consisting of both σ and π bonds. The unit cell of crystalline diamond, illustrated in Figure 1a highlights the tetrahedral bonding of sp^3 hybridized carbon atoms. Due to its high atomic density, diamond possesses superior physical properties, it has the highest hardness of all known materials and has the lowest coefficient of thermal expansion. Diamond is an insulator, it does not conduct electricity well. The electrons in diamond are localized, which means that they are stuck to the atom that they are bonded to. Furthermore, an ideal crystalline diamond has a clean band gap with no gap states. The wide band gap of 5.5 eV makes crystalline diamond optically transparent to a large optical spectral range. The chemical inertness and wear resistance can also be attributed to the strong covalent bonds between atoms in sp^3 hybridization. Diamond is a metastable form of carbon at room temperature, however, the high activation energy from diamond to graphite ensures that diamond remains stable [2].
Graphite's crystal structure consists of a layered and planar structure which can be seen in Figure 1b, bonding between the hexagonal layers consists of weak van der Waals forces. In graphite the atoms on a plane are bonded covalently, while the electron at the fourth bonding site remains free to migrate on the plane, this makes graphite electrically conductive in plane. But poor at conducting in the direction perpendicular to the plane. Graphite is a highly anisotropic solid, and carbons most stable form under standard conditions [2].

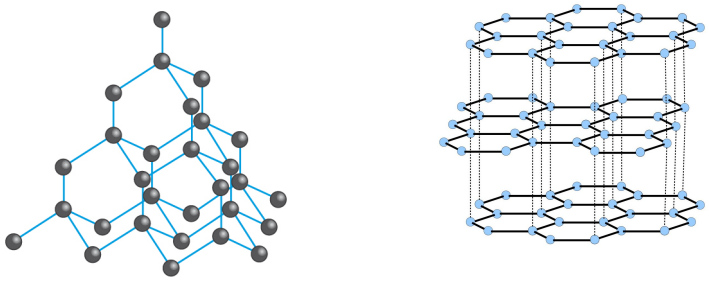

(a) Diamond crystal structure [3].

(b) Graphite crystal structure [4].

Figure 1: Comparison of (a) Diamond and (b) Graphite crystal structures.

To conclude, diamond is a material with a variety of applications due to its remarkable properties. Its first use was, and still is, as a gemstone. Throughout history, diamonds have been a status symbol due to its scarcity, hardness and bright sparkle. The fact that it is the hardest material, has the highest thermal conductivity and is chemically inert also makes it interesting for engineering applications [5]. Table 1 lists the relevant properties of diamond.

Table 1: Diamond properties [6].

Property	**Value**	**Units**
Hardness (Vickers)	$4.2e3 - 4.9e3$	HV
Density	3440-3580	kg/m^3
Thermal expansion coefficient	0.0000011	/K
Thermal conductivity	900-2320	W/mK
Transparency	Optical quality	
Electrical resistivity	$1e20 - 1e22$	$\mu\Omega \cdot cm$

Doped diamond. Perfect, impurity-free diamond consists solely of carbon atoms and is a colorless, large band gap material. However, the growth environment or post-growth conditions may introduce impurities into the material. Due to the large atomic density of diamond, it is difficult to fit larger atoms into the lattice. Boron, nitrogen, phosphorus, nickel, and silicon have been found in lattice sites. These defects can change the electrical, optical, thermal, and structural properties of diamond, making it possible for lab-grown diamonds to alter properties [7].
Natural diamond cannot be used as an electrode material due to the fact that it is a very wide band gap semiconductor. Introducing charge materials into diamond can make it conductive. Most often, boron is used for this. Boron has one less electron than carbon while also having a small atomic radius, this makes it relatively easy to incorporate as a charge acceptor. Boron-doped diamond (BDD) has several advantages in comparison to other electrode materials like gold, platinum, and glassy carbon. It has the largest electrochemical potential window for aqueous and non-aqueous media. Additionally, it offers bio-compatibility, a broad electromagnetic transparency window, low magnetic susceptibility, and tunable electrochemical properties by boron concentration [8].

2.1.2 Applications

Today, as many as 100 commercial companies fabricate diamonds for gemstone or other applications. As a result, the cost of diamonds has fallen rapidly over the past decade. In 2024 the typical cost of a freestanding (4 x 4 x 0.5 mm) single-crystal diamond is $\sim$ 2000$, while a bigger (10 x 10 x 0.5 mm) polycrystalline sample is valued as low as $\sim$ 50-200$ depending on quality [9]. This decrease in cost resulted in diamonds becoming a viable material for commercial applications. The following examples exploit the extraordinary properties of diamond or doped diamond thin films:

Hardness - Cutting tools.
Diamond's exceptional hardness makes it ideal for fabricating cutting tools. In most cases, diamond is deposited directly onto a substrate, a technique frequently researched and now widely used in commercial applications. One notable example is the deposition of diamond on hard metal (WC-Co) substrates [10]. Diamond-coated cutting tools offer significant advantages over conventional hard metal tools, including longer lifespan, faster cutting speeds, and superior surface finishes. However, a key limitation of diamond cutting tools is their reactivity with iron, making them unsuitable for cutting ferrous metals like steel [11].

Thermal conductivity - Electronics.
The high thermal conductivity and electrical insulation make diamond a great packaging material for semiconductors [10]. It can even be used as a substrate material for multi-chip modules or submount for integrated circuits. Resulting in higher speed of operation, because devices can be packed more tightly without overheating. [11]

Boron doped diamond (BDD) - Electrochemical applications.
Doped diamond films can be used for electrochemical applications, they can be used in harsh or corrosive environments. Conventional electrode materials like Platinum cannot be used in water, because it dissociates. However, BDD has a very large potential window in water, which means they can be used to analyse contaminants in water, measure PH levels and even detect bio-potential changes in plants[8].

Transparancy - Optics.
Diamond has a multi spectral-transparency, which means that it is transparent for a lot of wavelengths. This unique property combined with its hardness, chemical inertness, and mechanical properties make it a desirable material for optical windows. In practice they can be found in X-ray detector windows for scanning electron microscopy (SEM) and X-ray tubes [10]. Diamond optical windows are also used as infrared (IR) window in harsh environments. An example of a commercially available optically transparent diamond window is shown in figure 2. Where a diamond optical window, produced by XDS oxford and Fraunhofer institute is used in a harsh environment as a vacuum reactor window [12].

Figure 2: Optically transparent diamond window, produced by XDS oxford [12].

2.1.3 Diamond synthesis

Natural diamonds present challenges, including environmental and ethical concerns, as well as inconsistent quality control. This has led to the invention of several experimental techniques to synthesize diamond in a laboratory setting. This chapter will start with the carbon phase diagram, hereafter proceed with an explanation of high pressure synthesis techniques; detonation nanodiamond and high pressure high temperature diamond synthesis. After this low pressure low temperature chemical vapor deposition synthesis will be explained. Finishing with diamond morphology and characterization.

Carbon phase diagram. Figure 3 shows the carbon phase diagram, in which the different forms of diamond synthesis can be seen. The carbon phase diagram displays the thermodynamic stability for graphite and diamond at different pressures and temperatures. Theoretically and experimentally determined conditional phase boundary lines separate the diamond and graphite stability fields. It is evident that diamond also grows in a metastable regime, where its growth is not thermodynamically stable but can be kinetically favorable under specific conditions [5, 7].

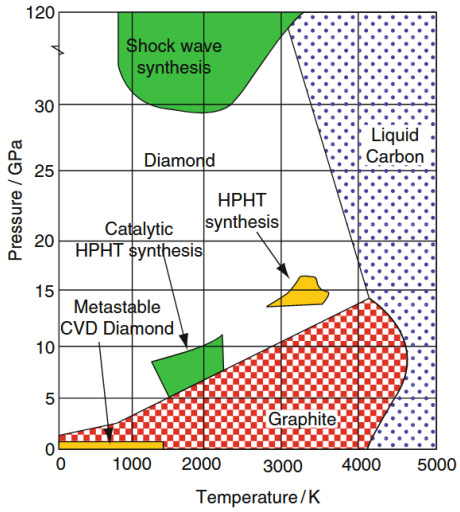

Figure 3: Carbon phase diagram, highlighting the temperatures/pressure ranges of various diamond synthesis techniques [5].

High pressure synthesis techniques. The first two diamond synthesis techniques that are discussed replicate the growth environment of natural diamond, high pressure and high temperature. In this way thermodynamically stable diamond can be created.

High pressure high temperature diamond synthesis (HPHT). The first technique that was developed to produce synthetic diamond was the HPHT growth technique. This technique replicates the natural creation of diamond by compressing graphite to high pressure and heating it to high temperature. Under the influence of a metal catalyst, it is then left until diamond crystallizes. These types of diamonds are commonly used in cutting tools and machining components, and recently found great traction in the jewelry market too. The downside of this technique is that it produces diamond in the form of single crystals ranging in size from nanometer to millimeters, which limits the range of applications. Therefore, a different approach based on low-pressure synthesis was developed in the second half of the past century. This allowed for diamond to be synthesized in thin layers, thereby enabling more applications [11].

Detonation nanodiamond. Diamond nanoparticles have a wide variety of applications, including lubricants, polishing materials and seeds for further Chemical vapor deposition diamond growth [13]. The detonation technique, also called shock wave synthesis, is the most common method for the large-scale production of nanodiamond. Carbon containing compounds are detonated in a metallic chamber under a combined atmosphere of N_2, H_2O and CO_2. Under extreme pressure and temperature, it reaches the Chapman-Jouguet (C-J) point, where carbon nanoclusters form as detonation products expand and cool. Controlled chamber pressure ensures the growth of nanodiamonds, yielding diamond soot composed of 75 wt% nanodiamonds and other carbon allotropes [14]. To purify the diamond soot different types of oxidation processes are used to remove the graphitic impurities. For example, Ardhayanti *et al.* [15] used a combination of salt-assisted air oxidation and Fenton chemistry to effectively purify the diamond soot.

2.1.4 Diamond chemical vapor deposition (CVD)

Diamond can also be synthesized in its metastable regime, by Chemical vapor deposition (CVD). Under CVD conditions, diamond growth is driven by kinetics and not thermodynamics. CVD is performed using a small fraction of carbon containing gasses ($< 5\%$) in an excess of hydrogen. These gasses are heated to temperatures above 2000K, this activation can be done with a variety of methods like thermal (hot wire), electric discharge (microwave) or combustion methods [16]. The reactant gases are typically activated at pressures between ca. 1 mbar and several hundreds of mbar to create many molecular, radical, and ionic species. The CVD process is illustrated in Figure 4. In this schematic, the reactants are introduced to a reactor with a certain pressure. The hot filament or plasma dissociate the reactants hydrogen and methane. Subsequently, the gas is transported to the substrate by forced flow, convection or diffusion. This substrate is maintained at a temperature between 600 and 1200 °C. Boundary layers with strong tem-

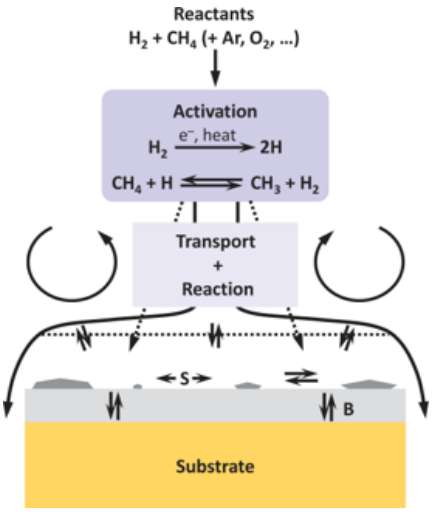

Figure 4: Schematic of the diamond CVD process [7].

perature and reactant gradients are then formed above the substrate surface. On the substrate surface, diamond growth will then occur [7].

Role of atomic hydrogen in CVD diamond growth. Atomic hydrogen is the most critical component in the gas mixture. In a CVD system, atomic hydrogen is created by decomposition of H_2 (eq 1).

$$H_2(g) \longrightarrow H + H \tag{1}$$

Hydrogen is responsible for the termination of 'dangling bonds', which are H atoms that need to be replace by carbon containing species. The large number of H atoms at the surface can bond these dangling H atoms and prevent graphitization. Additionally, atomic hydrogen can etch graphitic sp^2 carbon, while leaving diamond-like sp^3 carbon intact [11]. Furthermore, atomic hydrogen accelerates the gas phase reaction, and decomposes the carbon continaing gasses like CH_4 into active radicals [5] (eq 2).

$$CH_4 + H\cdot \longrightarrow CH_x + H_2 \quad (x = 1 \text{ to } 3) \tag{2}$$

As mentioned earlier, growth of CVD diamond is thus based on kinetics. The formation of diamond kinetically competes with the formation of graphite [17]. But the atomic hydrogen suppresses the formation of graphite, leading to diamond growth. A schematic of the resulting process can be seen in Figure 5. In which the stepwise addition of CH_3 is shown, leading to diamond growth. It starts with the reaction of atomic hydrogen with a surface H to form H_2 leaving behind a reactive surface site. Most often, this reactive surface site reacts with another H atom, returning it to its previous state. But occasionally a gas phase CH_3 radical reacts with the active surface, adding a carbon atom to the lattice. Another reaction of atomic H leaving behind a reactive surface can attack the newly formed nearby carbon group to form a ring structure, locking the two carbon atoms into the diamond lattice [11].

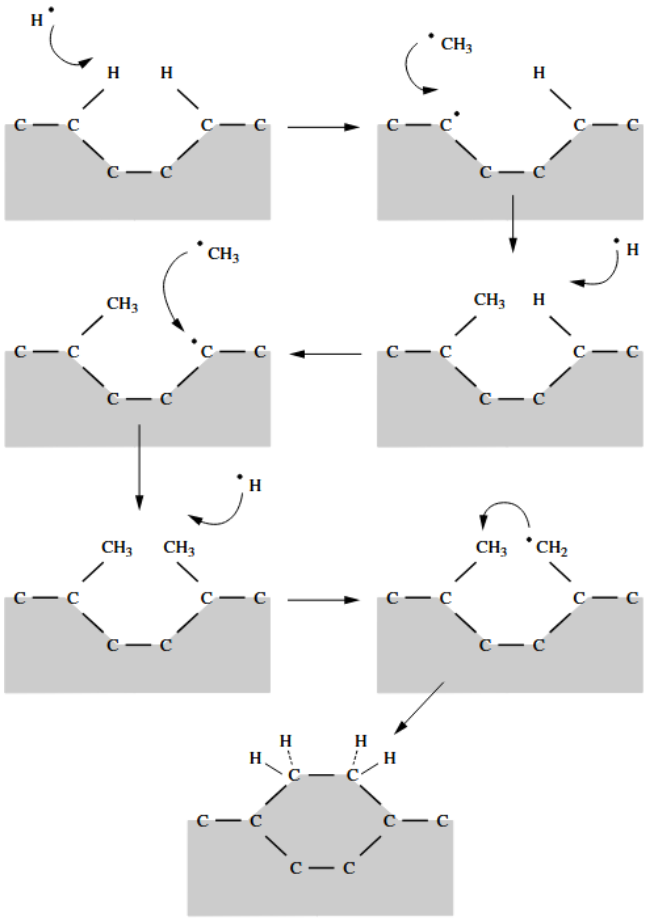

Figure 5: Reaction process at the diamond surface, leading to stepwise addition of CH_3 and diamond growth [11].

Hot filament chemical vapor deposition (HFCVD). The first type of CVD that will be discussed is HFCVD, an example layout is shown in Figure 6. Just like in other methods, a vacuum reactor is used in which the substrate is heated. The substrate lies a few millimeters beneath the hot filament, which is heated to excess of 2200 °C. Carbon containing gasses such as methane (CH_4) are passed over the hot filament, as well as additional hydrogen (H_2) gas. Pyrolysis of the gas mixture takes place resulting in the generation of diamond-forming active gas species, which upon reaching the substrate surface, maintained at 700–900 C°, is kept at a distance of about 8–10 mm from the hot filament to a form a diamond film.

The hot filament is made of a metal that can sustain these harsh circumstances and will not react significantly to the process gas, most commonly used are metals like tungsten (W) and tantalum (Ta). However, eventually the filaments will carburize under the influence

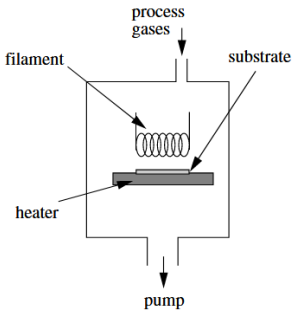

Figure 6: Example layout of a hot filament chemical vapor deposition (HFCVD) setup [11].

of the carbon-containing gasses. This carburization will change their resistivity, making them brittle and reducing their lifetime [11]

Microwave CVD. In Microwave CVD (MWCVD) the process starts with dissociation of raw gases, primarily hydrogen (H_2) and methane (CH_4), under microwave irradiation. This process creates atomic hydrogen and various carbon-containing species. The carbon radicals and atomic hydrogen will interact with the diamond substrate which will facilitate the growth of new carbon layers [19]. Figure 7 shows an example of a type of MWCVD setup called microwave plasma CVD (MPCVD). In this example, the discharge called a 'plasma ball' is generated above the substrate, which will provide the substrate heating. At the right microwave power, pressure and mass flows, MPCVD diamond growth will occur [18]. In recent year, MWCVD has become the most widely used deposition technique in China. The most used reactor is a so called 'top-hat' MWCVD reactor, capable of growing high-quality diamond at high rates [9].

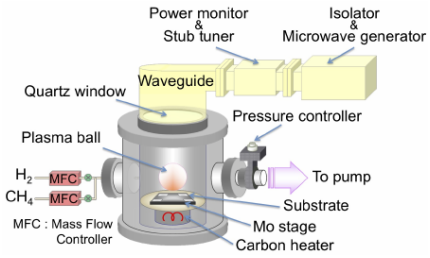

Figure 7: Schematic of a microwave plasma chemical vapor deposition (MPCVD) setup [18].

Scope and importance of HFCVD. Now that the two most widely used CVD methods have been briefly discussed, they can be compared. The HFCVD method is scalable, increasing the filament and substrate dimensions will allow for bigger areas of diamond growth. As mentioned earlier, HFCVD can be contaminated by metal inclusions from the filament. This leads to the fact that microwave plasma CVD diamond is generally of highest quality, but this technique is more expensive and harder to scale [20].
Nowadays, MWCVD is widely used in the production of artificial gemstones, due to its high growth rate and operational stability. On the other hand, HFCVD is extensively used in various industrial applications like hard-coating, thermal management and boron-doped diamond [21]. There have been concerns about using HFCVD diamond in electronic applications due to the possible metal impurities. However, recent studies [22] have shown that heavy boron doping can be achieved while maintaining high electrical activity. Additionally, other studies have shown a vast improvement in diamond growth rates, while maintaining high phase purity (sp^3) [23]. The combination of these improvements and the ability to produce diamond on wafer scale resulted in the focus on Hot-Filament Chemical Vapor Deposition in this literature survey.

2.1.5 CVD diamond morphology

Diamond produced by CVD can be either polycrystalline or single crystal, depending on the substrate used during growth. Single crystal diamond (SCD) is grown through homoepitaxial growth, which involves depositing diamond layers on a single crystal diamond seed. This process requires low pressure and high substrate temperatures. This type of growth is the preferred method in the semiconductor industry.
In contrast, polycrystalline diamond typically forms when growth occurs on a non-diamond substrate.

In this case, nucleation happens at multiple locations, leading to "island growth" that merges into a polycrystalline layer. This growth mechanism, known as Volmer-Weber (VW) growth, occurs when interactions between adatoms (adsorbed atoms) are stronger than their interactions with the substrate surface. This results in relatively rough films [16, 24].

Crystal shape. Most often, growth conditions lead to diamond crystal shapes with octahedral (111) or cubic (100) facets. However, at certain growth parameters a different unfaceted structure of diamond can be grown. These polycrystalline unfaceted structures are called ballas (or ball-shaped, cauliflower-like). Figure 8 shows an image of the different crystal shapes.

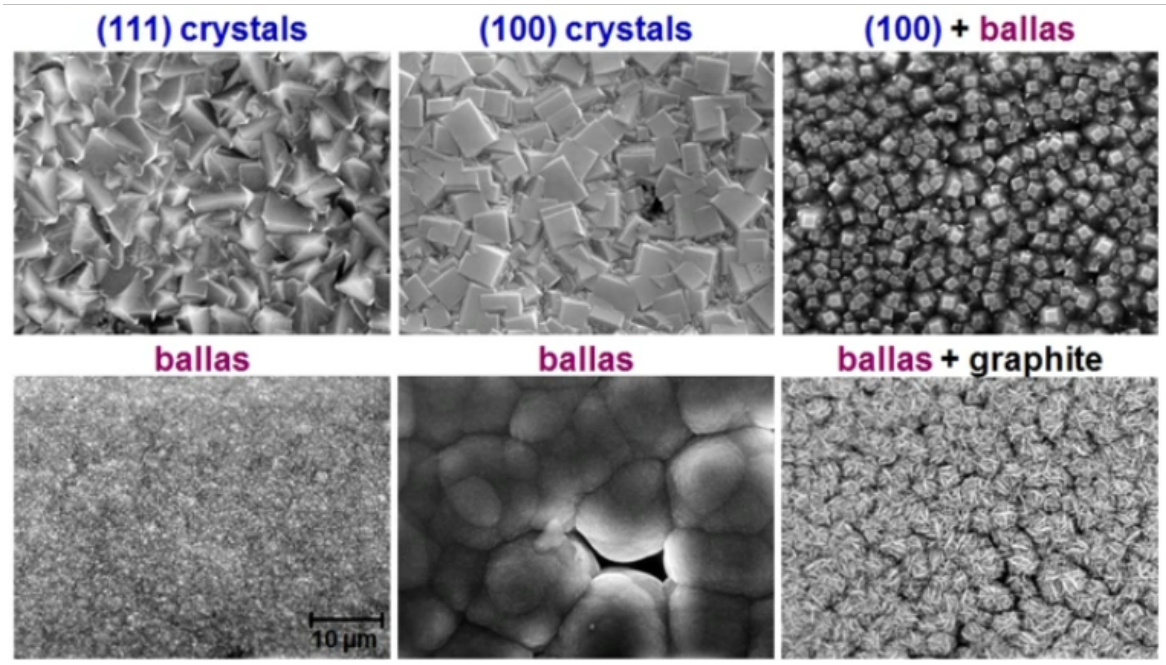

Figure 8: Different polycrystalline diamond morphologies [10].

Moreover, the morphology is dependent on growth parameters (Figure 9). At low plasma intensity and high carbon supersaturation, fine-grained aggregated deposit, frequently referred to as ballas. Increasing the amount of atomic hydrogen leads to the formation of coarser crystalline regions leading to (100) faceted crystals. Finally, further optimizing the growth parameters leads tot (111) faceted crystals to become dominant [10].

The CVD diamond crystal shape can be calculated by its growth parameter α. It is dependent on the ratio of the (100) and (111) growth rates. It is defined as equation 3, in which v_{100} and v_{111} are the growth rates on the (100) and (111) plane, respectively. For single crystals, α is 1, and for cubes 3. A value in between 1 and 3 results in cubo-octahedral shape.

$$\alpha = \sqrt{3}\frac{v_{100}}{v_{111}} \tag{3}$$

In polycrystalline diamond films, controlling α to be dominant in the (100) surface leads to smooth films. Moreover, the growth parameter α is closely related to the concentration of radical species and substrate temperature [25].

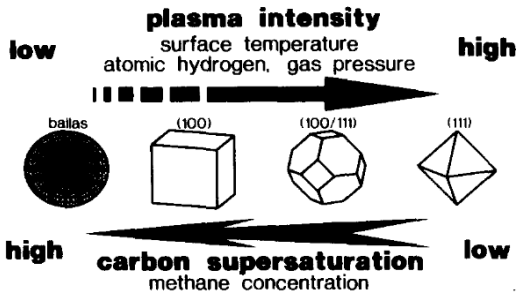

Figure 9: Influence of growth parameters on CVD diamond morphology [10].

Polycrystalline diamond grain size. The three distinct forms of polycrystalline diamond are: microcrystalline diamond (MCD), nanocrystalline diamond (NCD) and ultrananocrystalline diamond (UNCD). MCD grain sizes are in the range $\geq$ 1 micron, while NCD has grain sizes in the 10-100s nm range. The grain size scales with film thickness due to the columnar growth mode. This means that NCD turns into conventional MCD material after a certain layer thickness [26]. The roughness of the film increases with the film thickness, which has a negative effect on the performance of MCD films in certain applications. Under certain conditions, new diamonds are able to grow on top of the existing ones. This process, called 'secondary nucleation', limits the grain size to that of NCD. NCD are therefore typically smoother than MCD films and have lower friction coefficients, but worse mechanical properties [27].

UNCD compromises of the smallest grains, typically in the range of 5-15 nm. The grain size is independent on the film thickness due to continuous renucleation during growth. UNCD is grown from an hydrogen poor Ar/CH_4 plasma that leads to high renucleation rate. This continuous new nucleation of crystals limits the maximum grain size [28].
The low surface roughness (Table 17, Appendix A), limited stiction with other materials and commonly very low mechanical wear has led to new breakthroughs in MEMS (micro electromechanical systems) devices [26].

2.2 HFCVD reactor

The reactor plays a big role in the hot filament CVD process, this chapter gives an overview of the type of reactor used in the HFCVD process at the TU Delft dept. Precision and Microsystems Engineering (PME). Figure 10 shows the new generation of the HFCVD reactor. Subsequently, the type of reactor, vacuum system, gas flow control, and temperature monitoring system based on this reactor will be explained. Figure 11 shows a drawing of the inside of the reactor, in which the two hanging electrodes, substrate and array of hot filaments can be seen.

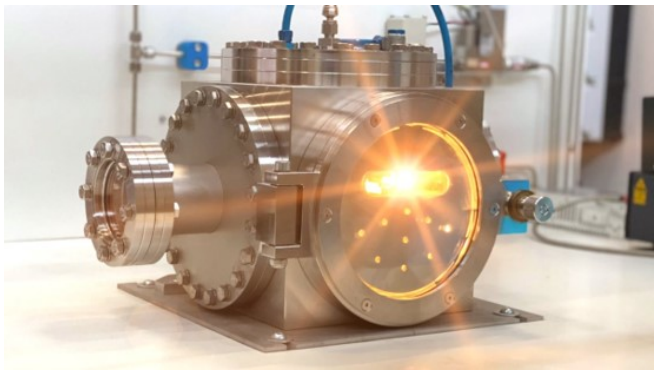

Figure 10: Photograph of the HFCVD reactor [29].

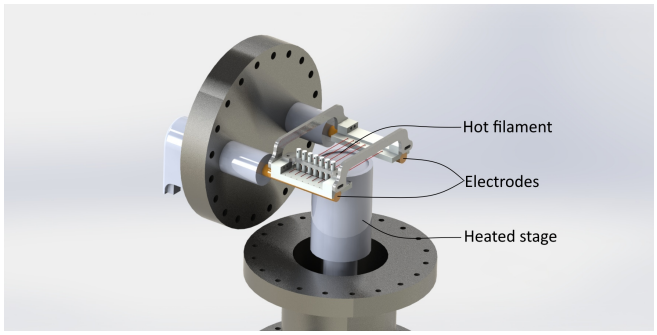

Figure 11: Render of the HFCVD reactor inside.

Reactor types and configurations. In diamond chemical vapor deposition, two types of reactors can be used. Hot wall CVD and cold wall CVD, the main difference being how they are heated. A hot wall CVD reactor works by heating the entire chamber to achieve a uniform temperature, its big advantage being potentially improving the uniformity of deposition due to a more uniform temperature. Additionally, multiple wafers can be heated, leading to a higher throughput. The downside of this type of reactor is that heating of the reactor walls can lead to contamination, resulting in inferior quality diamond growth and the need for frequent cleaning.
On the other hand, in a cold wall CVD reactor, only the substrate is heated. This localized heating of the substrate allows for relatively quick cooling. Another advantage is the simpler reactor design and reduced maintenance, associated with reduced costs, the TU Delft HFCVD reactor is a cold wall reactor [30, 31].

2.2.1 Reactor components

Vacuum system. As can be seen in the carbon phase diagram (Figure 3), a vacuum is needed to facilitate the dissociation of precursor gases like methane and hydrogen in CVD. Ensuring the creation of reactive species that contribute to diamond growth, and preventing contamination from impurities. The most commonly used type of pump is a mechanical rotatory vane pump. It operates by a rotor with vanes ($\leq$ 5000 rpm) that traps fluid in a chamber and moves it from the pump's inlet to the outlet using a rotating mechanism. A single-stage rotary vane pump can pump the system down to a few tens of mtorr, the mechanical pump becomes increasingly less effective.
Mechanical pumps alone cannot typically reach pressures low enough for high-quality thin film deposition. So an additional high vacuum pump is needed to remove more air from the chamber, and achieve much lower pressure. For most CVD processes a turbo molecular pump is used [32], however, due to the fact that growth in this specific reactor happens at relatively high pressures, it is not necessary to use a high vacuum. Next to this, the HFCVD process is not very clean inherently due to filament contamination [33].

Heating. The electrodes, the two hanging round bars on which the filament array is positioned, are displayed in figure 11. The function of the electrodes is to pass an electric current through the resistive hot filament array, consequently heating it. The electrodes must have a high-temperature resistance and sufficient electrical conductivity. In this case copper bars are used ($T_m = 1.06e3 - 1.09e3$ °C, $\rho = 1.7 - 4 \mu ohm.cm$ [6]). Additionally, copper has sufficient mechanical properties such that the electrodes can be placed horizontally, allowing for a configuration in which the hot filaments can rest on top of the electrodes. Furthermore, copper is easier to machine than other possible electrode materials like tungsten.

Contrary to the hot filament, the substrate is either heated via surface irradiation by a lamp or conduction from the sample holder. The substrate is heated by conduction from the sample holder in the cold-wall reactor used at the TU Delft, for specific schematics see Appendix (H). In a cold-wall reactor without substrate heating from above, the substrate may be 50-200 °C cooler than the heating stage [34].

2.2.2 Hot filament

The filament component functions to thermally decompose source gas molecules, converting them into reactive chemical species. Former MSc student Dilpreet Singh did a literature survey [29] on filament carburization during HFCVD diamond growth process. This part of the literature survey aims to give an introduction to the filament, and a summary on the previous findings on carburization.
The precursor gas mixture in the diamond CVD process consists of hydrogen, that does not dissociate until temperatures of 2000 °C are met. Because of this the filament needs to be made of refractory materials. The materials used for this include rhenium (Re) and the carbides of tungsten (W) and tantalum (Ta) [35, 36]. This literature survey will focus on the use of W and Ta hot filaments, due to high price of Re filaments. The mechanical properties of W and Ta are given in Table 2:

These properties indicate that the refractory materials can be used as a filament without much ad-

Table 2: Filament properties at T: 20 °C, p: 1 atm. [6, 37, 38].

Material	**Young's Modulus (GPa)**	**Electrical Resistivity ($\mu\Omega$·cm)**	**Vickers Hardness**	**Melting Temperature (°C)**
W	390–410	5.4–5.6	450	3407–3431
Ta	178.12	11.3–13.6	103	2990–3000

ditional problems. However, both W and Ta will react with the carbon-containing gasses due to carburization, leading to a change in material properties over time.

Filament carburization. Stability of the HF is the prerequisite of CVD. Several aspects can affect the stability, such as deformation, crack, breakage poisoning and volume expansion. These aspects rely on the morphology and structure of the filament, for T and W this is a changing process due to carburization. Carburization is the incorporation of carbon atoms in the metal lattice, following this sequence of steps [39]:

1. Physical adsorption of methane molecules onto the filament surface
2. Methane decomposition on the filament surface, forming carbon and hydrogen atoms that are chemisorbed.
3. Liberation hydrogen atoms, molecules and hydrocarbon species into gas phase
4. Surface adsorbed carbon atoms transition to dissolved state
5. Carbon atoms diffuse into metal lattice

Understanding of this carburization is required to stabilize the HF CVD process [25].

Tungsten (W) carburization. Depending on the process parameters, the filament undergoes structural changes and tungsten monocarbide (WC), tungsten dicarbide (W_2C) or graphite phases can form. Zeiler *et al.* [40] studied the structural changes of tungsten hot filaments for diamond CVD at standard conditions (1% methane, 99% hydrogen). From this study in could be concluded that a thin W_2C layer appears after only a few seconds. Figure 12a shows the rapid increase in W grain size. After this the outer W_2C layer grows at a constant rate, up until about one hour. At this point no metallic W can be found and the growth of WC will occur on the outside. Leading to the following equation for the carburization of tungsten in diamond HFCVD: $W \longrightarrow W_2C \longrightarrow WC$.
The resistance variation is a direct indicator of W filaments morphological and structural evolution. The difference in specific resistance of W, W_2C and WC (at 2400 °C W: 5.5 $\mu\Omega cm$, W_2C: 80 $\mu\Omega cm$, WC: 22 $\mu\Omega cm$ [39]) can be measured as a function of time to approximate the filaments structure (example of Ta filament resistance curve in Figure 12b).

Filament degradation. As mentioned earlier, filament carburization will lead to filament degradation. Cracking and graphite formation (also called filament poisoning) contribute to a shortened lifetime of the hot filament.

Crack formation and volume expansion Crack formation in the hot filament must be considered. Crack formation weakens the structural integrity of the filament, making it more prone to breaking during operation, increasing downtime.

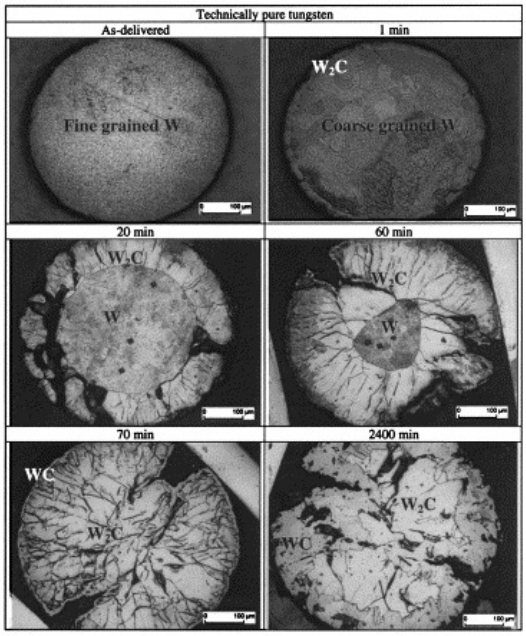

(a) Optical micrographs showing transverse sections of tungsten as function of exposure time [40].

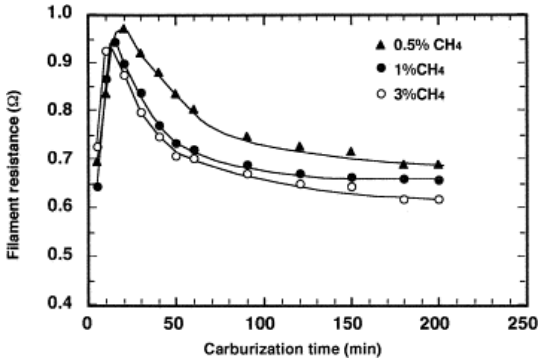

(b) Ta Filament resistance vs carburization time at 2500 °C, 30 torr and various CH_4 concentrations [41].

Figure 12: Carburization figures

For W filament carburization, crack formation can be seen in figure 12a. Due to the volume expansion large cracks form in the filament. The cracks in pure tungsten are numerous and irregular[40]. A similar effect can be seen in Tantalum. Okoli *et al.* [39] measured the volume change for the different phase changes at different temperatures. pressures and CH_4 concentrations. This resulted in a 15-18 % volume expansion for Ta at higher temperature (2400 °C) and a 8,8-22.5 % volume expansion for W at 2000 °C.

Graphite formation. Kweon & Lee [42] showed that at low filament temperatures and/or high methane concentrations graphite can form on the filaments surface. This can lead to contamination of graphite on the substrate, leading to lower quality diamond film. X-ray diffraction peaks at $2\theta = 26$ were found for several depositions at low filament temperature and/or high methane concentrations. Indicating the presence of graphite in the deposited diamond film. SEM images of the hot filament confirmed this. Figure 13 shows the cross section of the W filament. Showing that, at lower temperature graphite forms on the outer area of the W filament. A rise in the intensity of the 26° graphite peak at higher methane concentrations indicates increased graphite formation. This observation highlights that both temperature and methane concentration must be carefully managed to avoid filament graphite formation.

Filament metal contamination. The downside of HF CVD diamond films is the metal impurity that occurs due to the filament. Menon *et al.* [35] studied the contamination of the diamond film for Re, W and Ta filaments. By using Neutron activation analysis (NAA) they quantitatively determined

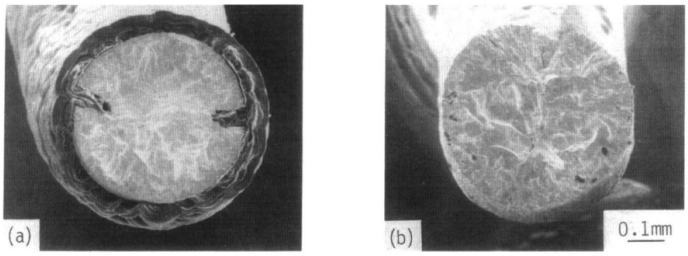

Figure 13: SEM image of filaments cross section at (a) 1900 °C and (b) 2150 °C, both 1.6 % methane concentration [42].

the metal contents in the respective films, the results can be seen in table 3. Re filaments resulted in the highest impurity levels, measured in parts per thousand by mass. Ta and W showed much lower contamination in the ppm-m range, of these two W filament showed the lowest metal contamination in the diamond film.
There was a notable correlation between the impurity levels and the quality of the diamond films. Films with lower metal content showed better crystalline quality, this was measured with Raman Spectroscopy.

Table 3: Filament metal contamination [35].

Filament material	**Filament temperature (°C)**	**Substrate temperature (°C)**	**CH4 (%)**	**Re (ppm-m)**	**W (ppm-m)**	**Ta (ppm-m)**
Re	1950	1010	1.0	5400	N/A	<<
W	1950	1018	1.0	0.6	4.6	0.4
Ta	1960	1010	1.0	1.6	2.5	37

2.3 Filament clamping and tensioning mechanisms

Tungsten filaments carburize faster than Tantalum filaments, as a result W filaments deform more than Ta filaments [43]. The filament lifetime can be increased by using a straight filament instead of a coiled one, straight filaments can better remain their shape by applying a tension. This section provides examples of clamps that minimize W deformation, as found in patents and literature. An overview of these findings can be found in Appendix C.

2.3.1 Tension by adding weights

The most common way [25, 41] to apply tension to the hot filament found in literature is by adding weights to the system. Figure 14 shows an example of a HFCVD setup that used weights to apply tensile stress to the hot filament. In this study, a 0.5 mm ∅ Ta wire is fixed to the electrode on the right, and connected to a thicker 2 mm ∅ Ta wire that can slide vertically. To the end of the thicker Ta wire, a 12 gf of tension was applied to the filament to keep the filament straight.
The tensile stress applied by this weight method can be calculated (ignoring friction) using equation 4

$$\sigma = F_g / A_{total} \tag{4}$$

In which σ is the tensile stress in Pa, F_g is the applied force by the weights and A_{total} is the total area which is equal to nA for an array of n wires. The gravitational force is equal to $F_g = mg$. This results in weights of 0.38-0.95 kg used for a stress of 4.4-11 MPa by Xiang et al [25]. And a much lower stress of 0.6 MPa being applied by the 12 gf to straigthen the Ta filament in the study of Tsutsumoto [41].

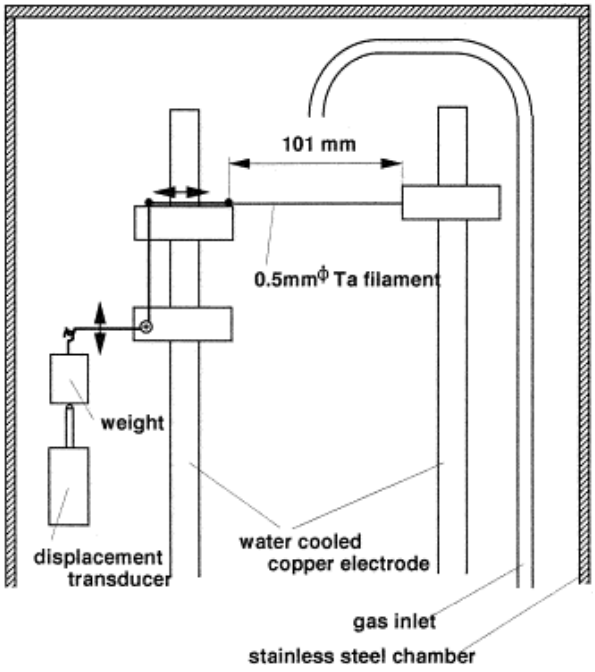

Figure 14: Filament tensioner using weights [41].

2.3.2 Spring tension

Tension force can be applied by springs, the advantage being that when using horizontal hot filaments, the springs can be used in the same plane. Contrary to using weights, in which gravity is a constant force, tension force applied by springs is a variable force. The springs shorten during operation due to it being in a hot environment, this makes the spring annealing, diminishing the coefficient of stiffness over time [44].
Nevertheless, several apparatus have been developed by inventors to minimize this effect. For example, Shuangli [45] invented an apparatus using springs that limits heat transfer to the springs by incorporating an insulating panel. Figure 15 shows the hot filament (10) being held by a fixed electrode (5) and a movable electrode (6). This moving electrode is a molybdenum wire (1-5 mm ∅) that slides over the stationary electrode (2) maintaining electrical contact. The movable electrode is fixed to a ceramic insulating panel (14) that is fixed on a slider. Finally, the spring (8) is connected to the insulating panel, applying the required tension force. Unfortunately, diamond growth data and the type of springs used were not specified in this patent.

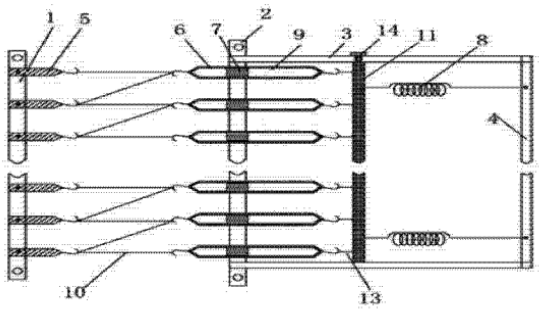

Figure 15: Tensioning mechanism using tensile springs [45].

Another example of a filament straightening apparatus is developed by Chinese inventors [46]. It involves an assembly using compression springs instead of tension springs. The apparatus is assembled prior to operation by placing the springs and hot filament between the fixing rods (110)(104), the carrier rods (101)(111) act as conductive elements for the filament. The ceramic rods (109) act as structural support and provide electrical insulation. The assembly is held by molybdenum screws, and the compression springs are made out of 'heat resistant material'. The downside of this invention is that the springs are close to the filament. However, the assembly has minimal parts and is relatively simple. This patent claims to have used this device in growing 3-4 μm diamond layers on cutting tools.

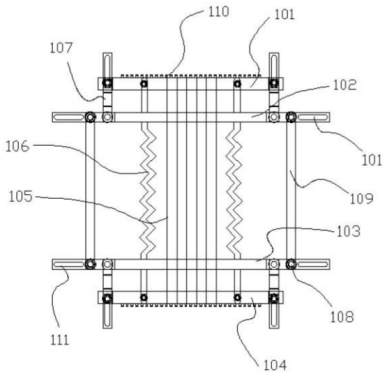

Figure 16: Tensioning mechanism using compression springs [46].

2.3.3 Movable electrode

A problem that is often not addressed in scientific papers like the ones mentioned before, is how to overcome the friction force present between the hot filament and electrode. By looking at patents, solutions were found that minimize this friction force by using a movable electrode [44]. Figure 17 shows that the engineers opted for a fixed electrode (1) that is connected to piston-type electrode (5) ensuring that resistive heating occurs while minimizing friction. This patent claims to have increased tantalum filament lifetime to 150 hours, achieving diamond film thicknesses of 1 mm. Operating at normal conditions(2500 °C, CH_4 concentration 4%).
While the friction force at the friction at the electrode is minimized, other Chinese inventors [47] mentioned that the friction at the pulley block (9) is still significant. The pulley block is placed in a high temperature environment, and cannot be lubricated with traditional liquid lubrication. This leads to difficulty in maintaining the stability and consistency of the pulley block.

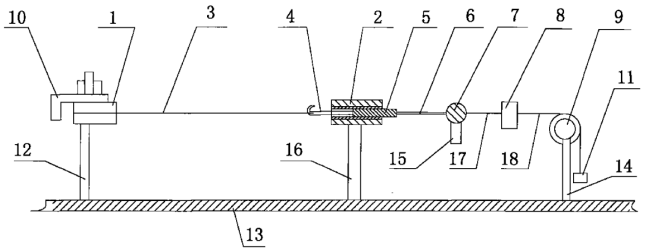

Figure 17: Weight tensioning patent minimizing friction using a movable electrode [44].

Patent US5833753A [48] also mentions the use of movable electrodes. This time fixed to a spring, instead of weights. This patent describes three different ways of fabricating the movable electrodes, each with its advantages and disadvantages summarized in Figure 18. The movable electrode (140) provides the necessary space for the filament to expand, while the spring (112) tensions the filament in the right direction. Preferably a minimal force of no more than a few ounces is applied to the screw. A low spring constant is preferred to minimize the change in tension force as the filament expands. Herlinger *et al.* [48] provide extensive reasoning on why tensioning with spring and force regulator is preferred.

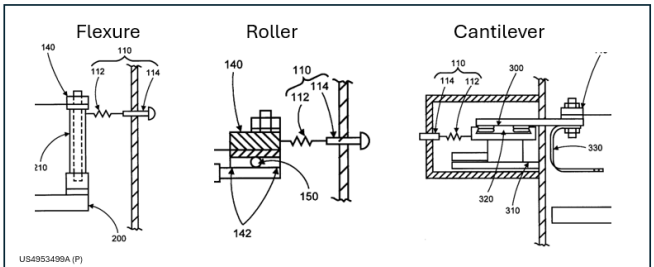

	Flexure	Roller	Cantilever
Advantages	Minimize off axis forces	Simple, easy to maintain	Precise control, minimize vibrations
Disadvantages	Prone to fatigue, limited range of motion	Limited ability to handle vibrations	Expensive, complex

Figure 18: Three different movable electrode designs (adapted from [48]).

2.4 Heat transfer simulations

The temperature gradient produced by thermal energy generated from the filament has a large influence on the growth of diamond thin films [49]. It is difficult to obtain detailed HFCVD apparatus temperature distributions by experiments, hence finite element methods (FEM) are used to obtain this distribution. Additionally, modifying parameters such as filament radius, filament separation distance, and filament substrate distance is possible using FEM.
The evolution of these structural models has evolved from theoretical models considering only the dominant radiation [50], to complex 3D models that can simulate the temperature distribution in a commercial CVD apparatus [51]. This subsection firstly describes the physics in heat transfer simulations in Section 2.4.1. Hereafter, a summary of the existing literature on HFCVD temperature distribution simulations is given in Section 2.4.2.

2.4.1 Relevant physics

The HFCVD process is governed by the interplay of multiple physical phenomena, namely heat transfer, fluid dynamics, and chemical reactions. These are briefly discussed in the sections below.

Heat transfer. The heated filament acts as a thermal energy source, raising the local gas temperature and initiating gas decomposition. Heat transfer in the system involves:

- Conduction through the filament and structural supports.
- Convection between the filament and surrounding supports.
- Radiation, particularly at high filament temperatures, has a significant effect on heat distribution.

Radiative heat transfer is dominant over both conduction and convection. Radiation scales with T^4, conduction and convection with $\approx T^1$. The relative importance of convection and conduction can be indicated by the Peclet number. This is a dimensionless number, shown in Equation 5:

$$Pe = \frac{VL}{\alpha} \tag{5}$$

where V is the characteristic velocity of the flow, L is the characteristic length scale, and α is the diffusivity. A high Pe value (Pe $\gg 1$) indicates transport is mostly due to bulk flow, a low Pe value (Pe $\ll 1$) means that diffusion dominates due to molecular movement, rather than flow [52]. For their particular setup, comparable to the TU Delft setup, Wolden *et al.* [50] estimated the Pe value to be $\sim 10^{-4}$. As a result, heat loss by convection can be safely neglected, and only conduction and radiation will be considered in the heat transfer in the system.

Fluid dynamics. For the hydrogen flow, the Mach number $V/c \ll 0.3$ (where V is gas velocity, c is the speed of sound in the fluid [53]). This makes the gas incompressible-ideal. The Reynolds number indicates the type of flow, and is given by Equation 6:

$$\mathrm{Re} = \frac{\mathrm{ud}}{\nu} \tag{6}$$

where u = velocity, based on inlet diameter, d = hydraulic diameter, ν = kinematic viscosity). In the PME HFCVD reactor, u $\sim$ 1 m/s, d = $3 * 10^{-3}$ m, and $\nu \sim 1.1 * 10^{-4} m^2/s$ [54]. What follows is that Re $<$ 2300, which means that the gas flow is laminar [53].

Chemical reactions. The various chemical reactions occurring near the filament (activation) and at the substrate/film surface (Figure 4), including hydrogen decomposition, bonding of active groups, carbon–carbon bonding, and hydrogen-atom etching, collectively influence the heat distribution within the reactor [53]. Wolden *et al.* [50], modeled the heat transfer by radiation to predict the substrate temperature (substrate passively heated by hot filaments). They noticed an increase in experimental temperature w.r.t only accounting for radiation of $\sim$ 100 C °, while this effect was also noticed by Zhang *et al.* [53] in a lesser degree (15 C °). This increase can be accounted for by H atom recombination and conduction. H atom recombination occurs at the substrate surface, it is a very exothermic reaction (ΔH_r = -444 kJ/mol of H_2). The relative contributions of H atom recombination and conduction were measured by monitoring the reactor in hydrogen and helium gas separately. This was done by first measuring the temperature in a vacuum, and after this, measuring the temperature at 30 Torr. This elevated pressure, leaded to a 90 °C temperature increase. Then, based on the thermal conductivity of the two gasses, 60 $\pm$ 5 °C can be attributed to H atom recombination, and 25 $\pm$5 °C to conduction [50].

2.4.2 HFCVD simulation results in literature

Simulating the HFCVD process started in the 1990's with DebRoy *et al.* [55] numerically computing the equations of mass, moment, and enthalpy to obtain temperature and fluid flow fields for different 2D HFCVD reactor configurations. Wolden *et al.* [50] numerically computed the temperature distribution on substrates, as a function of the proximity of the filament to the substrate. Most notably, the relations between filament emmisivity (Figure 19), radius (r), filament substrate distance (H), and filament temperature (Tf). Additionally, they proved that the temperature distribution of a rotating substrate is more uniform than that of a stationary substrate.

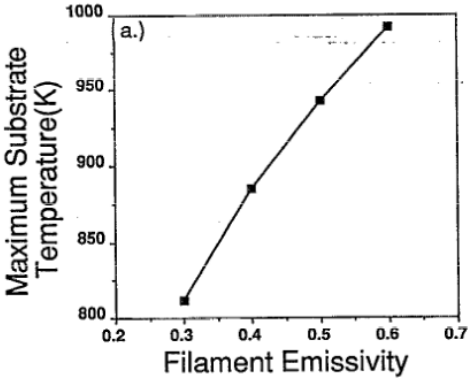

Figure 19: The dependance of calculated maximum substrate temperature on filament emmisivity for three 10 cm parallel filaments (r: 0.625 mm, D: 20 mm, H: 12 mm, Tf: 2500 K) [50].

The 1990s and early 2000s had huge excitement about the plethora of applications of thin film diamond. Unfortunately, using diamond as a semiconductor was harder than expected due to the difficulty to find a useful n-type dopant [9]. After the hype around diamond thin film died down in the United States and Europe, funding also decreased. However, starting in the 2010's the popularity of HFCVD diamond rose. New applications were found, such as electrochemical electrodes and the ability to grow large single-crystal gemstone-quality diamonds. Mainly in China, research groups and companies started developing their own HFCVD apparatus at a larger scale. In the meantime technology had advanced, FEM software like ANSYS or COMSOL could now be used to optimize the reactor configurations.

In 2012, Zhang *et al.* [53] developed a model with an error between the simulated and actual temperature of only 3 %. This study varied the deposition parameters (Number of filaments [N], radius [r], filament-filament distance [D], Filament substrate distance [H]) for their particular reactor, while also varying the gas inlet. In the end, preferred parameters were obtained. This study is cited 51 times and is one of the most popular papers on HFCVD diamond simulation. Lots of research groups replicate this study with their type of filament configurations and substrates. Examples of this are: Song *et al.* 2017 [56], Panickar *et al.* 2019 [57], Wu *et al.* [58], Wang *et al.* 2023 [51], and Hao *et al.* 2024 [59]. A summary of the relevant HFCVD simulations and their objectives can be found in Table 4:

Table 4: HFCVD simulation papers.

Author	Year of publication	Objective	Method
DebRoy [55]	1990	Optimal gas flow configuration.	Numerical
Wolden [50]	1992	Minimal temperature variation across substrate	Numerical
Zuo [60]	2007	3D simulation to obtain substrate temperature contours	ANSYS
Zhang [53]	2012	Influence key parameters on temparature distribution on substrate	ANSYS-FLUENT
Shen [61]	2014	Optimize substrate temperature unifority	Not mentioned
Song [56]	2017	Relation power, filament, and substrate temperature	ANSYS-FLUENT (17.0)
Panickar [57]	2019	Optimize substrate temperature distribution.	ANSYS-FLUENT
Wu [58]	2021	Influence key parameters on temparature distribution on substrate	COMSOL Multiphysics
Choi [49]	2023	Worktable temperature prediction.	ANSYS-FLUENT (20.1)
Lee [62]	2023	Simulate H generation.	Numerical
Hao [59]	2024	Effect filament spacing on uniformity temperature field.	ANSYS R15.0
Wang [51]	2024	Reduce electrical power consumption in HFCVD apparatus	ANSYS-FLUENT
Kwok [63]	2024	HFCVD with magnetic field assistance simulation	COMSOL Multiphysics
Ruan [64]	2024 (preprint)	Optimize substrate temperature uniformity	COMSOL Multiphysics

Some of these authors, have multiple papers on HFCVD simulation, in Table 4, the most relevant one is mentioned. For example, Song has upwards of 10 papers on HFCVD diamond simulation from the early 2000s up until now.

3 Research focus

This chapter highlights the scope, goal, and research questions of this MSc thesis project.

3.1 Problem statement

A new HFCVD reactor setup, shown in Figure 20, has been designed and built by the technical staff of the Precision and Microsystems Engineering (PME) department at TU Delft. Unlike the previous setup, which used a single coiled filament, this reactor employs an array of hot filaments. This configuration should allow for scalable diamond deposition over larger substrate areas, up to 2-inch wafers, and enable more uniform film growth.
Former MSc student Dilpreet Singh [29], tested the effect of different deposition parameters (i.e. filament-substrate distance, stage temperature, and methane concentration) on diamond growth on Si (100) substrates. He found that the lifetime of the tungsten filaments was limited due to the sagging effect. To improve diamond growth in the new setup, this sagging should be minimized.

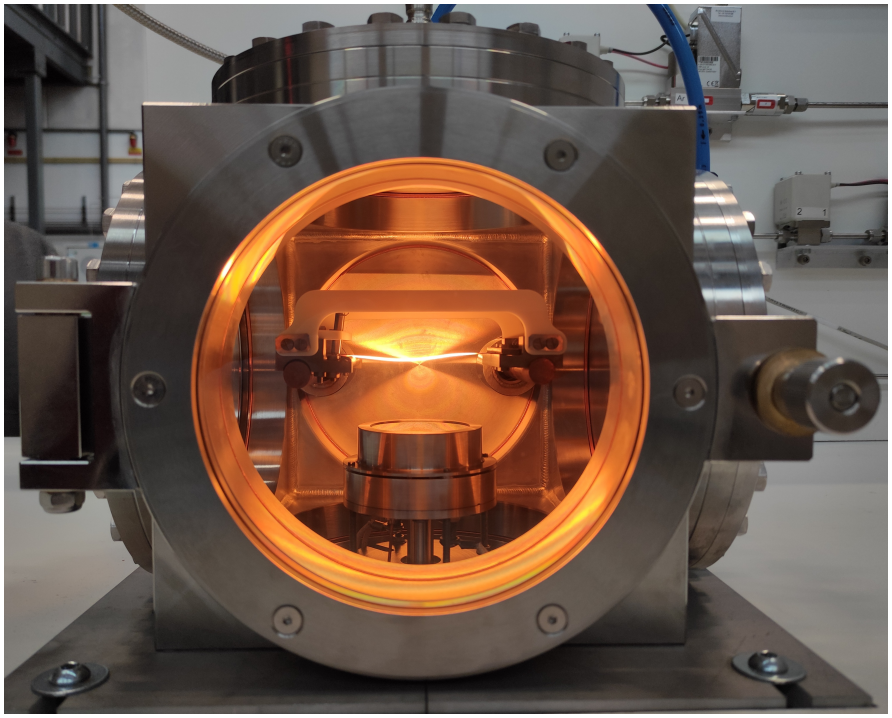

Figure 20: HFCVD reactor setup at the TU Delft Precision and Microsystem Engineering department.

3.2 Goal of this research

The primary goal of this research is to enhance the quality and consistency of diamond growth in the newly developed hot-filament chemical vapor deposition (HFCVD) setup. To achieve this, a design study was conducted to develop and manufacture a novel filament clamping mechanism aimed at minimizing filament sagging, which is a key factor affecting temperature uniformity and film quality.

Due to ongoing maintenance issues with the heater stage, experimental validation of the new clamp design was not feasible during the project timeline. As a result, a secondary objective was introduced: the development of a multiphysics simulation model of the HFCVD reactor using COMSOL. This digital twin enables detailed analysis of temperature distribution and gas flow dynamics within the reactor.

Building on prior experimental work by Dilpreet Singh [29], which investigated the influence of deposition parameters such as filament-substrate distance and methane concentration, this study focuses on parameters that are difficult to explore experimentally (without buying new components). These include filament-to-filament spacing and filament radii. The simulation model serves as a cost-effective and flexible tool to optimize reactor design and deposition conditions. It also provides guidance for future experimental efforts aimed at improving the scalability and reliability of diamond film synthesis.

3.3 Research questions

The main research question of this research is:
How can filament clamping design and temperature distribution modeling be optimized to improve filament lifetime and deposition quality in a home-built HFCVD reactor?

Several sub-questions that need to be answered during the course of this project are:

- How can a filament clamping mechanism be designed and manufactured within a €3000 budget to minimize sagging and withstand high-temperature HFCVD conditions?
- What materials and configurations for clamp components offer the best balance between thermal stability, manufacturability, and contamination risk?
- What modeling strategies and boundary conditions are required to accurately replicate the thermal and fluid dynamics of the HFCVD reactor in COMSOL?
- What is the effect of varying deposition parameters (filament radius, filament-filament distance, and filament-substrate distance, and substrate heating power) on substrate temperature distribution?
- What is the effect of filament sagging on the substrate temperature distribution?
- How can the COMSOL model be validated through comparison with literature data?

4 Methodology

4.1 Clamping device

This first part of this section starts with the boundary conditions the clamp must agree with, presents the three proposed clamp concepts and their material choices. Includes results from prototyping, thermal simulations, and cost assessment.

4.1.1 Boundary conditions

Dimensions. Figure 20 shows the inside of the hot filament chemical vapor deposition (HFCVD) reactor. Pictured is the current clamping mechanism, which does not minimize sagging of the hot filament. The electrodes are made of copper. A front view of the dimensions of the reactor without the current clamping mechanism can be seen in Figure 21 (a), and a side view in Figure 21 (b).

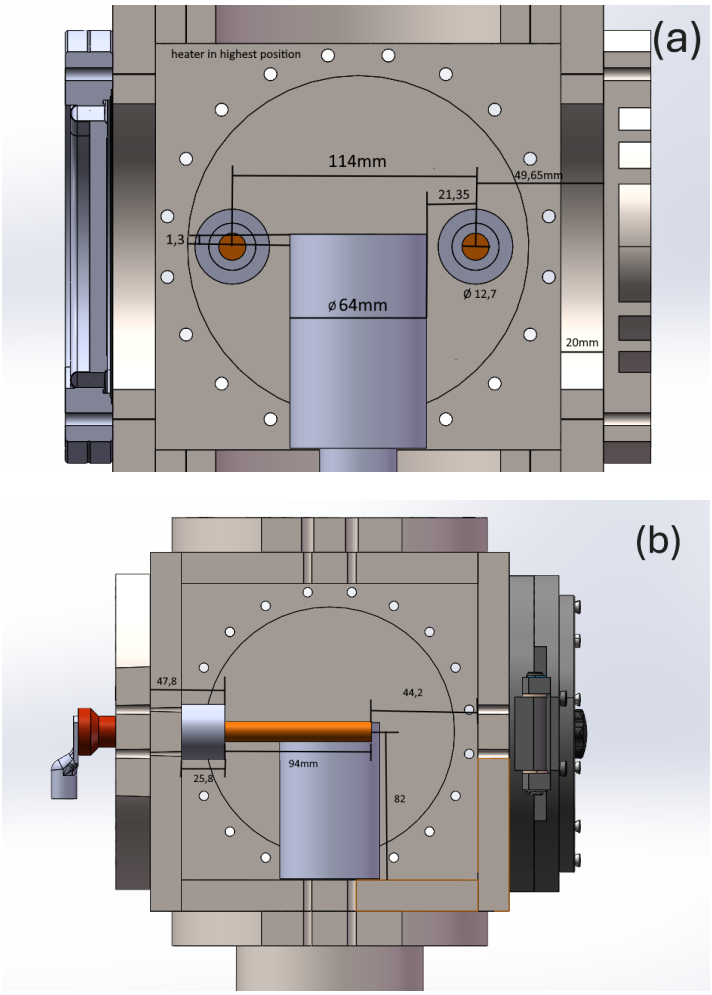

Figure 21: Reactor dimensions. (a) shows the front view, (b) the side view.

Temperatures. The cold wall reactor is passively heated by both the substrate and the heated filament. The substrate gets heated to 600-900 °C, while the heated filament is heated up to 2500 °C depending on the type of filament used. Finally, the reactor flanges are water-cooled by the circulating fluid temperature controller (SMC – HRS). The temperature distribution inside the reactor can be measured at certain spots using a pyrometer. Section 4.2 aims to utilize FEM software to obtain a temperature distribution of this particular HFCVD setup.

Materials. The reactor consists of a cubic shape reactor build out of stainless steel 304. The electrodes that provide Joule heating to the heated filament are made of copper round bars.
Due to the high temperatures in parts of the reactor, some of the components have to be made from refractory metals. Thus, the current filament clamp utilizes molybdenum parts that are in direct contact with the copper electrodes. The insulating bridges are made from alumina (Al_2O_3).

Requirements. Below, in Table 5, a list of all the extracted requirements can be found. Each requirement has a priority that follows the MoSCoW method [65] (M- Must, S- Should, C- Could, W- Won't), and then a concise description of the expected behavior.

Table 5: List of requirements for the clamping device

Priority	Description
M	R1) The mechanism shall be made out of refractory metals, or other temperature resistant materials
S	R2) The mechanism shall take into account a 22.5 % filament expansion
M	R3) The mechanism shall be made to fit through the reactor opening
S	R4) The mechanism shall work for an array of heated filaments
C	R5) The mechanism shall be easy to assemble
S	R6) Parts that connect the electrode to the filament shall be conductive
M	R7) Parts that connect to both electrodes shall be insulated
S	R8) The mechanism shall be made out of a material that has limited degradation, to prevent contamination
S	R9) The mechanism shall be easy to use
S	R10) The force delivered shall be adjustable
M	R11) Moving parts of the mechanism shall not come into contact with other parts of the HFCVD setup

4.1.2 Concepts

This part will cover three possible concepts for a new clamping mechanism. The first one is the best possible combination of a movable electrode and a straightening mechanism concept. While the two alternative concepts both use a support wire from beneath in a different manner. The tree in Figure 22 shows how this chapter divides the various concepts (C1, C2, C3).

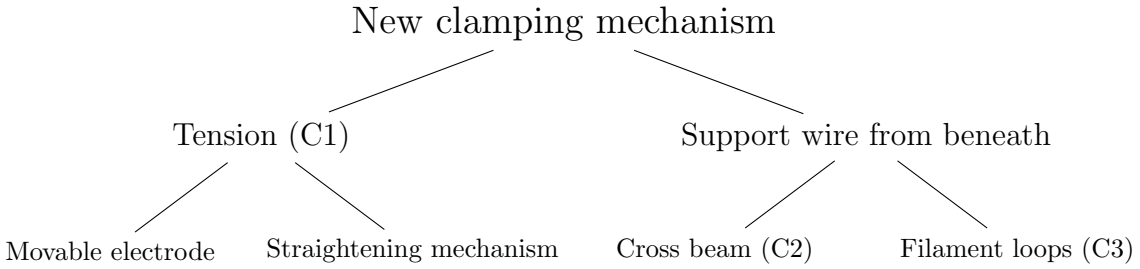

Figure 22: Tree structure of the new clamping mechanism possibilities

Straigthening mechanism, in combination with movable electrode. This part of the thesis serves as a follow-up to the patent study done in the literature survey. The aforementioned straightening mechanisms and movable electrode types will be compared for usage in the PME HFCVD reactor.

Straightening mechanism. The design option tree (Appendix B) shows the possible concepts for a hot-filament straightening mechanism. These concepts are evaluated based on the requirements from Table 5. The ones that fullfill the 'must' requirements get compared in a trade-off table to obtain a final straightening mechanism, which will be used for the final design.

Table 6: Evaluation of Different Mechanism Concepts

Concept	**Usable**	**Notes**
Tensile springs	yes	
Compressive springs	yes	
Weights	yes	
Thermally expanding material	yes	
Shape memory alloy	Maybe	R1, Usable up to ∼500 degrees °C [66]
Piezoelectric	Maybe	R1, Conventional ones usable up to 500 degrees °C [67]
Electric motor	Maybe	R1, Insulated brushless DC motor tested up to 155 degrees °C [68]
Hydraulic motor	No	R1, Fluid breakdown at 150 degrees °C [69]
Pneumatic motor	No	Unsuitable in vacuum due to air dependence
Pretensioning pegs	No	R2, does not allow heated filament to expand
Pretensioning screw	No	R2, does not allow heated filament to expand
Bending	No	R2, does not allow heated filament to expand

After evaluating the possible concepts based on the requirements in Table 6, numerous concepts can be left out. This leaves springs, weights, and possibly thermally expanding materials and motors as viable options. The concepts that are left will be briefly explained, and compared in a trade-off table.

Concept 1: Weights

The working principle of the weights based mechanism is showed in Figure 23. The electrodes are shown as [1], the heated filament as [2], a general movable electrode as [3], some sort of pulley in [4], and finally the mass in [5]. The mass applies a tension force due to gravity, the pulley in turn alters the direction of this force to be in plane with the hot filament.

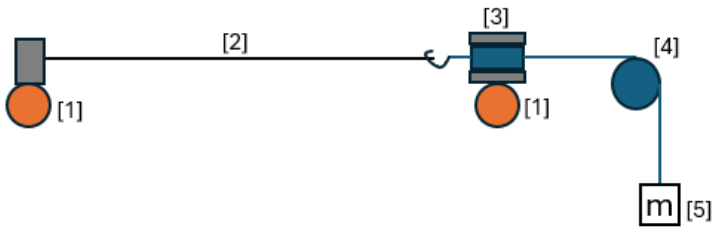

Figure 23: Weights based straightening mechanism side view

Concept 2: Compression springs

The compression spring schematic is shown in Figure 24. From the side, it looks similar to the other concepts, because the compression springs [4] will most likely be used in the same plane as the heated filaments. Figure 24 (b) shows that from above, two compression springs are positioned at both sides of the hot filament array.

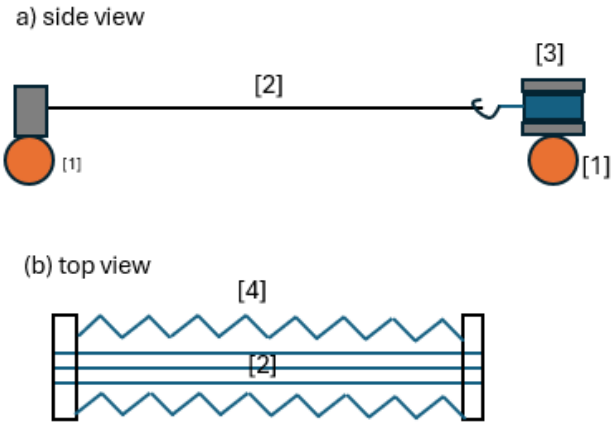

Figure 24: Compression spring based straightening mechanism

Concept 3: Tensile springs

A schematic of a basic tensile spring concept is shown in Figure 25. In this concept, a tensile spring [4] is attached to the movable electrode. It is important that the spring does not reach a temperature above its maximum working temperature. For this, the spring can use the reactor wall as a heat sink, and/or an insulating material can be put in between the movable electrode and spring.

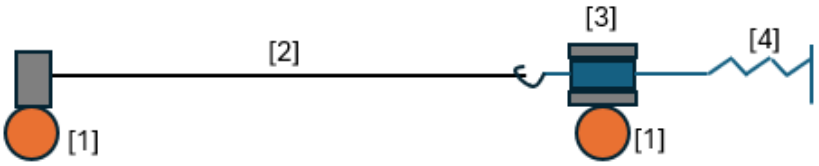

Figure 25: Tensile spring based straightening mechanism

Concept 4: Thermally expanding material

The final possible concept works by using a thermally expanding material [5] to apply tension to the heated filament. Most likely, this material will not expand $> 20\%$, hence a lever [4] is drawn in the schematic. This lever diminishes the force output, but increases the extension range.

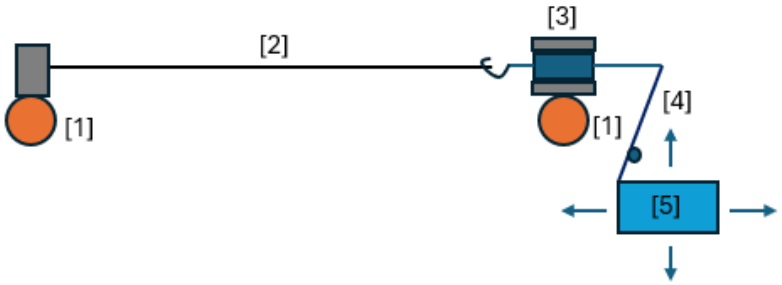

Figure 26: Thermally expanding material based straightening mechanism

Straightening mechanism trade-off table. This trade-off table compares design concepts based on key performance criteria such as complexity, contamination risk, heat resistance, space requirements, and costs. Most of the scores are arbitrary, but the including notes attempt to give a brief explanation. The trade-off table is located in Table 7, a lower score is preferred.

Table 7: Straightening mechanism trade-off

Criteria	Weights	Tensile Springs	Compressive Springs	Shape Memory Alloy
Contamination	1	5	5	7
Heat resistance	4	3	4	7
Space requirements	7	3	2	7
Costs	3	4	4	6
Total Score	15	15	15	27

Weights concept.
The weight concept can be made entirely out of non-contaminating materials. All the materials, except for the pulley can be made from refractory metals, giving it a good score on heat resistance. The concept does require a large amount of space compared to others. Due to the high amount of components the cost is scored as sufficient.

Tensile and compressive springs.
The springs can suffer from contamination. Nickel-based super alloys, the most common material for heat-resistant springs, have relatively high vapor pressures. Nickel evaporation also catalyzes graphite growth over diamond [33]. Meaning that the materials can slowly evaporate and potentially contaminate the deposition process. Springs are annealing, meaning that the spring constant will diminish over time in the heated environment. However, several springs severely limit this effect, and an insulating casing can be employed around the spring. The space requirement of both types of springs in very small in comparison to the other options. Finally, the costs are slightly higher than weights because of the relatively expensive heat-resistant springs.
The main difference between the tensile and compressive springs is in where the springs will be placed. The tensile springs will be placed on the side of the heated filament, while the compressive springs will be placed in a jig on top of the heated filament. This means that the compressive spring will experience a higher temperature, but take up less space.

Thermally expanding material. The final viable option, thermally expanding material, gets the worst final score on contamination. Refractory metals such as molybdenum have a low coefficient of thermal expansion, meaning they cannot be used. Materials such as titanium alloys can be used but can degrade in the reactor environment. Due to the required lever to amplify the moment arm, the space required is also much bigger than in other concepts. Lastly, the amount of parts and rotating components is higher than in the other components.

Movable electrode Section 2.3.3 explained that the movable electrode is the essential component in letting the hot filament expand, if tension is applied to the filament. Additionally, experience has shown that applying tension to regions of the W filament outside the heated zone has little effect. Hence the movable electrode, which allows the force to be directly applied to the heated parts of the filament. Hereafter, different movable electrode concepts will be explored. Just like the straightening mechanisms these concepts will be evaluated based on viability. Finally, one type of movable electrode will be incorporated in the final tensioning concept.

Concept 1: Bushing (glijlager).
The first concept can be seen Figure 27. In this concept, the copper electrodes are in electrical contact with additional molybdenum components [3,5]. The friction then gets minimized by a heat resistant bushing, shown in light grey [4]. This concept is inspired by Wang *et al.* [44].

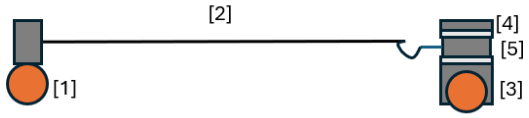

Figure 27: Bushing concept

Concept 2: Flexure.
The second concept, seen in Figure 28, makes use of an electrode that has low stiffness. The flexure [3] allows for movement in the x-direction, allowing the heated filament to expand. The material that this flexure can be made off is unknown as of yet. Herlinger [48], on which this idea is based, does not mention a specific material used.

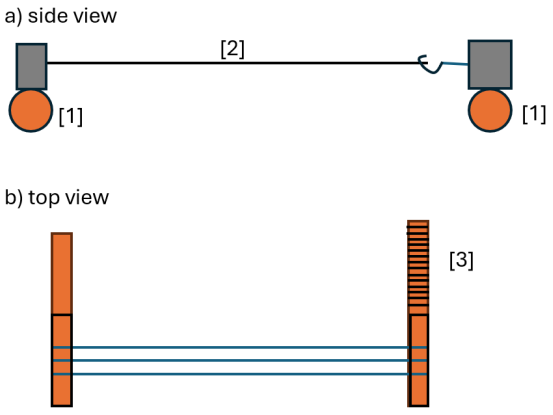

Figure 28: Flexure concept

Concept 3: Roller.
The final concept is displayed in Figure 29. It is similar to the concept utilizing bushings, but now uses rollers [3] to allow for the movement. To stabilize the structure, insulating support rods [4] are added.

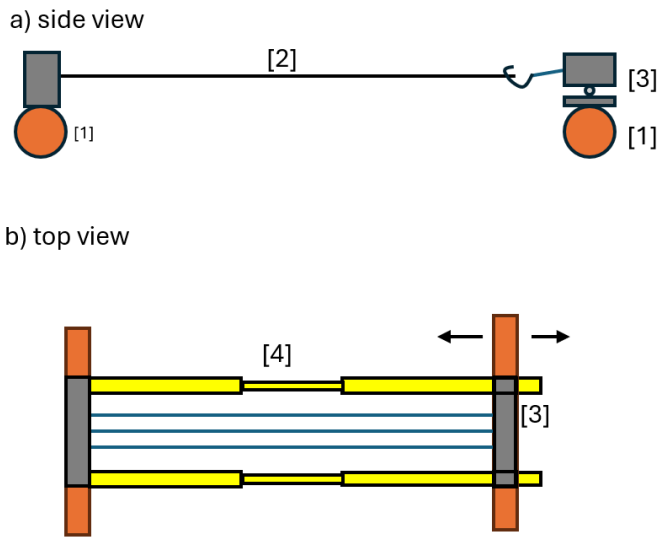

Figure 29: Roller concept

Trade-off movabel electrode. Just like in Table 7, Table 8 arbitrarily scores the concepts based on relevant criteria. Likewise, a low score means better performance.

Table 8: Trade-off table movable electrode concepts

Criteria	Bushing	Flexure	Roller
Range of motion	3	7	3
Precision	4	6	2
Friction	5	2	4
Complexity and cost	3	6	7
Total score	15	21	16

Bushing concept.
The bushing and roller concept offer the possibility of larger displacement, which is beneficial for the 20 percent material expansion. Bushing precision is limited due to wear over time. Bushings are the cheapest and least complex concept.

Flexure concept.
The range of motion of the flexure is limited by the elasticity of the electrode. They are also less precise due to the off-axis movement. However, friction is low and wear even lower. Finally, the design off a new flexible electrode adds complexity.

Roller concept

Rollers allow for precise, heavy load, low friction large displacement. The downside is the higher cost, especially in the heated vacuum environment.

Concept 1: Straightening mechanism with movable electrode. Based on the concept trade-offs, a preliminary final design has been developed. It was decided that a tensile spring was best for this reactor, due to the limited amount of space. Furthermore, a bushing will be used as movable electrode, due to the cost benefits.

Figure 30 illustrates a part of the original clamp, with additional molybdenum components highlighted in dark grey. The upper molybdenum components function as clamps for the black graphite plates, which act as plain bearings for the molybdenum part sandwiched in between.

This sandwiched molybdenum component serves as the attachment point for the W wires and the insulating yellow cross. The movable electrode design is guided by the molybdenum sliding rail and tensioned by attaching it to the reactor wall using tension springs. To secure the assembly, milled stainless steel blocks are bolted onto the reactor walls using tapped M3 holes. The section view, displayed in Figure 31, properly shows how the heated filament is connected to the moving molybdenum electrode parts. This part was not properly modeled in Figure 30.

The springs can be made of a heat resistant material such as Inconel X-750. Additionally, the alumina (Al_2O_3) cross part could be redesigned with a hexagonal shape to enhance its strength. Suppliers still need to be identified for graphite plates with the required dimensions. The molybdenum components can likely be machined by DEMO, while the alumina parts can be sourced from Ceratec, Gimex, or Lauwershanique.

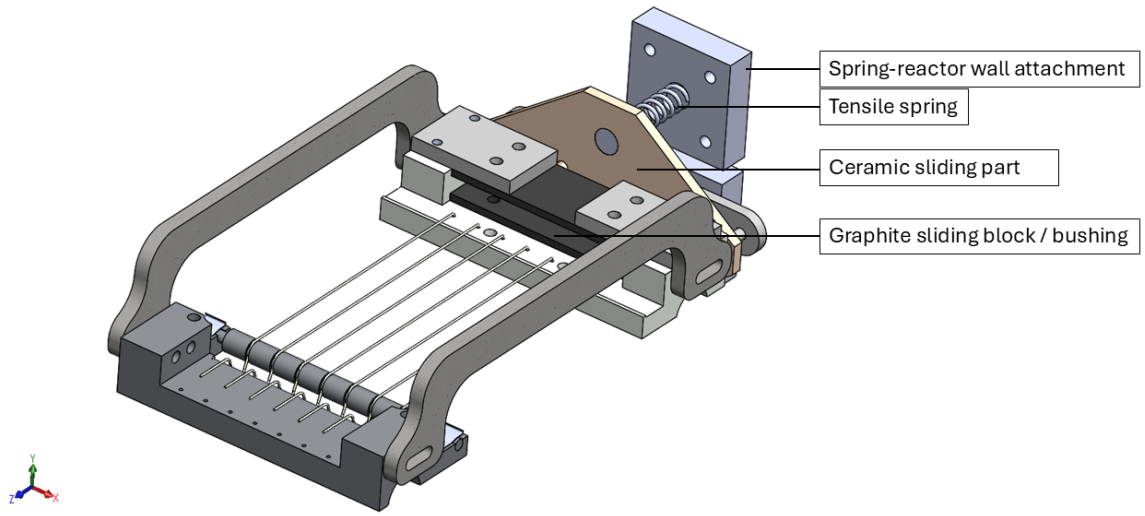

Figure 30: CAD design straightening mechanism with movable electrode

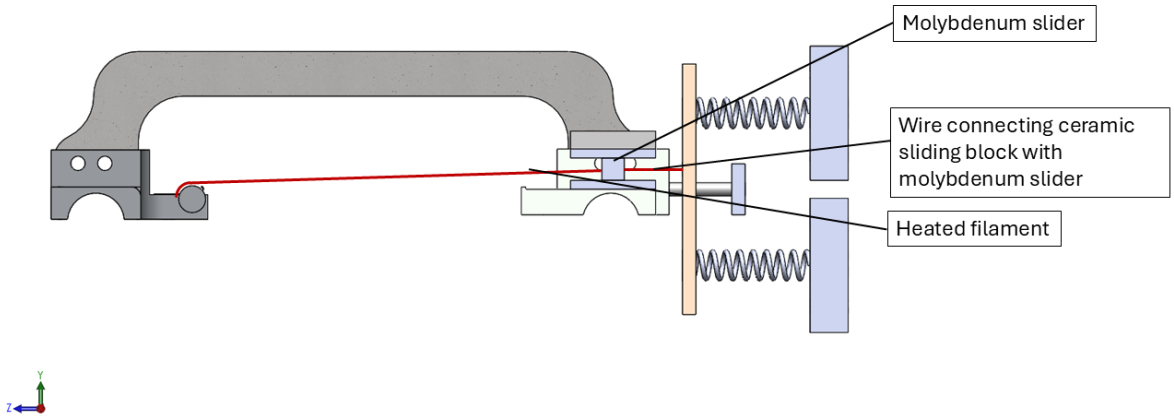

Figure 31: Section view in the YZ-plane of the straightening mechanism CAD design.

Support wire form beneath Two types of designs are discussed in this section, one supporting the heated tungsten wire with a cross beam, and the other utilizing tungsten loops.

Concept 2: Cross beam. In his MSc thesis, Singh [29] proposed a cheaper, easier to produce solution to the filament sagging than applying tension. The idea is that expanding the current clamp with additional an additional alumina cross beam. This kind of design is easy to manufacture, it consists of 2D alumina parts that can slide into each other to form a rigid Connection. The clearance for the sliding parts has to be carefully adjusted by first making a 3D printed prototype. Additionally the cross beam temperature distribution should be simulated, to see if it does not exceed maximum working temperature of Alumina.

A new version of this design has also been developed, shown in Figure 32. It has been designed to be modular; the clamp design can easily be changed to the filament loops concept, explained in the next paragraph. The new iteration features a rod that supports the filament from underneath, minimizing the contact of the heated wires with the support beam.

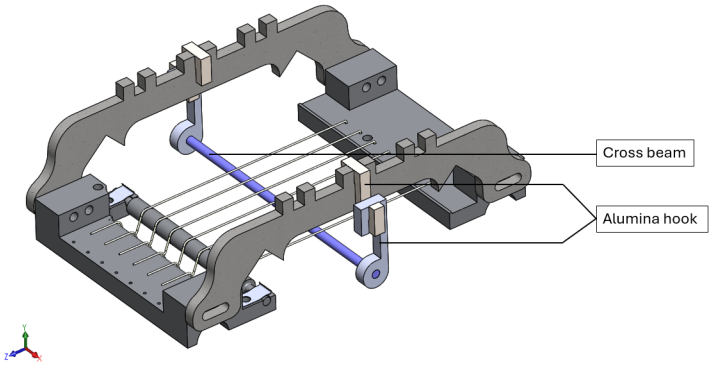

Figure 32: CAD design cross beam iteration 2

Concept 3: Filament loops. The second version of supporting the heated wires is inspired by tungsten filament lamps. To prevent sagging of the heated wire due to gravity and thermal expansion, some tungsten filament lamps use a 'spider'. The spider is a metal frame that holds and stabilizes the coiled tungsten filament inside the bulb. The filament needs to be precisely positioned to ensure even heating, and optimal light distribution. Figure 33 shows an example of such a spider support mechanism, the spider is made of either molybdenum, nickel-based alloys, or tungsten.
Modifying the spider working principle to the current clamp is done by hanging tungsten support loops (spiders) from additional alumina cross beams, as shown in Figure 34. For this to work, the original molybdenum parts of the current clamp can be reused. The additional cross beams are colored green, and have indentations on top or holes, from which the tungsten loops can hang. The current design utilizes tungsten support loops because tungsten wire is available. The less brittle molybdenum might work better in a future prototype. Like the previous concepts, the filament loops temperature distribution has to be tested. This will be done in Section 4.1.3.

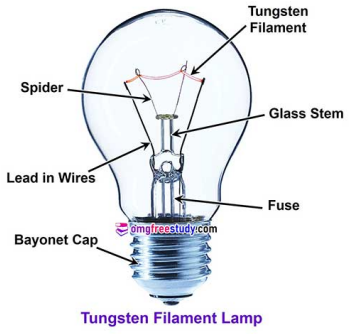

Figure 33: Spider example [70].

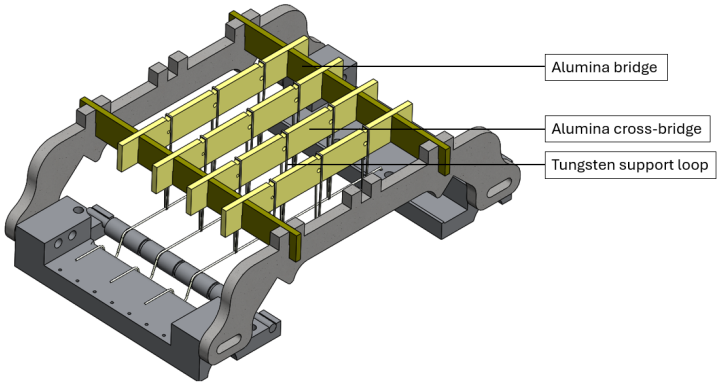

Figure 34: CAD design of filament loop clamp.

4.1.3 Detailed validation

Experimentally testing the new clamp designs is expensive due to the valuable heat resistant materials such as molybdenum and alumina. Hence, this section will test the three current designs by fabricating prototypes, and simulating the heat transfer in the clamp materials.

Prototypes.

Filament straightening mechanism. Figure 35 shows and image of the prototype of the spring tension concept in combination with the bushing movable electrode (render in Figure 30). The main lessons learned from the 3D printed prototype is that tolerances are tight, the rail guide is prone to jamming. The 3D printed clearance hole gets worn out by the metal bolts that are used as guiding rods, enlarging the holes, leading to jamming. To prevent this issue, the final design must use graphite rods as guiding rods. These rods are widely available, and temperature resistant. The prototype uses bolts as end stops on the linear guide rod. However, graphite rods cannot be tapped, so custom set collars have to be made.
Another issue with the 3D printed prototype is the incorrect spring stiffness. The prototype uses cheap off the shelf which springs which are too long. It does prove the concept, the force is applied in the right direction. The spring that will be used in the final design will be a custom temperature resistant spring, the required stifness is dependant on the amount of filaments, filament material, and more. Appendix D shows a MATLAB script which calculates the required spring stiffness for tantalum filaments, the required force for tungsten filaments has not been studied yet.

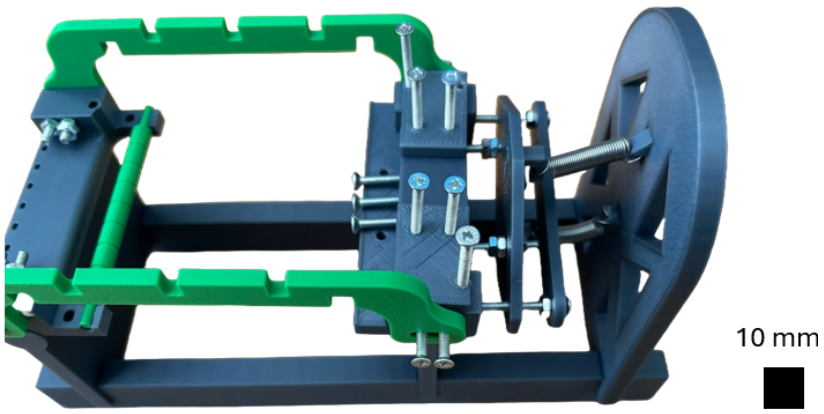

Figure 35: 3D printed prototype of the spring tension concept

Cross beams. A photo of the cross beam prototype can be seen in Figure 36. The same side beam as in the tungsten loops design, making it a modular design. Manufacturing and assembling this prototype took the leas amount of time. The only concern is the round bar, the 1 mm diameter is very small, and thus fragile. Making the round bar diameter bigger would solve this issue, but would als increase shadow effects. Shadow effect lead to uneven heating of the substrate.

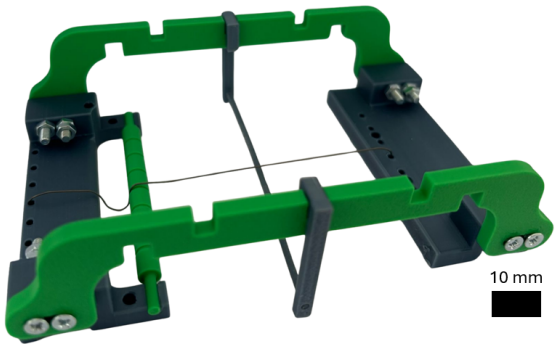

Figure 36: Cross beam 3D printed prototype

Tungsten loops. The tungsten loop prototype (Figure 37) was significantly easier to manufacture and assemble than the filament straightening one. The 3D printed overhang beams slid into each other without problems using a slight tolerance. The only issue is the tungsten loop production. A 3D printed mould is produced to guide the production of the tungsten loops, which are bent using pliers. Due to the brittle nature of tungsten, the wire is hard to bend without breaking. Using molybdenum wire could provide an easier to work with alternative, with even higher melting points. For this thesis, tungsten is used because it was already available.

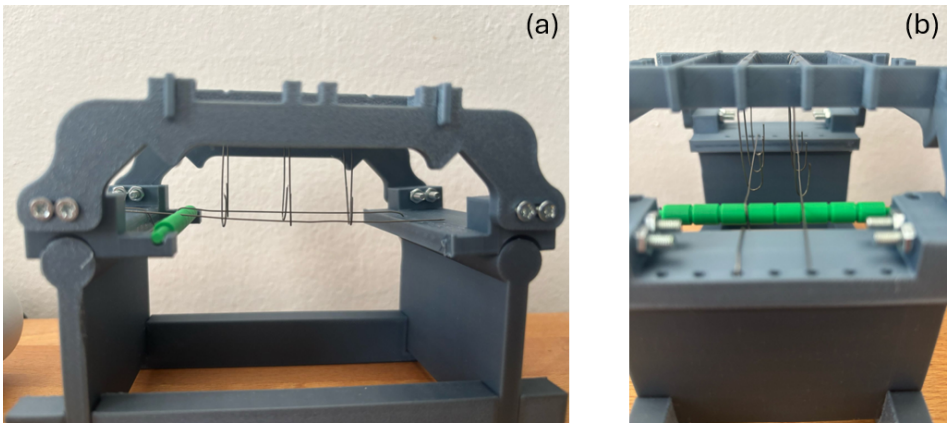

Figure 37: Tungsten loop prototype from different perspectives, (a) shows a side view, and (b) a front view.

Clamp heat distributions. The SolidWorks simulation package [71] is used to do thermal simulations. Several assumptions are made:

- In thermal radiation calculations, the spectral absorption ratio of all solids is assumed to be independent of wavelength. Their absorption is equal to their emissivity, treating them as opaque gray bodies. The radiative heat transfer of the hydrogen medium is neglected.
- It is a closed system; there is no surface-to-surface radiation to the environment.
- Convection can be neglected due to the low-pressure environment (10-15 mbar).
- Molybdenum, alumina, and tungsten are considered to be pure forms of the material.

The thermal loads applied to all concepts are:

- Temperature-1. The electrodes are assumed to be at around 300 degrees °C. This is a very rough estimate and has to be verified with a pyrometer. In reality the electrodes are cooled at one side, and passively heated by the resistive heating of the filament, but this has not been modeled.
- Temperature-2. The tungsten heated filaments have been measured in the past to be 2300 °C. In reality, this temperature is not uniform, but it has been modeled as such.
- Radiation-1. The heated tungsten wires emit radiation, for modeling the clamp temperature, surface-to-surface radiation with an emissivity value of 0.291. This emissivity value was obtained for a hemispherical tungsten object at 2500 K by Matsumoto *et al.* [72], and is used as an approximation.
- Radiation-2. In a lesser degree than the heated, the molybdenum components also emit radiation. The emissivity value of molybdenum depends on the temperature and surface roughness, based on the study by He *et al.* [73] the emissivity is estimated to be 0.2.
- Radiation-3. The emissivity value of the alumina components is estimated to be 0.43. In literature, Mayer *et al.* [74] found this value for an alumina surface at 1000 °C.
- Radiation-4 The parts of the spring and wall-spring holder in the filament straightening are estimated to be steel (in reality the spring is made of heat-resistant material like Inconel X-750, but the material library did not include these materials). The emissivity of steel is set at 0.1 [58].
- Radiation-5 The sliding block in the filament straightening mechanism are made of graphite. The emissivity of graphite is approximated to be 0.8 [58].

Filament straightening concept. The filament straightening concept is the most computationally expensive concept to model. The radiation view factor calculation takes significantly longer than the other concepts due to the additional surfaces. The result of the heat distribution simulation of this concept is shown in Figure 38.

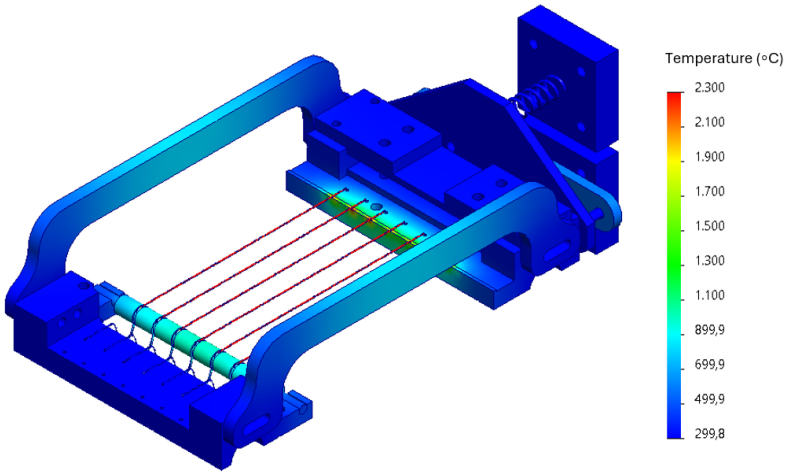

Figure 38: SOLIDWORKS simulation heat distribution of the filament straightening concept at steady state.

In this design, only the molybdenum parts make direct contact with the heated filaments. Hence, these parts will get local high temperature zones. The alumina cross beam is not in direct contact with the heated filaments, but gets heated up to 800 °C, due to radiation. The parts of the spring module gain very little heat from the heated filaments. The radiation view factor with respect to the heated filament is almost 0 here.

Cross beam. The design with the support beam underneath was also modeled. Figure 39 shows the temperature distribution of the clamp after simulation. At steady state, the result is that the temperatures of the alumina beam will reach similar tempereratures as the tungsten loops (2300 C °), the alumina components that are holding this beam will reach temperatures of ∼1500 degrees C.

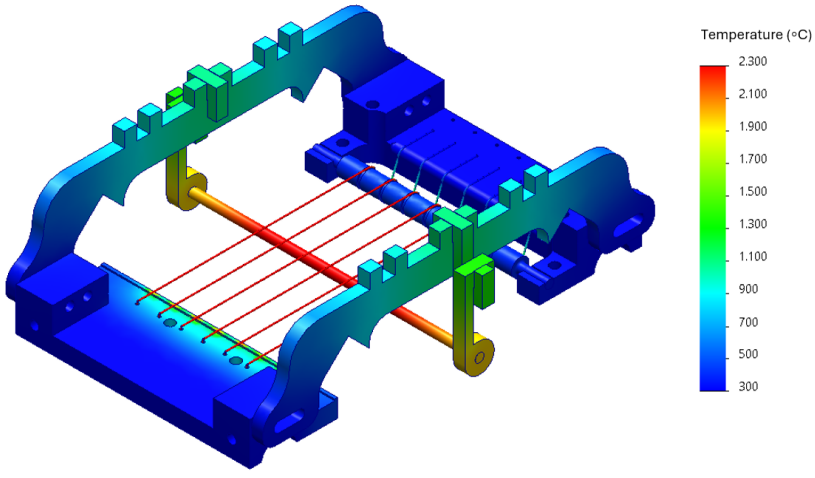

Figure 39: SOLIDWORKS simulation heat distribution of the cross beam concept at steady state.

Tungsten loops. The design with the tungsten support loop, obtained the results shown in Figure 40. This is a worst-case scenario, in which the tungsten loops make full contact with the ceramic crossbeams across the entire surface. This means that the conduction between the loops and ceramic cross beams will be very high. The result is that the ceramic parts will reach a maximum temperature of 1250 °C in this design.

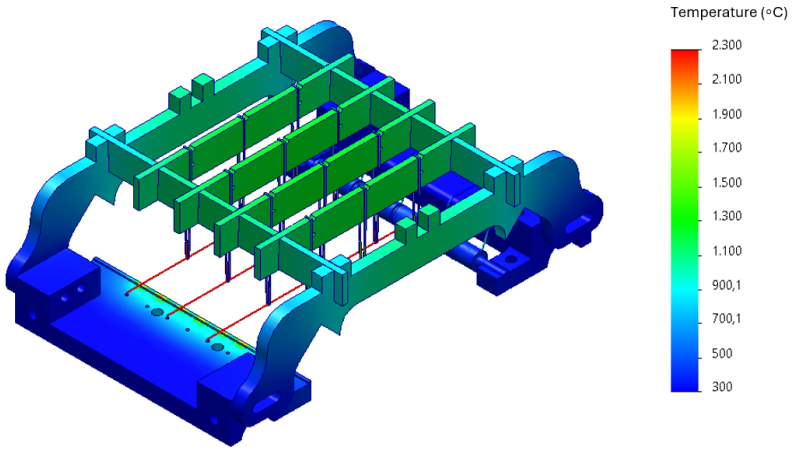

Figure 40: SOLIDWORKS simulation heat distribution of the filament loops concept at steady state.

Clamp heat simulation discussion. The goal of the simulation is to see if the alumina and tungsten parts can withstand the temperatures that they are exposed to. By modeling the heat simulation of the parts, the maximum steady state temperature can be estimated. This estimation is then used to validate whether the maximum service temperature of the material is high enough for the new clamps to work. Table 9 shows the melting and service temperatures of the relevant materials.

Table 9: Melting and maximum service temperatures of relevant materials [6]

Material (Purity (%))	Melting Temperature (°C)	Maximum Service Temperature (°C)
Molybdenum 99	2610 - 2620	867 - 1310
Alumina 99	2000 - 2100	1170 - 1230
Alumina 99.9	2000 - 2100	1760 - 1840
Quartz	1560 - 1960	1100 - 1400
Tungsten	3410 - 3420	825 - 1210
Tantalum 99.7	2990 - 3000	1370 - 1980

If the ceramic parts are manufactured from Alumina with 99.9 % purity (or similar), both the tungsten loop design and the tensile spring straightening mechanism are viable based on the simulation results. In contrast, the cross-beam concept is not feasible, as simulations indicate that the cross beam heats up to 2200 °C, which would cause the part to melt.

4.1.4 Cost estimation

Another thing to take into consideration is the monetary cost of the different concepts. For experimental testing, the design must not exceed 3000 euros. The cost of each design is shown in Table 10, the cross beam and tungsten loop are exact prices based on quota received from Gimex [75]. The cost of the straightening mechanism is only an estimate, as the quote for a heat-resistant spring has not been obtained.

Table 10: Prices of different designs

Straightening mechanism*	€ 2500 – 3500
Cross beam	€ 1365
Tungsten loops	€ 1652

4.1.5 Final design submitted for production

Due to the limited time scale of this thesis project, and the fact that no quota was obtained for the straightening mechanism. The tungsten loop concept is the most promising new clamping mechanism. It is relatively cheap, withstands hot temperatures, and is easy to manufacture. Chapter 5.1 will go over results of this new clamp. The manufacturing of the Alumina 99.7% parts took two months. In the meantime, work on the HFCVD simulations was initiated, which is presented on the following page.

4.2 Simulations

This Chapter describes the setup of the COMSOL model used to simulate temperature distributions. Introducing geometry, physics used, applied materials, boundary conditions, and roughness of the mesh. A more detailed explanation of the model setup can be found in Appendix E. More details on the geometry setup can be found in Appendix F.

4.2.1 Geometry definition

The reactor model was created in COMSOL version 6.1 [76] to allow for modification of geometrical parameters at a later stage. Figure 41 shows a schematic diagram of the simplified 3D model of the HFCVD system. The simulation is based on an array of 7 tungsten filaments positioned 1.5 cm apart from the substrate, with a 7.5 mm distance between adjacent filaments. The initial geometrical parameters are summarized in Table 11.

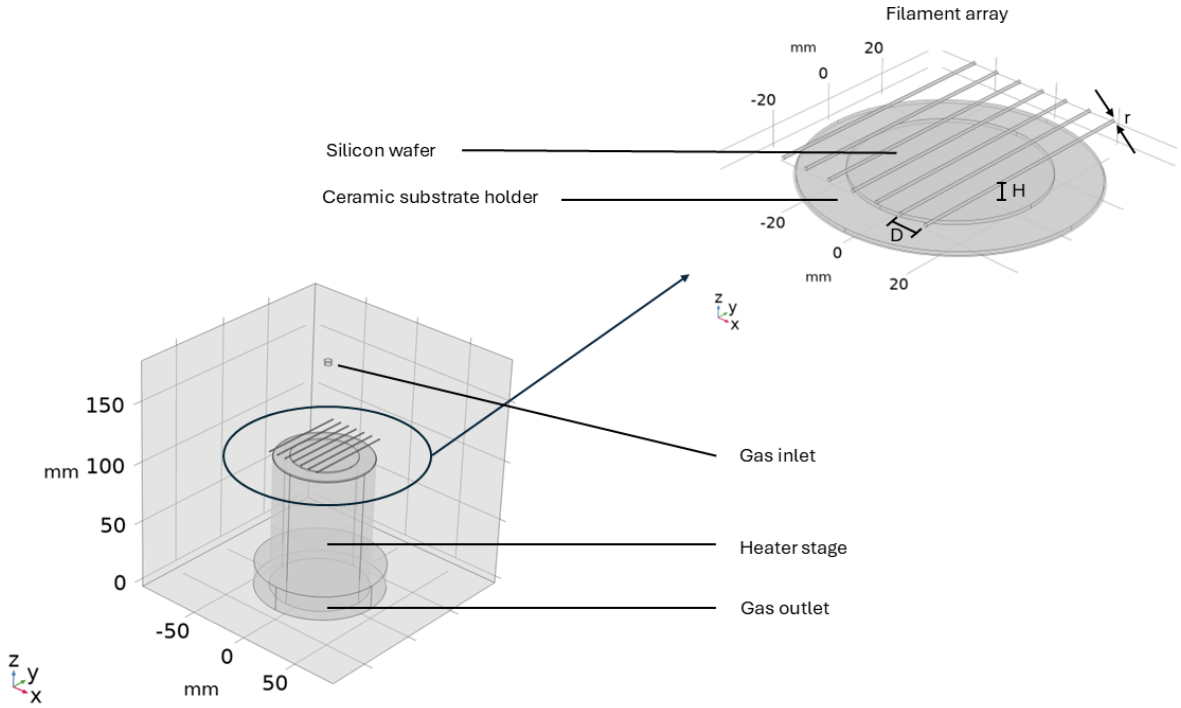

Figure 41: COMSOL HFCVD reactor geometry

Table 11: Initial filament configuration parameters

Symbol	Parameter	Starting value
D	Filament separation distance	7.5 mm
H	Filament-substrate distance	8 mm
r	Filament radius	0.5 mm
P	Power supplied to heated substrate	0 W

4.2.2 Physics interface used

Governing equations. The model utilizes laminar flow of hydrogen gas; due to the small percentage of methane (i.e.< 5 vol.%), it is assumed that the gas consists solely of hydrogen. COMSOL solves the steady-state governing equations for particle motion. The momentum and continuity equations are shown in Equations 7 and 8, respectively.

$$\rho(\boldsymbol{u} \cdot \nabla)\boldsymbol{u} = \nabla \cdot \left(\frac{p}{2}\mathbf{I} + \boldsymbol{K}\right) + \boldsymbol{F} \tag{7}$$

$$\rho \nabla \cdot \boldsymbol{u} = 0 \tag{8}$$

In the above equations, ρ denotes the fluid particle density, and $\boldsymbol{u}$ represents the particle velocity vector. The initial velocity at the gas inlet is specified as 1 m/s in the downward direction, corresponding to the vector $(0, 0, -1)$. The variable p stands for the pressure, which is initially set to atmospheric pressure (1 atm). The symbol $\mathbf{I}$ denotes the identity tensor, used here in the context of the mixing length formulation [63]. $\mathbf{K}$ represents the viscous stress tenor, and $\mathbf{F}$ the body forces acting on the fluids (such as gravity) [77].

Furthermore, heat transfer in solids and heat transfer in fluids modules are used to study the heat distribution in the reactor. The energy equation with conduction and convection is given by Equation 9. The heat flux vector is defined by Fourier's law (Equation 10).

$$\rho_s c_{p,s}\, \boldsymbol{u} \cdot \nabla T + \nabla \cdot \boldsymbol{q} = Q + Q_{\text{ted}} \tag{9}$$

$$\boldsymbol{q} = -k \nabla T \tag{10}$$

In the above equations, ρ_s denotes the solid density, and $c_{p,s}$ is the specific heat capacity of the solid at constant pressure. The thermal conductivity is represented by k, which may be a scalar in isotropic materials or a tensor in the case of anisotropic conductivity. The velocity field $\boldsymbol{u}$ is specified by the translational motion sub-node and applies when parts of the domain are in motion within the material frame. The term Q accounts for volumetric heat sources, while $\boldsymbol{q}$ is the heat flux vector governed by Fourier's law. The symbol ∇T denotes the spatial temperature gradient [63].

Additionally, surface-to-surface radiation module is used to take the radiation into account. The radiation heat flux equation can be described by Equation 11.

$$q = (1 - \rho_d)G - \varepsilon \sigma n^2 T^4 \tag{11}$$

Here, q denotes the heat flux, ρ_d represents the diffuse reflectivity of the surface, and G is the incident radiation on the surface. The symbol ε stands for the surface emissivity, while n is the refractive

index. Additionally, σ refers to the Stefan-Boltzmann constant (5.670×10^{-8} $\mathrm{W\,m^{-2}\,K^{-4}}$), and T is the absolute temperature of the surface [78].

Multiphysics. Coupling the heat transfer modules to the gas flow is done by adding the non-isothermal flow multiphysics module. Equation 12 represents the heat generated by viscous forces in the fluid (Q_{vd}). Where the viscous stress tensor for a Newtonian fluid (τ) is given by Equation 13.

$$Q_{\mathrm{vd}} = \boldsymbol{\tau} : \nabla \boldsymbol{u} \tag{12}$$

$$\boldsymbol{\tau} = \mu \left(\nabla \boldsymbol{u} + (\nabla \boldsymbol{u})^T \right) \tag{13}$$

Here, μ is the dynamic viscosity, and $\boldsymbol{u}$ is the velocity vector field. The colon symbol (:) means the double dot product is used.

The radiative surface-to-surface heat transfer is coupled with the heat transfer in solids and fluids module, using the Heat transfer with surface-to-surface radiation module. At the interface between the domain and the environment, the coupling between conductive/convection heat flux and radiation is expressed as Equation 14:

$$-\mathbf{n} \cdot \mathbf{q} = q_{\mathrm{r,net}} \tag{14}$$

where $\mathbf{q}$ is the conductive/convective heat flux vector, $\mathbf{n}$ is the outward surface normal vector, and $q_{\mathrm{r,net}}$ is the net radiative heat flux leaving the surface due to surface-to-surface radiation exchange.

Material properties. Most of the materials were directly selected from the COMSOL built-in material library [79]. Table 12 shows the properties of the used materials.

Material	**Density (kg/m^3)**	**Thermal Conductivity (W/m·K)**	**Heat Capacity (J/kg·K)**
Tungsten (filament)	17,800	175	132
Steel AISI 4340 (reactor walls)	7850	44.5	475
Hydrogen (gas precursor)	0.0899	0.1805	14,300
Silicon (substrate)	2329	130	700
SiC (substrate holder)	3216	490	690

Table 12: Thermal properties of selected materials at 0 °C and standard atmospheric pressure [79]

Additionally, COMSOL calculates the material properties of the various materials for different temperature values. Furthermore, the emissivity is not defined by COMSOL and must be obtained from literature. It depends on factors such as material, surface finish, and temperature. Therefore, values are estimated based on literature sources. For solid surfaces, emissivity is assumed constant, depending on the material and finish: tungsten (0.291 at 2500K) [72], stainless steel (0.1) [78, 49], and silicon (0.6) [80], silicon carbide (0.9) [51].

4.2.3 Boundary conditions

In the heat transfer in solids module, all domains are defined as solid except for the fluid hydrogen domain. Filament temperature can be defined by a heat flux boundary condition [49], or a uniform temperature. In the current model, three boundary temperatures are set at a fixed value. The steel wall temperature is set at 20 °C, the tungsten filament temperature at 2200 °C, While the heater stage (supplier Thermic Edge, UK; see appendix H) is set at a heat rate of 0 W, which can be increased at a later stage.

The laminar flow module is applied to the fluid domain. The reference pressure is set at 1 atm, assuming weakly compressible flow. The initial system pressure is set at 10 kPa. At the gas inlet, a fully developed flow gets in at an average velocity of 1 m/s. The outlet pressure is set at 0 Pa, suppressing backflow.

Finally, in the surface-to-surface radiation module, infinite voids have to be defined as opaque. More details on how the boundary conditions are applied can be found in Appendix E.

4.2.4 Mesh generation

The mesh is shown in Figure 42. The sequence type is defined as Physics-controlled mesh. This is a built in function in COMSOL, where COMSOL automatically selects the mesh element size and type based on the physics module, and its typical solution behavior. The mesh is finer where the solution changes rapidly, such as at the gas inlet or substrate surface. The complete mesh consists of 309982 domain elements, 17548 boundary elements, and 2232 edge elements.

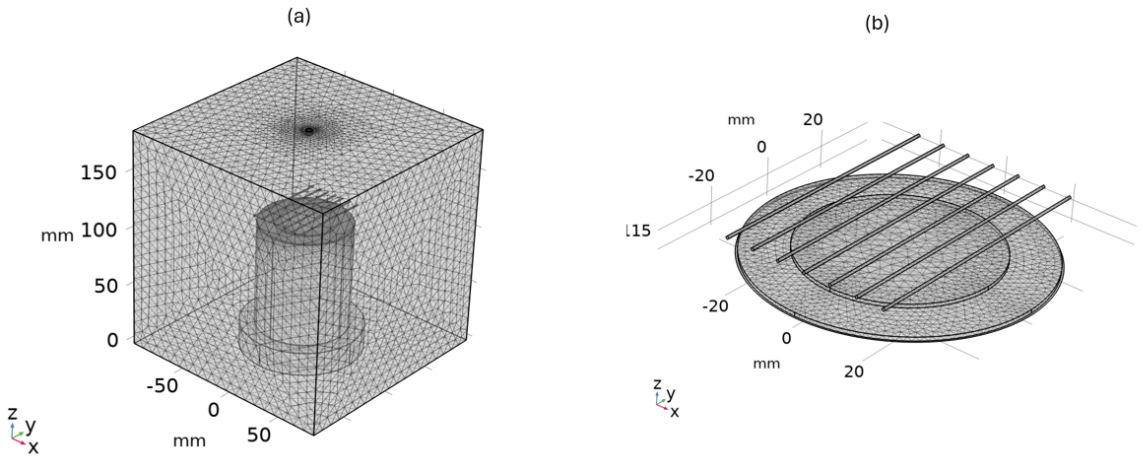

Figure 42: HFCVD reactor mesh. (a) mesh of the entire HFCVD reactor, (b) close-up of the relatively fine substrate, and filament mesh.

5 Results and discussion

5.1 Clamping device

5.1.1 Assembly and geometrical fit

Assembly. Upon arrival, the parts were assembled to see if the tab and slot connections fit as well as in the 3D-printed prototype. Fortunately, this was the case. The final clamping device can be seen in Figure 43 (a). The white parts are the new alumina parts, custom-made by Gimex [75]. The teal and green parts are temporary 3D printed parts, identical to the current molybdenum parts.
As a result, the dimensions of the new alumina clamp will be compared to the dimensions of the design. In future studies, these dimensions can be measured after a specific number of heating cycles. This can be useful to examine the effect of thermal expansion and creep on the structural integrity of the clamp.
The schematic drawing of the couple beam can be seen in Figure 43 (b). The measured dimensions here are A,B and C. A is the slot distance, B is the end-to-end distance, and C is the part thickness. Measuring with calipers, the 4 mm thick parts measured at 3.95 ± 0.05 mm, the end-to-end distance at 133.95 ± 0.05 mm, and the 4.2 mm slot was measured at 4.15 ± 0.05 mm. Indicating small manufacturing tolerances.

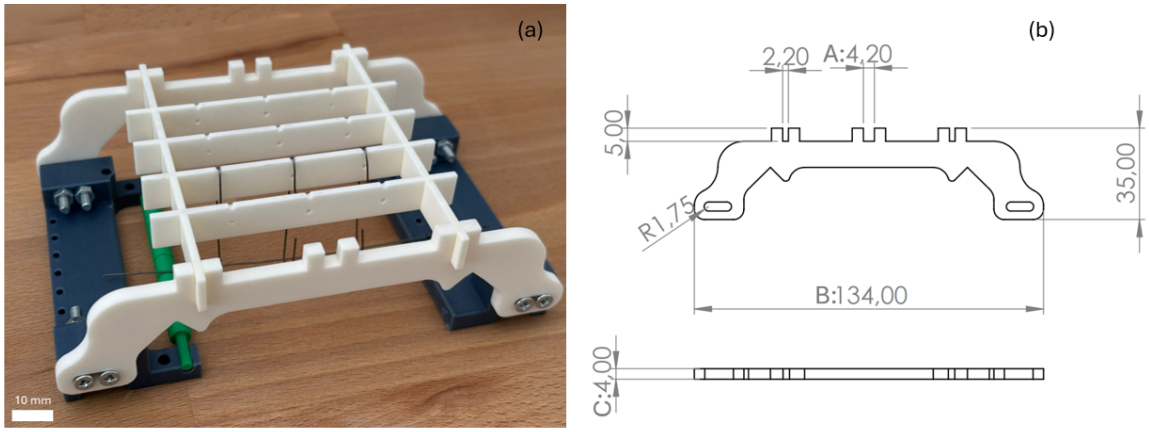

Figure 43: Tungsten loop clamping device. (a) shows a picture of the assembled alumina 99.7% parts, (b) a schematic drawing of the couple beam

Table 13: Dimensional differences after production

Dimension	A (mm)	B (mm)	C (mm)
Designed	4.20	134	4
Produced	4.15 ± 0.05	133.95 ± 0.05	3.95 ± 0.05

Geometrical fit. Figure 44 illustrates the geometrical fit of the new clamp inside the reactor, confirming that it integrates into the setup without any issues. In addition, a dedicated device, referred to as the "fork," has been developed to insert and remove the clamp. This device is particularly valuable given the limited space within the reactor, where manual handling would be both difficult and prone to contaminating the environment.

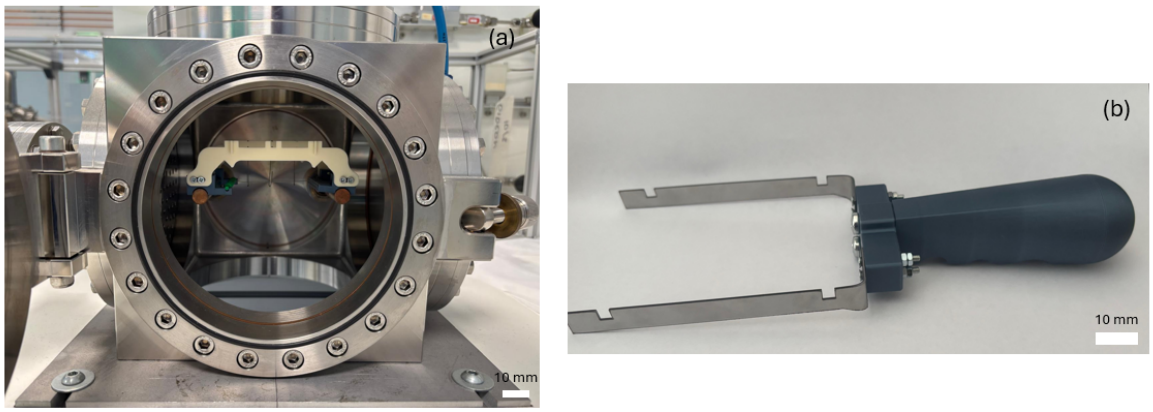

Figure 44: Geometrical fit of the new clamp inside the reactor setup (a), and fork (b).

5.1.2 Future test plan.

Once the heater stage has been successfully integrated into the HFCVD setup, additional testing should be conducted. First, the structural integrity of the clamp should be evaluated after varying numbers of heating cycles (e.g., 1, 10).
In addition, the degree of filament sagging in the new clamp should be quantified as a function of time during a single heating cycle. The lifetime of a tungsten loop, and hot filament should also be assessed.
Finally, the influence of the new clamp on diamond quality should be investigated. Raman spectroscopy, in combination with SEM imaging, will provide valuable insight into the resulting diamond characteristics. Hopefully, the diamond quality will improve at longer deposition times. For now, this thesis will commence with the exploration of HFCVD simulations in the next Chapter.

5.2 Simulations

This chapter will give an overview of the temperature distributions obtained on the wafer and the gas flow profile. The starting parameters are defined previously in Table 11. Additionally the parameters will be varied in order to optimize temperature distribution on the wafer. Lastly, the effect of the filament sagging on the wafer distribution temperature profile is simulated. For clarity, the different types of simulations and image views are represented by different icons, which can be seen in the upper-right corner of the respective image. The corresponding icon to the HFCVD reactor simulation is displayed in Figure 46. A more elaborate explanation on the icons and their meaning can be found in Appendix G.

5.2.1 Starting parameters

This subsection gives an overview of the results obtained from simulating the HFCVD reactor setup using the initial parameters (Table 11). Starting with the temperature distribution results, and ending with the hydrogen flow profiles.

Temperature distribution. The result of the numerical computations of the temperature distributions in side view, top view at substrate level, top view at filament level, and the substrate temperature curve along y = 0 are shown in Figure 45.

Comparing these temperature plots visually with literature modeling data gives similar temperature profiles to the study by Song *et al.* [56]. Most noticeable is the higher temperature at the edge of the substrate, where heated filaments do overlap (Figure 45 (c)). The side view profiles are different in terms of temperature, because Song et al. did not consider an inlet gas velocity. Figure 45 (a) shows the cold hydrogen gas cooling down the reactor environment.

Figure 45 (d) shows the temperature curve on the substrate surface level at y = 0. The substrate surface mean temperature at the starting parameters was $\mu = 698.15$ °C, with a standard deviation of $\sigma = 3.67$ °C.

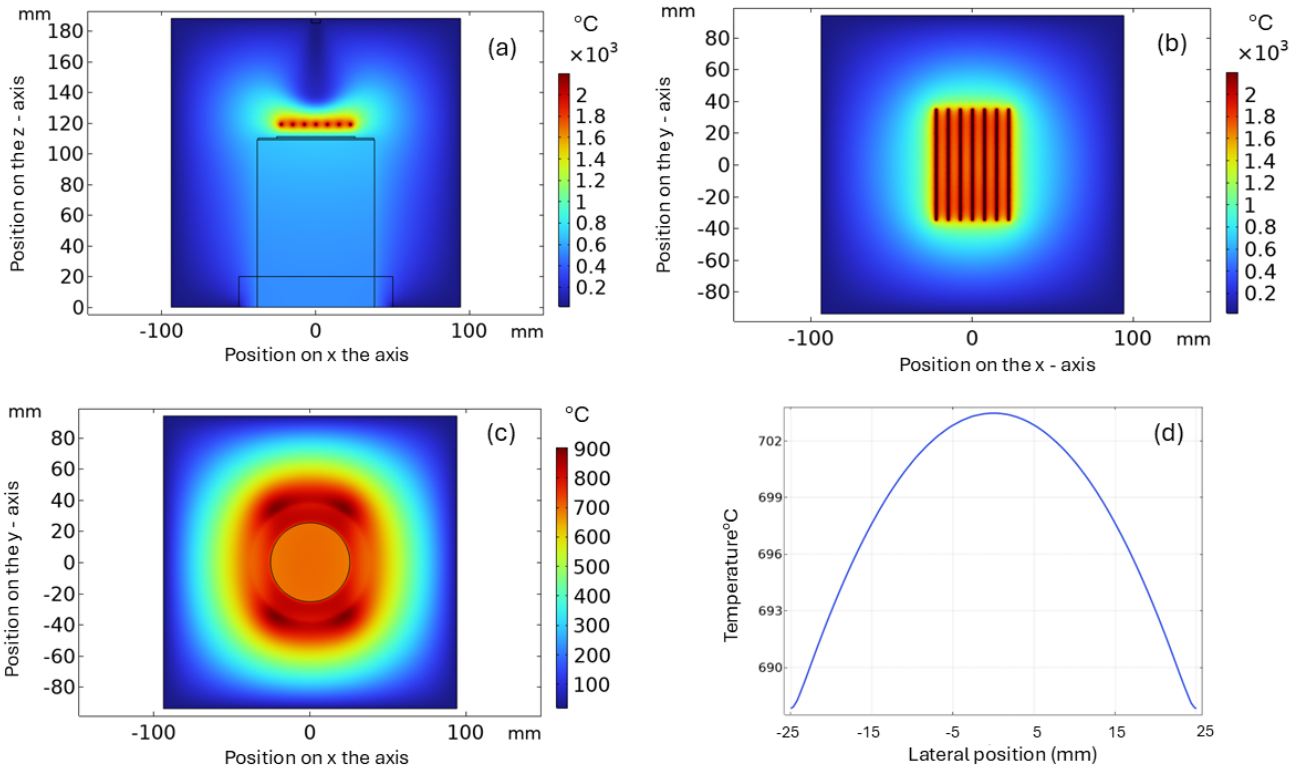

Figure 45: Different views of PME HFCVD reactor simulation temperature distribution results. (a) shows the side view temperature distribution, (b) the top view temperature distribution at filament level, (c) the top view temperature distribution at the substrate surface, (d) the substrate temperature curve at y = 0 in the XZ plane.

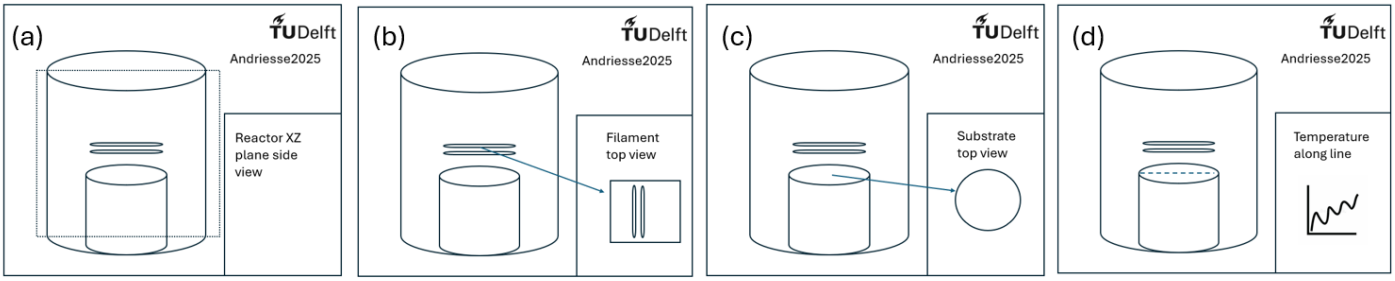

Figure 46: Corresponding logos to Figure 45 (a), (b), (c), (d). Further clarifying the view.

Laminar flow. Simulating the hydrogen flow in the HFCVD reactor is crucial for understanding gas transport and heat distribution. Hereafter, the results of simulations regarding the hydrogen flow are presented. In a later stage, this can potentially be used to optimize gas density or gas flow.

Figure 47 (a) shows the velocity magnitude of the gas stream, whereas Figure 47 (b) shows the streamline paths of the gas inside the reactor. Figure 47 (c) shows the hydrogen gas density. Finally, Figure 47 (d) displays the hydrogen gas density top view. Figures 47 (a), (b), and (c) correspond to the view displayed by Figure 46 (a), while Figure 47 (d) corresponds to the view in Figure 46 (b).

The plots indicate that the amount of hydrogen gas reaching the middle filament is greater than that reaching the outer filaments. Future studies could explore alternative gas inlet and outlet configurations, such as using an array of inlets. This approach, as demonstrated by Song *et al.* [56], may provide valuable insights for potential improvements. Furthermore, the gas flow is very slow (order $10^{-3}m/s$) at the blue area in Figure 47 (a). In reality, the gas gets pumped out at a higher velocity.

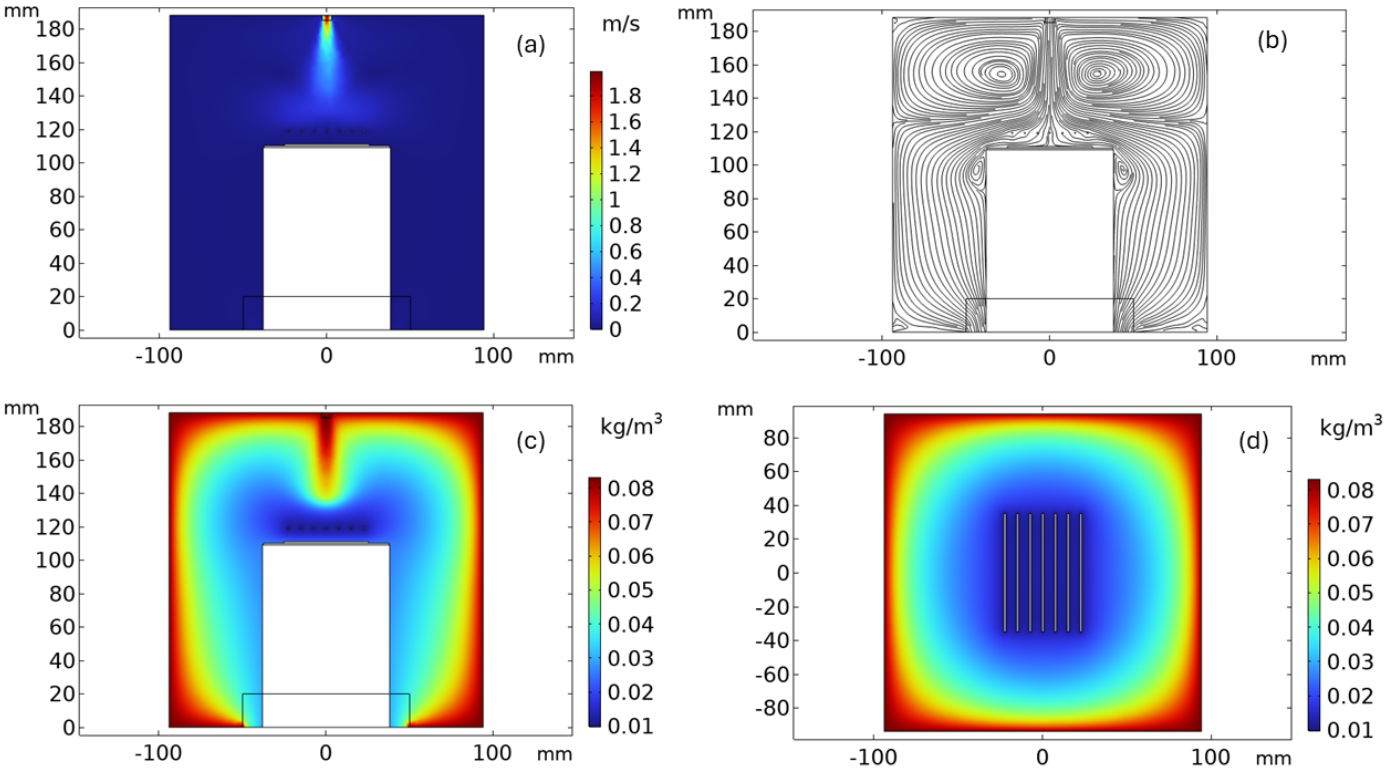

Figure 47: Laminar flow of hydrogen gas: (a) velocity magnitude distribution, (b) streamline plot of the gas flow, (c) hydrogen gas density distribution (side view), and (d) hydrogen gas density distribution (top view at filament level).

5.2.2 Validation using literature

Purpose of validation. Due to ongoing maintenance on the heated stage, experimental validation of the HFCVD model is currently not feasible. Instead, the model has been validated through comparisons with existing literature. Numerous studies have been conducted on simulating temperature distributions in HFCVD reactors (Table 14). Some of these models have been experimentally validated by placing thermocouples or thermometers inside and on the reactor during diamond deposition. Reproducing one of these validated models with the boundary conditions applied in my HFCVD model will provide a meaningful assessment of its accuracy.

Description of literature model. For the validation different HFCVD heat distribution studies were compared on usability for validation. As can be seen in Table 14, Wang *et al.* [51] was the only group that experimentally validated their simulations, and accurately described the used parameters and geometries. Their study focused on developing a HFCVD apparatus optimized to reduce the thermal budget (mainly electrical power consumption) during diamond film synthesis, which is crucial for cutting down production costs. Figure 48 shows the comparison between the simulation and experimental results, the original measurements (OM) are relevant here. It can be seen that the simulated substrate temperatures are sligthly lower than the measured ones. This is to be expected, because the chemical reactions, which are exothermic, are ignored. The result is that the deviations between the simulated temperatures and measured temperatures are always less than 45 °C, which demonstrates that this model is sufficiently accurate for optimizing the reactor configuration.

Table 14: Summary of relevant simulation studies on HFCVD Systems

Author	Date	Objective	Simulation method	Experimental verification (y/n)	Well-defined geometry (y/n)	Similar to PME setup (y/n)
Choi [49]	2023	Worktable temperature prediction	ANSYS-FLUENT (20.1)	yes	no, figures only	yes
DebRoy [55]	1990	Optimal gas flow configuration	Numerical simulation	yes	no, figures only	no
Hao [59]	2024	Effect of filament spacing on uniformity of temperature field	ANSYS R15.0	yes	no, figures only	yes
Panickar [57]	2019	Optimize substrate temperature distribution	ANSYS-FLUENT	no	yes	yes
Song [56]	2017	Relation between power and filament/substrate temperature	ANSYS-FLUENT (17.0)	yes	no	yes
Wang [51]	2024	Reduce electrical power consumption in HFCVD apparatus	ANSYS-FLUENT	yes	yes	yes
Wolden [50]	1992	Minimize temperature variation across substrate	Numerical simulation	yes	no	no
Wu [78]	2021	Influence of key parameters on substrate temperature distribution	COMSOL Multiphysics	yes	no	yes
Zhang [53]	2012	Influence of key parameters on substrate temperature distribution	ANSYS-FLUENT	yes	no	no

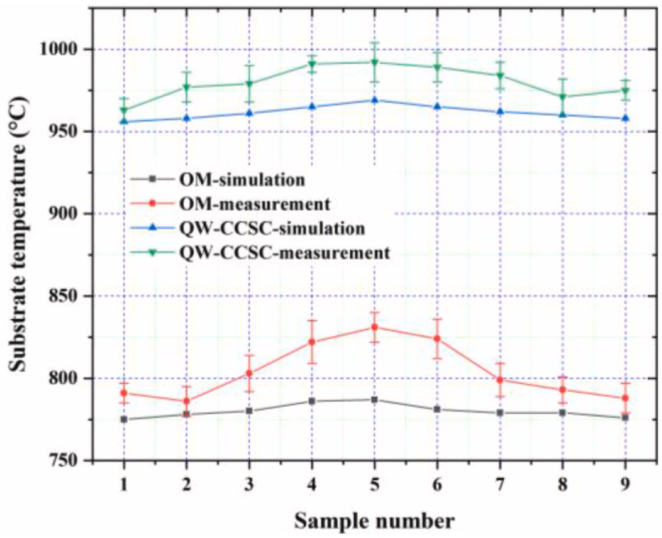

Figure 48: Comparison between simulations and experimental results (substrate temperatures) by Wang *et al.* [51]. OM stands for original model, QW-CCSC for quartz worktable and circular ring copper shielding case.

Reproduction of literature model in COMSOL. This part will explain how of Wang *et al.* [51] was reproduced in COMSOL.

Geometry definition. This reported model was chosen because it sufficiently explains the geometry and was experimentally validated. The reactor dimensions given are shown in Table 15:

Table 15: Component dimensions in the HFCVD model based on the study by Wang *et al.* [51]

Geometry	**Size (mm)**
Stainless steel reactor	∅ 400 × 300
SiC substrates	12 × 12 × 5
Graphite top worktable	200 × 100 × 20
Cu bottom worktable	220 × 120 × 60
Ta filaments	∅ 0.6 × 130

This is sufficient properties to remake the geometry in COMSOL. However, some information is still missing, which will reduce the accuracy of the replicated model. Among others, the separation distance between the 9 SiC was not given. So, this distance was set at 12 mm (estimated from published reactor pictures, see [51])

Materials. Materials are selected from the COMSOL built-in library. The reactant gas is simplified as pure hydrogen, as it accounts for over 95 % of the gas mixture in the actual CVD process. Hydrogen is also chosen due to its relatively high thermal conductivity compared to other reactant gases.
The water-cooled base is made of copper, while the worktable is constructed from graphite. The nine substrates are composed of silicon carbide, and the heated filaments are made of pure tantalum.

Boundary conditions. The following set of boundary conditions is used:

Laminar flow.

- A fully developed flow with a velocity of 0.1 m/s is added to the gas inlet
- The outlet pressure is set at 0 Pa, supressing backflow.

Heat transfer in solids.

- A fluid domain is added to the hydrogen domain, the rest is defined as solid material.
- A convective heat flux of 3 W/m^2 is added to the reactor walls.
- The temperature of the heated filaments is set at 2200 °C.
- The ambient temperature is defined as 26 °C.

Surface to surface radiation.

- Added surface emissivity with a value of 0.38, 0.9, 0.9, 0.59, and 0.7 for the tantalum, SiC, graphite, copper, and stainless steel boundary surfaces, respectively.

Comparison of results. Herein, the results of the replicated study will be shown and compared with the values found by Wang *et al.* [51]. The study did not show a temperature side view, but as this gives a better understanding of the heat transfer paths, the result of the replication is shown in Figure 49.

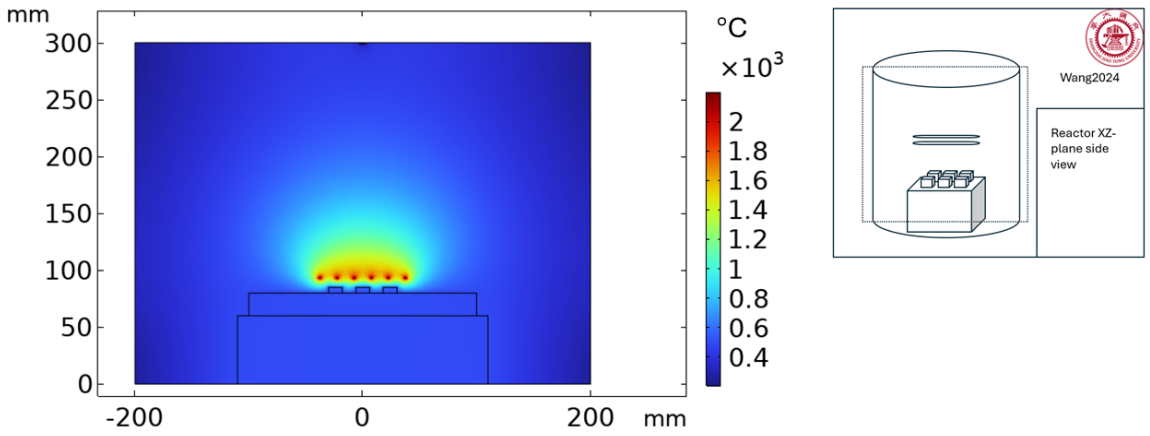

Figure 49: Side view temperature distribution of the replicated model of the reactor geometry reported by Wang *et al.*[51].

The substrate temperature distribution is shown in Figure 50 (a), and Figure 50 (b) shows the average temperature of the samples, in the same format as in the study (Figure 48).

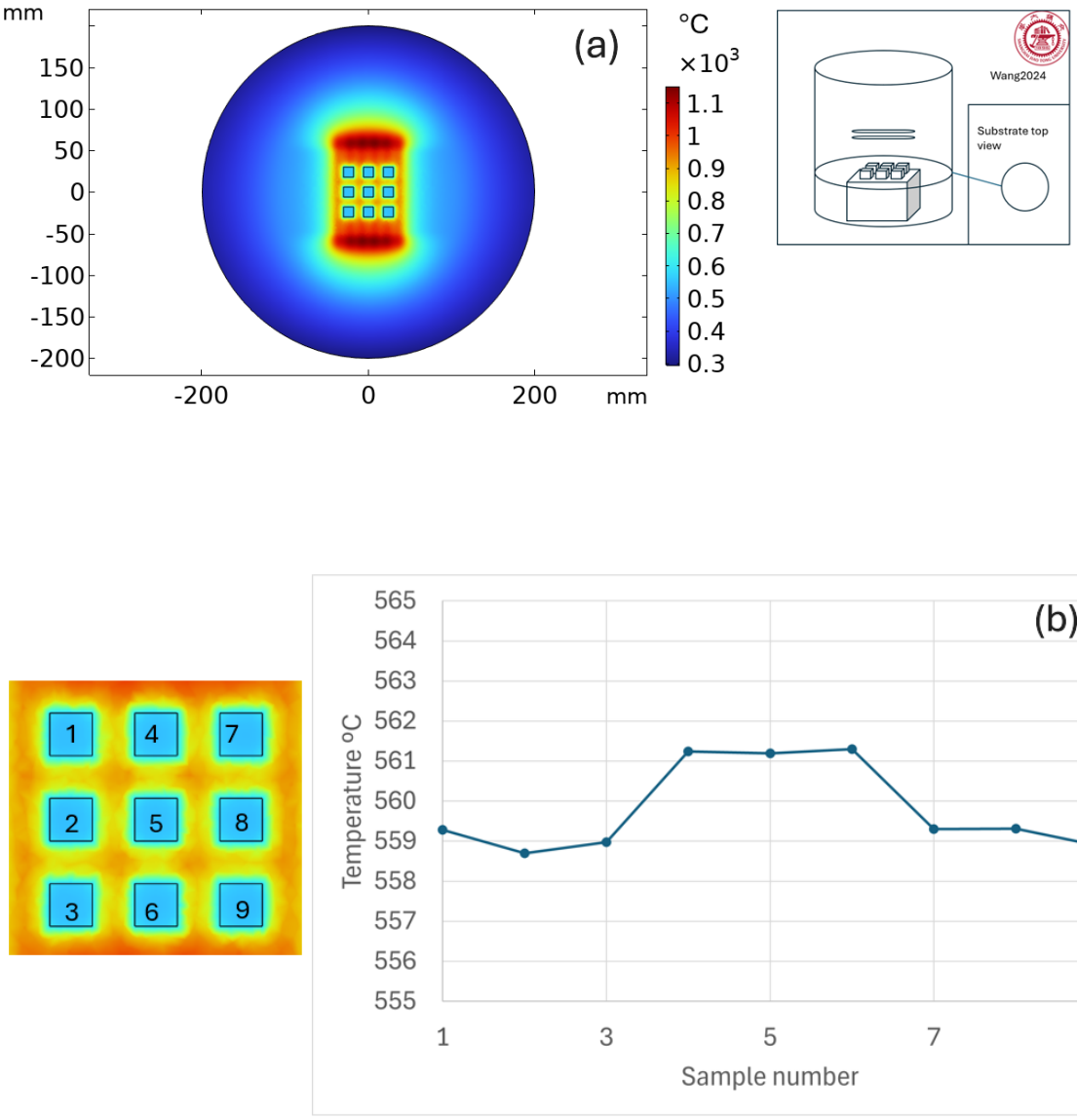

Figure 50: Modeling replication of the 2D substrates (a), and averaged 1D sample temperature profiles (b) according to the specifications in the study by Wang *et al.*[51]

Replication outcome and discussion. Wang *et al.* [51] obtained an average sample temperature of ≈ 775 °C. The present replicated study obtained an average sample temperature of ≈ 560 °C, a -20% decrease in absolute temperature (K). Thus, the replication is not sufficiently accurate to verify the accuracy of the original HFCVD setup model. There are several possibilities that explain this difference:

The main difference between the parameters used in the Wang replication, and the PME model is the reported emissivity used for the stainless steel boundary surface. Wang *et al.* [51] used an emissivity value of 0.7, while the PME model used an emissivity of 0.1. A lower emissivity leads to a higher substrate temperature, because more heat is reflected from the boundary surface back to the substrate. As a result, the emissivity value in the replication study was changed from 0.7 to 0.1. This led to a substrate temperature increase, but only around 20 °C. Hence not explaining the large inaccuracy in the original model.

When we look at the temperature profile along the x-direction (Figure 51 (a)), a big temperature drop is observed. The substrates conduct a lot of heat to the substrate holder. In reality, the contact between the substrate and substrate holder is not perfect due to surface roughness, and the substrate cannot conduct as much heat. Hao *et al.* [59] applied this surface roughness in their COMSOL model and found a trend similar to the black dotted line in Figure 51 (a). This could be the issue leading to the discrepancy. However, it is unlikely because Wang *et al.* [51] do not mention taking surface roughness, and/or contact pressure into account. Unfortunately, lacking modeling skills leaves this question open.

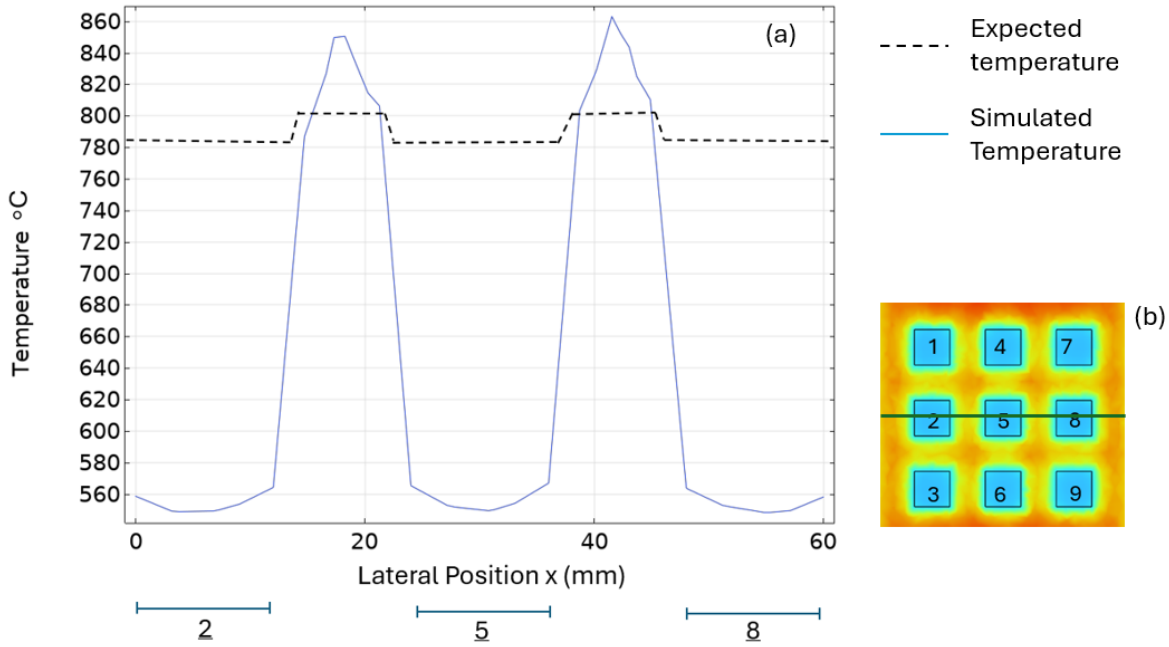

Figure 51: Temperature profile along x-direction at y=0, (a) shows the difference between expected results and simulated results, (b) the line along which the temperature is measured.

5.2.3 Parametric sweeps

Parametric sweeps are a way to systematically vary one or more input parameters to observe how they affect the outcome. In this study, the aforementioned parameters (Table 11) are varied to obtain their influence on the substrate temperature.

Filament-substrate distance. The filament-to-substrate default value was set as 8 mm. The starting parameter value was set as 6 mm, and the end at 10 mm, and by applying a step size of 1 mm, a total of five temperature profiles were obtained. The results are shown in Figure 52. This shows a higher temperature, with more ripples in the graph, for a lower filament substrate distance. The temperature jumps between each distance plot range from 16 to 21 °C.

Filament-filament distance. Figure 53 shows the parametric plot of the influence of the filament-filament distance. What can be observed is an increase in the temperature as the filaments approach each other. The problem with this plot is that it does not solely study the influence of the filament-filament distance. When the filaments get too close, a temperature drop off can be seen. This is because the 7 filaments are not enough to span the entire 2-inch wafer. Hence, a new simulation was done, this time with 10 filaments. Figure 54 displays this result.

This increase in filaments leads to an average temperature increase, which is to be expected. The temperature drop off on the sides, which could be seen in Figure 53 is no longer present. There is still an increase in temperature in the middle of the substrate when filaments are closer to each other, most probably due to higher conductive heat transfer. The gas flow is highest in the middle, where the relatively small gas-inlet nozzle is placed.

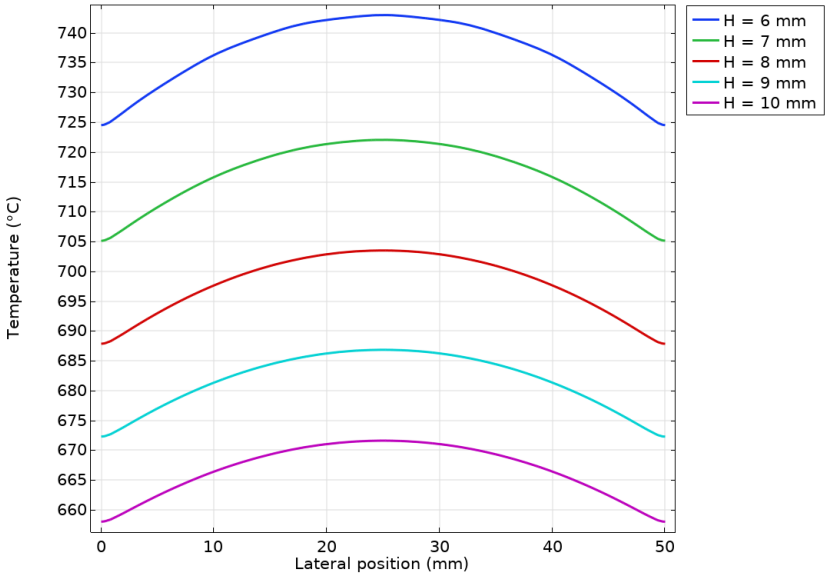

Figure 52: Substrate temperature curves in the XZ-plane for different **filament-substrate distances** H, in each case P=0 W, r=5 mm, D=7.5 mm.

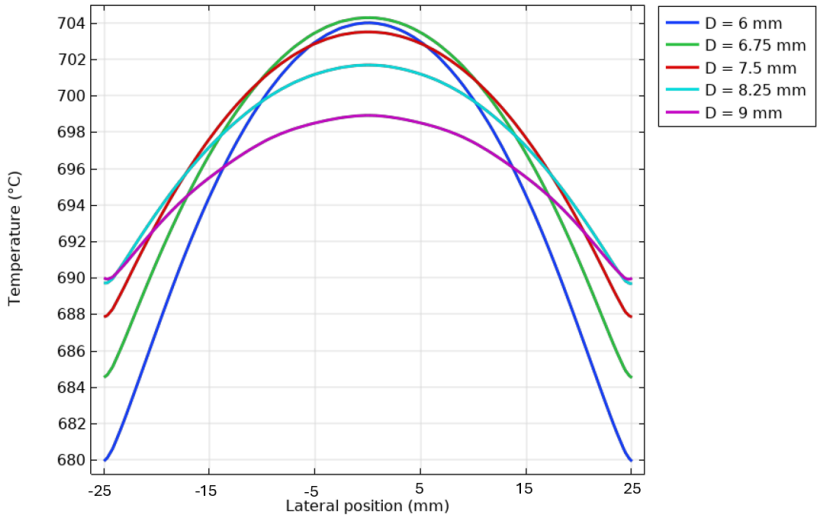

Figure 53: Substrate temperature curves in the XZ-plane for **different filament-filament distances** D, in each case P=0 W, r=5 mm, H=8 mm. The setup includes 7 heated filaments.

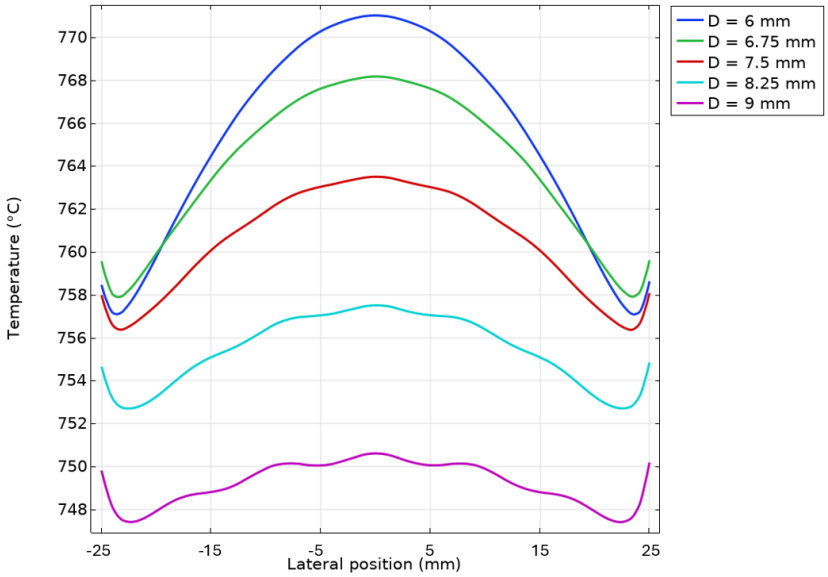

Figure 54: Substrate temperature curves in the XZ-plane for different **filament-filament distances** D, in each case P=0 W, r=5 mm, H=8 mm. The setup includes 10 heated filaments.

Filament radius. The filament radius default value was set at 5 mm, the starting value at 2 mm, and the final value at 6 mm. Figure 55 shows big temperature jumps when increasing the filament radius, ranging from 39 to 58 °C. The radius does not have much influence on temperature uniformity, but does have a large influence on average substrate surface temperature.

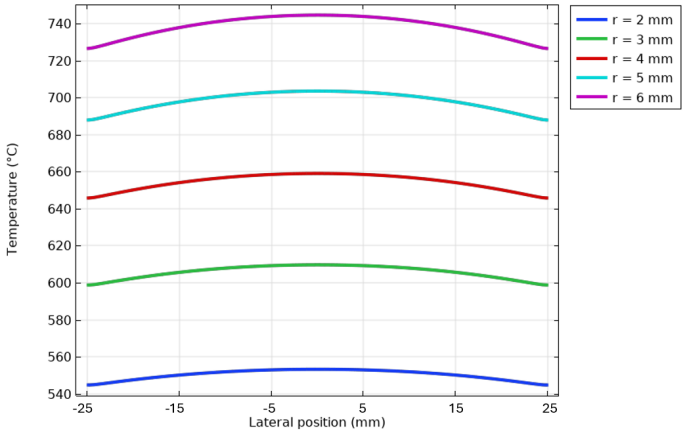

Figure 55: Substrate temperature curves in the XZ-plane for different **radii of the filament**, in each case P=0 W, D=7.5 mm, H=8 mm.

Power at heated substrate. A power input was simulated on the heater stage domain. The starting parameter was set to 0 W, and subsequently increased in 200 W steps to 1 kW. This gives an indication of how much power must be supplied to the heater stage, when for example less filaments are used. The accuracy is limited, and has to be validated. This is due to the in reality much more complex geometry of the heater stage (Appendix H).

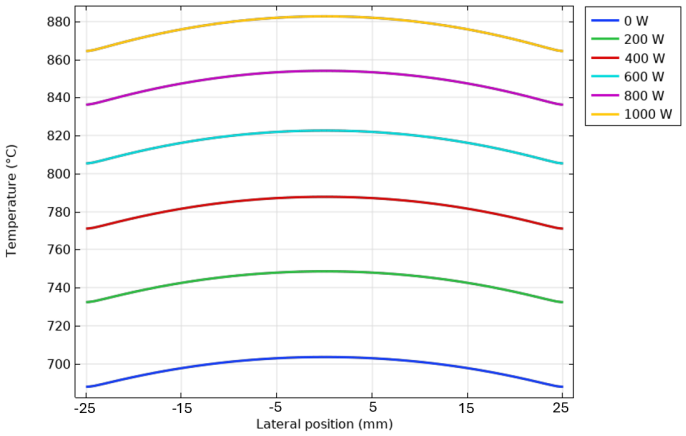

Figure 56: Substrate temperature curves in the XZ-plane for different **power inputs** at the heated stage, in each case r=5 mm, D=7.5 mm, H=8 mm.

Comparison parametric sweeps with literature. Several studies have compared different geometrical parameters to optimize diamond growth across various reactor sizes, including those by Hao et al. [59], Wu et al. [78], Panickar et al. [57], and Zhang et al. [53]. This subsection compares the trends obtained in literature with the plots obtained by the aforementioned simulations.

Firstly, Hao *et al.* [59] studied the influence of filament spacing (called Tw in their study). Nine square YG6 substrates were coated in their setup, similar to Wang *et al.* [51]. The results of Hao *et al.* [59] are shown in Figure 57 [59].

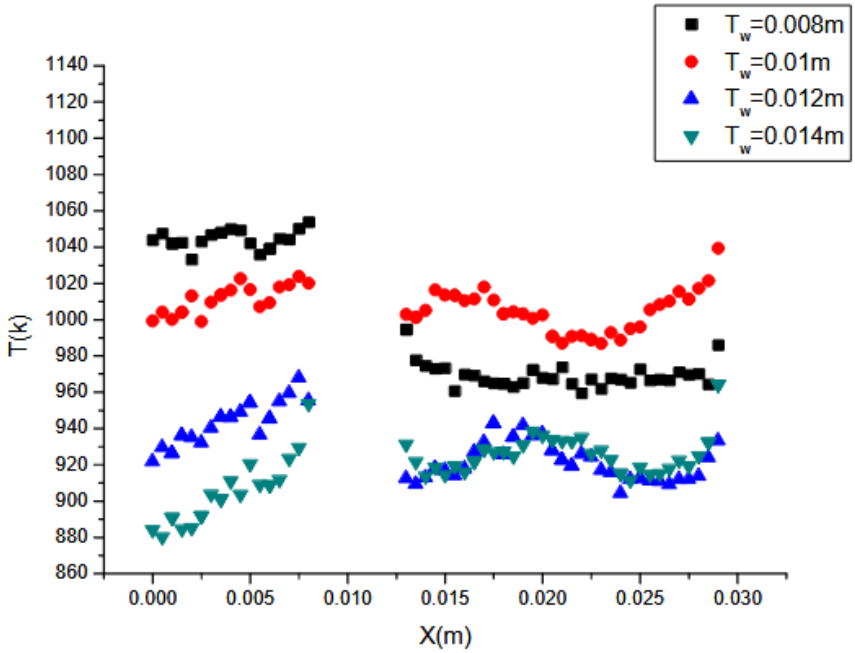

Figure 57: Influence of Tw on the temperature of substrate along X direction [59].

The trend they found was that the smaller Tw, the higher the temperature on the substrate surface, with a high temperature in the middle of the substrate, and a low temperature on the sides. With the increase in Tw, the distribtution of the hot filament over the substrate tended to spread out. Comparing this to Figure 54, similar results are observed. A small D/Tw leads to a higher convective heat transfer and concentrated heat radiation made the temperature in the middle of the substrate higher in both cases. In addition, a too high D/Tw leads to a relatively even distribution of temperature in both plots. Comparing the temperature ranges, it has to be noted that D/Tw is 8.25 mm for the PME reactor and 8 mm for the reactor by Hao *et al.* [59]. The mean temperature of the PME reactor is around 698 °C, while the mean temperature of the system reported by Hao *et al.* [59] is 767 °C, a similar temperature range. Additionally, Hao *et al.* [59] studied utilizing non-equidistant filament-filament distances, leading to even better temperature distributions.

The results of Zhang *et al.* [53] are shown in Figure 58. When we compare the trend in filament separation distance (Figures 53 and 58 (a)) the distances used by Zhang *et al.* are bigger, due to a bigger substrate being coated. In both cases, increasing D leads to a lower average temperature while decreasing D leads to a higher temperature peak in the middle.
Comparing different filament-substrate heights (Figures 52 and 58 (b)) also gives a very similar plot. A higher H leads to a lower substrate temperature, while a lower H leads to dispersion in both plots. Finally, comparing the different filament radii (Figures 55 and 58 (C)) shows a similar trend, in which increasing the radius increases the substrate temperature. The lines are also of similarly low slope in both plots. However, the temperature drop in the study by Zhang *et al.* is way bigger, T$\approx$ 130 °C vs $\approx$ 40 °C in the present study.

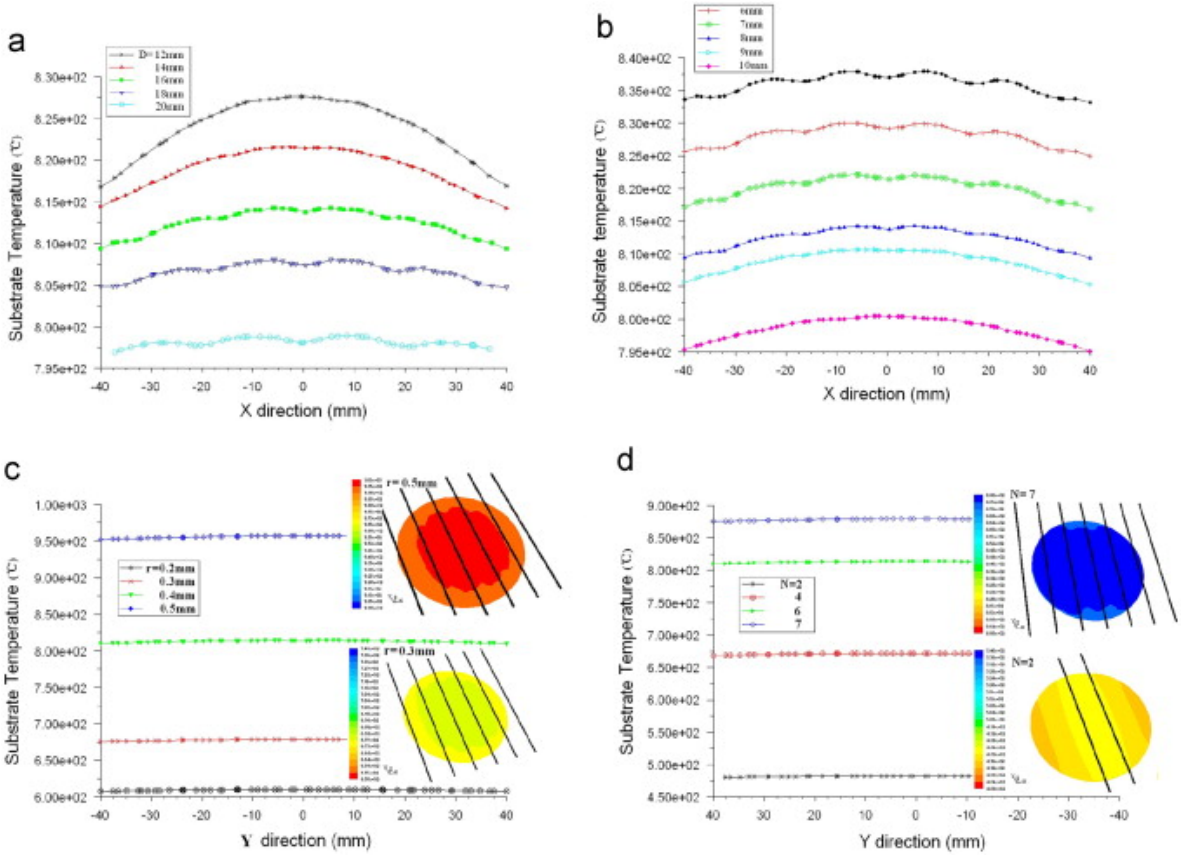

Figure 58: Comparison of calculated substrate temperature curves for (a) different filament separation, in each case r = 0.4 mm, N = 6, H= 8 mm; (b) different filament-substrate distance, in each case r = 0.4 mm, N = 6, D = 16 mm; (c) different radius of the filament, in each case N = 6, D = 16 mm, H = 8 mm and (d) different filament number, in each case r = 0.4 mm, D = 16 mm, H = 8 mm [53].

5.2.4 Sagged filaments

During long deposition runs in HFCVD the filaments undergo mechanical deformation due to thermal stress and prolonged exposure to high temperatures. Former MSc student Dilpreet Sing [29] imaged this occurrence of sagging in the PME HFCVD reactor. Appendix I explains how geometry (Figure 59) of a sagged filament after 148 hours of deposition was obtained. This geometry was then simulated using the same boundary conditions as the straight filaments (Section 5.2). The influence of the sagged filament is shown in Figure 60. Figure 60 (a) shows the temperature distribution contour on the 2-inch wafer with straight filaments. In contrast, Figure 60 (b) shows the temperature distribution on the 2-inch wafer in the most extreme case; after 148 hours of diamond growth.

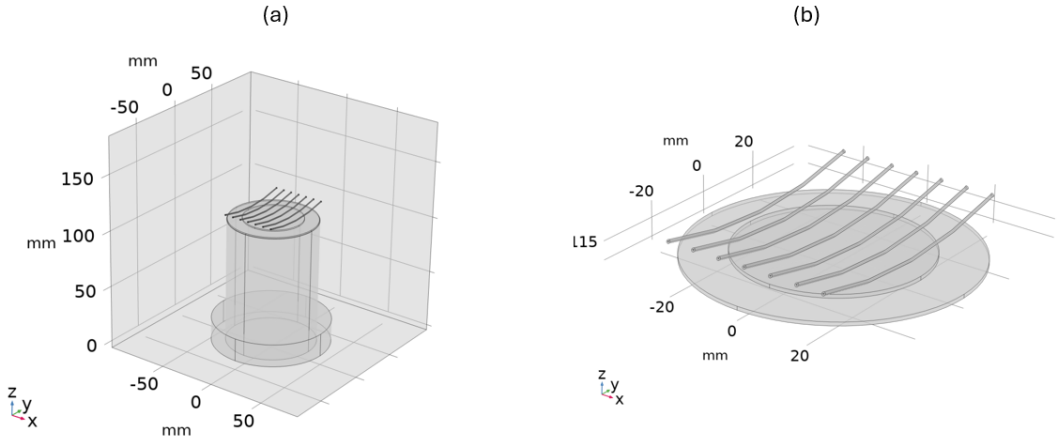

Figure 59: COMSOL geometry sagged filament after 148 hours of diamond growth. (a) shows the entire HFCVD reactor geometry, (b) offers a close-up of the sagged filament geometry.

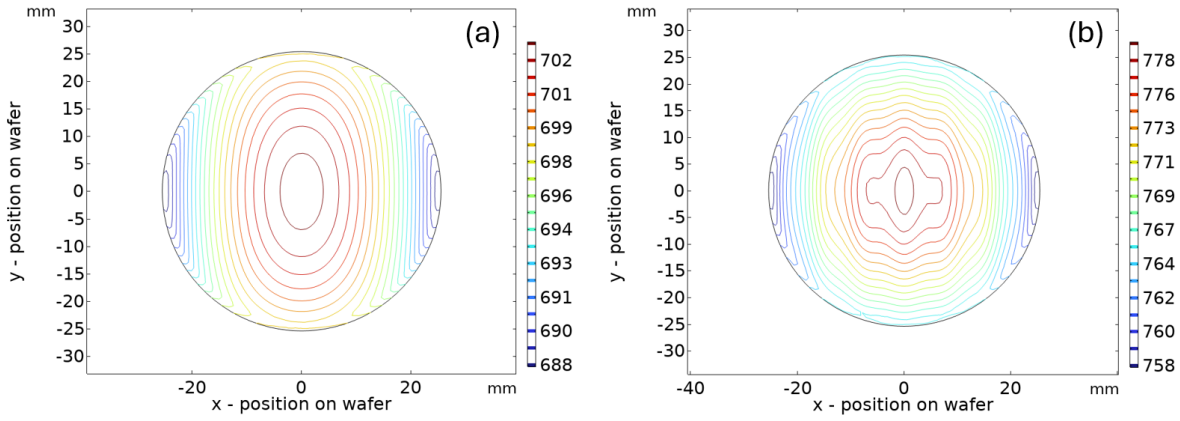

Figure 60: Contour plot of the temperature distribution on a 2-inch wafer. (a) after 0 hours of diamond growth (straight filaments), (b) after 148 hours of diamond growth (sagged filament).

What can be observed from Figure 60 is a higher average substrate temperature of 71 °C. Additionally, the temperature distribution in the case of the sagged filament is less uniform, undesirable in HFCVD diamond growth. Table 16 shows the measured average temperatures, temperature ranges, and temperature standard deviation of the substrate surface. This suggests that filament design, support structures, or active temperature compensation methods are necessary to ensure stable and uniform growth conditions during long deposition runs.

Table 16: Comparison of temperature values for straight and sagged filaments.

	Straight filaments (0 hrs)	Sagged filaments (148 hrs)
Substrate surface average temperature	698.15 °C	769.15 °C
Range (max–min temp)	15.67 °C	22.60 °C
Standard deviation	3.67 °C	5.33 °C

Despite decades of HFCVD modeling, no prior work has explicitly examined how a sagged filament alters substrate temperatures. All published studies (Chapter 2.4.2, Table 4) assume perfectly straight filaments, leaving a clear gap when it comes to real-world substrate temperature profiles. This COMSOL model represents the first quantification of sagging's thermal impact: After 148h of operation, filament sagging raised the wafer's mean temperature by approximately 71 °C, while simultaneously increasing the standard deviation from 3.67 °C to 5.33 °C. This information can be used as a starting point to study the relation between filament sagging and diamond quality if model accuracy is improved, or experimental testing can be used.

6 Conclusion and recommendations for future work

6.1 Conclusions

This thesis presents a study aimed at improving diamond film growth in a newly developed hot-filament chemical vapor deposition (HFCVD) setup at TU Delft. The research focused on two objectives: the design and fabrication of a novel filament clamping mechanism, and the development of a multiphysics simulation model of the home-built reactor to optimize deposition parameters.

Three novel filament clamp concepts were developed: one that straightens the filament using heat-resistant springs, another that supports the hot filament with an additional cross beam, and a third that utilizes tungsten loops for support. Each concept was evaluated through prototyping and thermal simulations to assess its mechanical stability and thermal performance. Among these designs, the tungsten loop concept proved to be the most promising due to its high thermal resilience, ease of manufacturing, and cost-effectiveness. Although the tungsten loop clamp has been successfully manufactured, experimental testing could not be performed within the timeframe of this thesis due to ongoing maintenance issues with the reactor.

As a result of the maintenance issues, another problem was solved. Developing a digital model of the temperature and gas distributions of the HFCVD reactor. Temperature and gas flow profiles were obtained for the starting deposition parameters. Furthermore, parametric sweeps revealed the influence of filament spacing, radii, and substrate heating power on substrate temperature distributions. The filament–filament distance (D) has the greatest influence on temperature non-uniformity. When $D < 8.25$ mm, the temperature range across the substrate increases. In contrast, when $D > 8.25$ mm, the average substrate temperature decreases, and the amplitude of periodic temperature fluctuations grows. Simulations also showed that filament sagging negatively affects substrate temperature uniformity, the standard deviation of substrate temperature went from 3.67 °C to 5.33 °C after 148 hours of diamond growth. This underscores the importance of mechanical stability during long deposition runs.

Although the simulation results show trends consistent with literature, limitations remain in the accuracy of absolute temperature predictions. When literature-based deposition parameters are applied to the COMSOL model, the resulting substrate temperatures deviate from reported values. This discrepancy highlights the need for further calibration of the simulation model, ideally through experimental validation. Furthermore, the inability to perform reactor tests during this project limits the assessment of filament sagging and clamp performance under actual operating conditions.

In conclusion, this thesis lays the groundwork for improving diamond deposition in a scalable HFCVD setup through mechanical design and simulation-based optimization. The developed clamp and digital twin offer promising tools for enhancing film uniformity and diamond deposition times. Future experimental validation will be essential to confirm the simulation findings and fully realize the potential of the proposed improvements.

6.2 Recommendations for future work

Future work on the clamping device. The selected clamping device design has been manufactured and should be experimentally tested in future studies. Several tests could be employed:

- Monitoring filament sagging over time using a fixed set of deposition parameters and a single heated filament.
- Comparing diamond film quality (via Raman spectroscopy and SEM imaging) with and without the new clamp under identical deposition conditions.
- Evaluating the effect of filament array size by testing diamond growth and quality using different numbers of heated filaments (e.g., 1, 2, 3, 4) in combination with the clamp.

Future work on heat distribution simulations. Simulating the HFCVD setup has proven to be a promising technique for optimizing polycrystalline diamond film growth. This short study on simulating the temperature and gas distribution showed a possible improved geometrical configuration for the HFCVD reactor. Due to time constraints and limited proficiency in heat transfer simulation, it was not feasible to provide enough validation and results. For this ultimate goal, several aspects must be improved:

- A practical validation must be done using the starting parameters (Chapter 4.2.1, Table 11). Measuring the substrate temperature with a pyrometer at different spots could be a first step.
- Parameter optimization. Whereas a parametric sweep will provide an overview of the design parameter space, a parameter optimization will provide the optimal parameters. Appendix J shows how parameter optimization can be applied by using COMSOL. For the optimal parameters to make sense, the COMSOL model first needs to be more accurately validated (either experimentally or using literature).

Additionally, the simulation can give insight into several other relevant aspects of the HFCVD reactor which has not been explored in this study yet. Examples include:

- Gas inlet configuration optimization, including variations in size, flow rate, and hydrogen content, to increase gas density above the substrate and potentially enhance diamond growth [53]).
- Non-equidistant filament spacing, which has been shown to improve temperature field uniformity (Shen *et al.* [61]).
- Magnetic field integration, as demonstrated by Kwok et al. [63], to guide ion trajectories and increase reactive radical concentration near the substrate. Future work could investigate the use of SmCo magnets in the PME reactor setup.
- Chemical reaction modeling, such as hydrogen recombination and filament phase changes. Although computationally intensive, incorporating gas-phase and gas-solid reactions [81] would significantly improve simulation fidelity.

References

[1] The Organic Chemistry Tutor. *Structure of Diamond and Graphite, Properties - Basic Introduction*. Nov. 2017. URL: https://www.youtube.com/watch?v=Anu2evOTnBU.

[2] D. Das. "Nanocrystalline Diamond". In: *Carbon-Based Nanofillers and Their Rubber Nanocomposites*. Elsevier, 2019, pp. 123–181. ISBN: 978-0-12-813248-7. DOI: 10.1016/B978-0-12-813248-7.00005-5.

[3] Minichemistry. *File:Diamond structure.png*. Jan. 2014. URL: https://www.minichemistry.com/macromolecules.html5.

[4] M. Sadaghdar. *File:Graphite structure.png*. June 2016. URL: https://www.electroboom.com/?p=835.

[5] R. Nor et al. *Diamond: Synthesis, Characterisation and Applications*. Vol. 5. Springer, Sept. 2010, pp. 195–217. ISBN: 978-3-642-14672-5. DOI: 10.1007/8611_2010_17.

[6] *ANSYS Granta EduPack*. Version 2024 R2. ANSYS Inc. 2024.

[7] U. F. S. D'Haenens-Johansson et al. "Synthesis of Diamonds and Their Identification". In: *Reviews in Mineralogy and Geochemistry* 88.1 (July 2022), pp. 689–753. ISSN: 1529-6466. DOI: 10.2138/rmg.2022.88.13.

[8] K. Muzyka et al. "Boron-doped diamond: current progress and challenges in view of electroanalytical applications". In: *Analytical Methods* 11.4 (2019), pp. 397–414. ISSN: 1759-9660, 1759-9679. DOI: 10.1039/C8AY02197J.

[9] P. W. May et al. "Diamond thin films: a 21st century material. Part 2: a new hope". In: *Philosophical Transactions of the Royal Society A: Mathematical, Physical and Engineering Sciences* (2024). URL: https://www.chm.bris.ac.uk/pt/diamond/preprints/PTRSA-review-preprint.pdf.

[10] R. Haubner. "Low-pressure diamond: from the unbelievable to technical products". In: *ChemTexts* 7.2 (Mar. 2021), p. 10. ISSN: 2199-3793. DOI: 10.1007/s40828-021-00136-z.

[11] P. W. May. "Diamond thin films: a 21st-century material". In: *Philosophical Transactions of the Royal Society A: Mathematical, Physical and Engineering Sciences* 358.1766 (2000), pp. 473–495. DOI: 10.1098/rsta.2000.0533.

[12] Fraunhofer Institute et al. *Windows – XDS Oxford*. URL: https://xds-oxford.com/products/beamline-components/cvd-diamond-windows/.

[13] M. Mermoux et al. "Raman spectroscopy study of detonation nanodiamond". In: *Diamond and Related Materials* 87 (Aug. 2018), pp. 248–260. ISSN: 09259635. DOI: 10.1016/j.diamond.2018.06.001.

[14] S. Kumar et al. "Nanodiamonds: Emerging face of future nanotechnology". In: *Carbon* 143 (Mar. 2019), pp. 678–699. ISSN: 00086223. DOI: 10.1016/j.carbon.2018.11.060.

[15] L. I. Ardhayanti et al. "Purification and tailored functionalities in detonation nanodiamond". In: *Bulletin of the Chemical Society of Japan* 97.9 (Aug. 2024). ISSN: 1348-0634. DOI: 10.1093/bulcsj/uoae089.

[16] R. Balmer et al. “Chemical vapour deposition synthetic diamond: materials, technology and applications”. In: *Journal of Physics: Condensed Matter* 21.36 (Sept. 2009), p. 364221. ISSN: 0953-8984, 1361-648X. DOI: 10.1088/0953-8984/21/36/364221.

[17] M. Frenklach et al. “Growth mechanism of vapor-deposited diamond”. In: *Journal of Materials Research* 3.1 (Feb. 1988), pp. 133–140. ISSN: 0884-2914, 2044-5326. DOI: 10.1557/JMR.1988.0133.

[18] M. Hiramatsu et al. “Radical Density Measurements in Microwave Plasma with Carbon-Containing Gases Used for Carbon Nanotube and Nanocrystalline Diamond Film Growth”. In: *Proceedings of the 20th International Symposium on Plasma Chemistry*. ISPC. 2011. URL: https://www.ispc-conference.org/ispcproc/ispc20/506.pdf.

[19] Y. Ren et al. “Recent progress in homoepitaxial single-crystal diamond growth via MPCVD”. In: *Journal of Materials Science: Materials in Electronics* 35.7 (Mar. 2024), p. 525. ISSN: 0957-4522, 1573-482X. DOI: 10.1007/s10854-024-12267-3.

[20] M. Ashfold et al. “Thin film diamond by chemical vapour deposition methods”. In: *Chemical Society Reviews* 23.1 (1994), p. 21. ISSN: 0306-0012, 1460-4744. DOI: 10.1039/cs9942300021.

[21] S. Ohmagari. “Single-crystal diamond growth by hot-filament CVD: a recent advances for doping, growth rate and defect controls”. In: *Functional Diamond* 3.1 (Dec. 2023). ISSN: 2694-1112, 2694-1120. DOI: 10.1080/26941112.2023.2259941.

[22] S. Ohmagari et al. “Low resistivity p+ diamond (100) films fabricated by hot-filament chemical vapor deposition”. In: *Diamond and Related Materials* 58 (Sept. 2015), pp. 110–114. ISSN: 09259635. DOI: 10.1016/j.diamond.2015.06.011.

[23] T. Tabakoya et al. “High-Rate Growth of Single-Crystalline Diamond (100) Films by Hot-Filament Chemical Vapor Deposition with Tantalum Filaments at 3000 °C”. In: *physica status solidi (a)* 216.21 (Nov. 2019). ISSN: 1862-6300, 1862-6319. DOI: 10.1002/pssa.201900244.

[24] S. H. Din et al. “CVD Diamond”. In: *Transactions of the Indian Institute of Metals* 72.1 (Jan. 2019), pp. 1–9. ISSN: 0972-2815, 0975-1645. DOI: 10.1007/s12666-018-1454-1.

[25] J. Xiang et al. “The Stability of Straightened Ta Filament During Chemical Vapor Deposition of Diamond Film”. In: *physica status solidi (a)* 221.11 (Apr. 2024). DOI: 10.1002/pssa.202300974.

[26] O. Auciello et al. “Review on advances in microcrystalline, nanocrystalline and ultrananocrystalline diamond films-based micro/nano-electromechanical systems technologies”. In: *Journal of Materials Science* 56.12 (Apr. 2021). ISSN: 0022-2461, 1573-4803. DOI: 10.1007/s10853-020-05699-9.

[27] S. Mandal et al., eds. *Novel Aspects of Diamond II: Science and Technology*. Vol. 149. Topics in Applied Physics. Springer Nature Switzerland, 2024. ISBN: 978-3-031-47555-9 978-3-031-47556-6. DOI: 10.1007/978-3-031-47556-6.

[28] O. A. Williams et al. “Growth and Properties of Nanocrystalline Diamond Films”. In: *Physics and Applications of CVD Diamond*. Ed. by S. Koizumi et al. 1st ed. Wiley, Aug. 2008, pp. 13–27. ISBN: 978-3-527-40801-6 978-3-527-62317-4. DOI: 10.1002/9783527623174.ch2.

[29] D. Singh. "Optimization of the hot-filament chemical vapor deposition setup". Master's thesis. Technical University Delft, 2023. URL: https://repository.tudelft.nl/record/uuid:df9ad225-903d-46bf-a027-ee0cf6776978.

[30] J. G. Buijnsters. *Lecture 6 - CVD -2*. Lecture slides, Delft University of Technology. Mar. 2024. URL: https://brightspace.tudelft.nl/d2l/le/content/596801/viewContent/3629253/View.

[31] Tech team Kintek solution. *What is the difference between hot wall CVD and cold wall CVD? 4 Key Differences Explained*. Sept. 2024. URL: https://kindle-tech.com/faqs/what-is-the-difference-between-hot-wall-cvd-and-cold-wall-cvd.

[32] N. Jokerst. *Introduction to pumps*. Dec. 2019. URL: https://www.youtube.com/watch?v=u4wHmW1H6KY.

[33] J. G. Buijnsters. personal communication, 25-11-2024.

[34] G. Malandrino. "Chemical Vapour Deposition. Precursors, Processes and Applications." In: *Angewandte Chemie International Edition* 48.41 (Sept. 2009). DOI: 10.1002/anie.200903570.

[35] P. Mehta Menon et al. "Filament metal contamination and Raman spectra of hot filament chemical vapor deposited diamond films". en. In: *Diamond and Related Materials* 8.1 (Jan. 1999), pp. 101–109. ISSN: 09259635. DOI: 10.1016/S0925-9635(98)00444-0.

[36] F. Jansen et al. "The deposition of diamond films by filament techniques". In: *J. Vac. Sci. Technol. A* 8 (1990). DOI: 10.1116/1.576494.

[37] P. N. Browning et al. "Room and ultrahigh temperature mechanical properties of field assisted sintered tantalum alloys". In: *Materials Science and Engineering: A* 680 (Jan. 2017), pp. 141–151. ISSN: 09215093. DOI: 10.1016/j.msea.2016.09.067.

[38] E. Lassner et al. *Tungsten: Properties, Chemistry, Technology of the Element, Alloys, and Chemical Compounds*. Springer, 1999. ISBN: 978-1-4613-7225-7. DOI: 10.1007/978-1-4615-4907-9.

[39] S. Okoli et al. "Carburization of tungsten and tantalum filaments during low-pressure diamond deposition". In: *Surface and Coatings Technology* 47.1-3 (Aug. 1991), pp. 585–599. ISSN: 02578972. DOI: 10.1016/0257-8972(91)90329-U.

[40] E. Zeiler et al. "Structural changes of tungsten heating filaments during CVD of diamond". In: *Materials Science and Engineering: A* 335.1-2 (Sept. 2002), pp. 236–245. ISSN: 09215093. DOI: 10.1016/S0921-5093(01)01933-5.

[41] T. Tsutsumoto. "Improvement of Ta filament for diamond CVD". In: *Thin Solid Films* 317.1-2 (Apr. 1998), pp. 371–375. ISSN: 00406090. DOI: 10.1016/S0040-6090(97)00626-3.

[42] D.-W. Kweon et al. "The effect of the change in filament characteristics on diamond growth in hot filament chemical vapor deposition". In: *Materials Research Bulletin* 27.6 (June 1992), pp. 783–791. DOI: 10.1016/0025-5408(92)90087-g.

[43] S. Okoli et al. "Influence of the Filament Material on Low-Pressure Hot-Filament CVD Diamond Deposition". In: *Le Journal de Physique IV* 02.C2 (Sept. 1991), pp. C2-923–C2-930. ISSN: 1155-4339. DOI: 10.1051/jp4:19912111.

[44] C.-X. Wang et al. *CN201102987Y - Hot-wire hanging device with constant tension force*. Aug. 2007. URL: https://patents.google.com/patent/CN201102987Y/en.

[45] Y. Shuangli et al. *CN203754804U - Hot-wire tensioning mechanism for chemical vapor deposition diamond equipment*. Feb. 2014. URL: https://patents.google.com/patent/CN203754804U/en?oq=CN203754804U.

[46] Y. Tang et al. *CN110468386B - Hot wire clamp, hot wire deposition equipment, application of hot wire clamp and preparation method of cutter*. May 2018. URL: https://patents.google.com/patent/CN110468386B/en.

[47] Shanghai Zhengshi Technology Co Ltd. *CN112501582A - Hot wire chemical vapor deposition device and metal support*. Nov. 2020. URL: https://patents.google.com/patent/CN112501582A/en.

[48] J. E. Herlinger et al. *US5833753A - Reactor having an array of heating filaments and a filament force regulator*. Dec. 1995. URL: https://patents.google.com/patent/US5833753A/en?oq=US4953499A+(P).

[49] D. Choi et al. "3-D Numerical Simulation and Optical Diagnosis of Temperature Distribution Inside a Chamber of Hot Filament Chemical Vapor Deposition". In: *Applied Science and Convergence Technology* 32.1 (Jan. 2023), pp. 7–11. ISSN: 2288-6559. DOI: 10.5757/ASCT.2023.32.1.7.

[50] C. Wolden et al. "Radiative heat transfer in hot-filament chemical vapor deposition diamond reactors". en. In: *Journal of Applied Physics* 72.8 (Oct. 1992), pp. 3750–3758. DOI: 10.1063/1.352295.

[51] X. Wang et al. "Development of HFCVD apparatus for synthesizing diamond films with low thermal budget". In: *Journal of Cleaner Production* 434 (Dec. 2023), p. 140132. DOI: 10.1016/j.jclepro.2023.140132.

[52] A. F. Mills et al. *Basic heat and mass transfer*. Temporal Publishing, Jan. 2015. ISBN: 978-0-9963053-0-3.

[53] T. Zhang et al. "Simulation of temperature and gas density field distribution in diamond films growth on silicon wafer by hot filament CVD". In: *Journal of Crystal Growth* 343.1 (Jan. 2012), pp. 55–61. DOI: 10.1016/j.jcrysgro.2012.01.005.

[54] Fluid Mechanics Ltd. *Fluid densities and kinemetic viscosities*. 2015. URL: https://www.fluidmechanics.co.uk/wp-content/uploads/2015/01/Fluid-Densities-and-kinematic-Viscosities.pdf.

[55] T. DebRoy et al. "Role of heat transfer and fluid flow in the chemical vapor deposition of diamond". In: *Journal of Applied Physics* 68.5 (Sept. 1990), pp. 2424–2432. DOI: 10.1063/1.346502.

[56] C. Song et al. "Computer Simulation of Temperature Parameter for Diamond Formation by Using Hot-Filament Chemical Vapor Deposition". In: *Coatings* 8.1 (Dec. 2017), p. 15. ISSN: 2079-6412. DOI: 10.3390/coatings8010015.

[57] R. Panickar et al. "Substrate Temperature Optimization for Diamond Thin Film Synthesis using Hot-Filament Chemical Vapor Deposition". In: *2019 8th International Conference on Modeling Simulation and Applied Optimization (ICMSAO)*. Apr. 2019, pp. 1–4. ISBN: 978-1-5386-7684-4.

[58] Y. Wu et al. "Hot filament chemical vapor deposition temperature field optimization for diamond films deposited on silicon nitride substrates". In: *Materials Research Express* 8.11 (Nov. 2021), p. 116403. ISSN: 2053-1591. DOI: 10.1088/2053-1591/ac3278.

[59] C. Hao et al. "A simulation study on the effect of filament spacing on the temperature field uniformity of an HFCVD system". In: *Coatings* 14.10 (Oct. 2024). DOI: 10.3390/coatings14101266.

[60] W. Zuo et al. "Simulation of Substrate Temperature Distribution in Diamond Films Growth on Cemented Carbide Inserts by Hot Filament CVD". In: *Applied Mechanics and Materials* 10-12 (Dec. 2007), pp. 864–868. ISSN: 1662-7482. DOI: 10.4028/www.scientific.net/AMM.10-12.864.

[61] B. Shen et al. "Optimization on the HFCVD setup for the mass-production of diamond-coated micro-tools based on the FVM temperature simulation". In: *Surface and Coatings Technology* 253 (May 2014), pp. 123–131. DOI: 10.1016/j.surfcoat.2014.05.024.

[62] Y. H. Lee et al. "Two-dimensional computational fluid dynamics modeling of slip-flow heat transfer in the hot filament chemical vapor deposition process". In: *Surface and Coatings Technology* 456 (Mar. 2023), p. 129291. ISSN: 02578972. DOI: 10.1016/j.surfcoat.2023.129291.

[63] F. M. Kwok et al. "Fabrication of diamond film under low methane concentration by hot filament chemical vapor deposition with magnetic field assistance". In: *Surface and Coatings Technology* 483 (Apr. 2024), p. 130802. DOI: 10.1016/j.surfcoat.2024.130802.

[64] Y. Ruan et al. *Optimizing Temperature Distribution for High-Throughput Diamond Coating on Tools Via Hot-Filament Chemical Vapor Deposition*. Preprint, https://www.ssrn.com/abstract=4847399. 2024. DOI: 10.2139/ssrn.4847399.

[65] ProductPlan. *What is MoSCoW Prioritization? — Overview of the MoSCoW Method*. Nov. 2024. URL: https://www.productplan.com/glossary/moscow-prioritization/.

[66] Aura design. *Nitinol - FAQ - Smart Wires*. n.d. URL: https://smartwires.eu/index.php?id_cms=9&controller=cms&id_lang=1#:~:text=Nitinol%20comes%20in%20many%20activation,and%20collected%20in%20small%20domains..

[67] H. Fritze. "High-temperature piezoelectric crystals and devices". In: *Journal of Electroceramics* 26.1-4 (Apr. 2011), pp. 122–161. DOI: 10.1007/s10832-011-9639-6. URL: https://doi.org/10.1007/s10832-011-9639-6.

[68] S. Ali et al. *Review in thermal effects on the performance of electric motors*. 2016. DOI: 10.1109/INTELSE.2016.7475166.

[69] J. Pasko. *The role of temperature control in hydraulic oil reliability*. Apr. 2023. URL: https://precisionlubrication.com/articles/temperature-hydraulic-oil/#:~:text=Hydraulic%20oil%20starts%20breaking%20down,as%20per%20the%20Arrhenius%20equation..

[70] E. R. Tajne. *Tungsten filament lamp construction; its working principle — Incandescent*. Apr. 2022. URL: https://omgfreestudy.com/illumination/.

[71] Dassault Systèmes. *SolidWorks Simulation*. Version 2024. June 10, 2023. URL: https://www.solidworks.com/product/solidworks-simulation.

[72] T. Matsumoto et al. "Hemispherical total emissivity of niobium, molybdenum, and tungsten at high temperatures using a combined transient and brief Steady-State technique". In: *International Journal of Thermophysics* 20.3 (Jan. 1999), pp. 943–952. DOI: 10.1023/a:1022699622719.

[73] B. He et al. “Influence of roughness and temperature on the emissivity of molybdenum in RTPV system”. In: *Materials Today Communications* 40 (Aug. 2024), p. 110102. DOI: 10.1016/j.mtcomm.2024.110102.

[74] J. M. Mayer et al. “Temperature-dependent diffuse reflectance measurements of ceramic powders in the near- and mid-infrared spectra”. In: *Solar Energy* 245 (Sept. 2022), pp. 193–210. DOI: 10.1016/j.solener.2022.08.071. URL: https://doi.org/10.1016/j.solener.2022.08.071.

[75] Gimex. *Gimex: Advanced Materials Solutions*. 2025. URL: https://www.gimex.com.

[76] COMSOL Inc. *COMSOL Multiphysics*. Version 6.1. Nov. 1, 2022. URL: https://www.comsol.com/release/6.1.

[77] F. M. White. “Differential Relations for Fluid Flow”. In: *Fluid Mechanics*. 8th ed. McGraw-Hill Education, 2016. Chap. 4, pp. 117–166. ISBN: 978-9-814-72017-5.

[78] Y. Wu et al. “Hot filament chemical vapor deposition temperature field optimization for diamond films deposited on silicon nitride substrates”. In: *Materials Research Express* 8.11 (Oct. 2021), p. 116403. DOI: 10.1088/2053-1591/ac3278.

[79] *COMSOL Multiphysics Materials Library*. Version 6.1. COMSOL Inc., Nov. 1, 2022. URL: https://www.comsol.com/material-library.

[80] V. S. van Merrienboer. “Development of a 1000C-capable LED-based RTP Reactor - Design and Optimisation Study of an 88kW LED Heater Array for Uniform and Rapid Thermal Processing of 300mm Silicon Wafers”. Master’s thesis. Technical University Delft, 2024. URL: https://repository.tudelft.nl/record/uuid:4901ef64-91c1-4b84-a70c-fab397032275.

[81] J. G. Buijnsters. “Hot-filament Chemical Vapour Deposition of Diamond onto Steel Substrates”. Doctoral thesis. Radboud University Nijmegen, 2003. URL: https://repository.ubn.ru.nl/bitstream/handle/2066/19264/19264_hotfchvad.pdf.

[82] P. Y. Papalambros et al. *Principles of optimal design*. Cambridge University Press, Jan. 2017. DOI: 10.1017/9781316451038.

A Properties of various forms of diamond

This table gives a quantitative representation of Section 2.1.5, in which the different forms of diamond are presented.

Material	Density (g/cm^3)	Hardness (GPa)	Young's modulus (GPa)	sp^3-C (%)	H content (at%)	Band gap (eV)	Surface Roughness (nm)
SCD	3.52	100	1050–1200	100	< 0.1	5.45	–
MCD (grain size $\sim$ 0.5–10 μm)	3.52	70–100	800–1200	~ 100	< 1	5.45	400 - 1000
NCD (grain size 50–100 nm)	3.50–3.75	30–75	800–1020	> 50	< 1	2–4.7	50–100
UNCD (grain size $\sim$ 3–5 nm)	3.50	88–98	916–980	95–98	< 1	5.4–5.65	20–40

Table 17: Properties of various forms of diamond (modified from Auciello *et al.* [26]).

B Design option tree

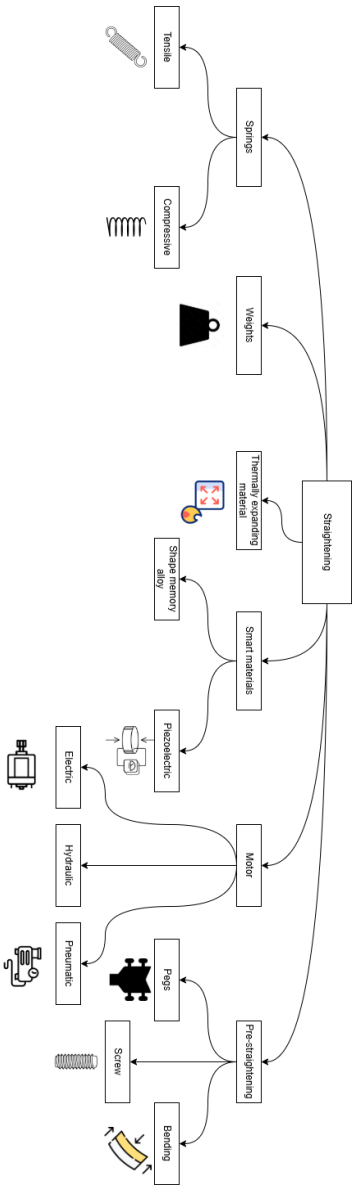

Figure 61: Design option tree straightening subsystem

C Clamping mechanism overview

Patent number / Author	*Type*	*Complexity*	*Applied force*	*Notes*	*Year*
Current clamp	No tension	1	0	Best performance when both sides are free	2018
Singh	Weights	2	?	Uses counterweight and lever, has not been tested	2023
Xiang	Weights	?	3.7-9.5 N	No image present	2024
Takahiro	Weights	1	0.1 N	Relatively simple drawing of counterweights	1998
CN201102987Y	Weights	2	?	Minimizes friction with moving electrode	2007
CN112501582A	Weights	2	?	Minimizes friction with diamond groove	2020
CN203754804U	Springs	2	?	Tension springs with movable electrode	2014
CN110468386B	Springs	2	?	Compression springs with movable electrode	2018
US4953499A	Pegs	3	?	Uses jig that tensions filament by inserting pegs	1990
US5833753A	Springs	2	0.1 ounce	Movable electrode attached to spring and adjustable screw	1996
JP2020041182A	Motor	3	?	Uses gears to transmit motor force into vacuum chamber	2019
CN108505019B	Springs	2	?	Variation using compression springs	2018
US4970986	Springs	2	?	Tension springs with movable electrode, one for each filament	1990
CN103834930A	Springs	2	?	30 degree angled tensioning springs	2013
CN110938810B	Weight and spring	2	?	Uses sliding Molybdenum weight block connected to spring	2024
CN102140626A	Spring	3	?	Tensions zigzag pattern of hot filament using several springs	2011

Patent number / Author	*Link*
Current clamp	https://repository.tudelft.nl/record/uuid:df9ad225-903d-46bf-a027-ee0cf6776978
Singh	https://repository.tudelft.nl/record/uuid:df9ad225-903d-46bf-a027-ee0cf6776978
Xiang	https://onlinelibrary.wiley.com/doi/10.1002/pssa.202300974
Takahiro	https://www.sciencedirect.com/science/article/pii/S0040609097006263
CN201102987Y	https://patents.google.com/patent/CN201102987Y/en?oq=CN201102987Y
CN112501582A	https://patents.google.com/patent/CN112501582A/en?oq=CN112501582A
CN203754804U	https://patents.google.com/patent/CN203754804U/en?oq=CN203754804U
CN110468386B	https://patents.google.com/patent/CN110468386B/en?oq=CN110468386B
US4953499A	https://patents.google.com/patent/US4953499A/en?oq=US4953499A
US5833753A	https://patents.google.com/patent/US5833753A/en?oq=US5833753A
JP2020041182A	https://patents.google.com/patent/JP2020041182A/en?oq=JP2020041182A
CN108505019B	https://patents.google.com/patent/CN108505019B/en?oq=CN108505019B
US4970986	https://patents.google.com/patent/US4970986A/en?oq=US4970986
CN103834930A	https://patents.google.com/patent/CN103834930A/en?oq=US4970986
CN110938810B	https://patents.google.com/patent/CN110938810B/en?oq=US4970986
CN102140626A	https://patents.google.com/patent/CN102140626A/en?oq=US4970986

D Spring stifness calculation

```
% Required force tantalum filament (Xiang et al 2024)
% Required force tungsten filament is not known yet

Sigma = 7.7e6; % [MPa]
D_filament = 0.5e-3; % [m]
A_filament = (pi/4)*D_filament^2; % [m^2]
F = Sigma * A_filament; % [N]
n_f = 3; % number of filament used
n_s = 2;% number of springs used
n = n_f/n_s;
F_t = F*n;

disp(['The total required force is ', num2str(F_t), ' [N]']);

% Spring stiffness calculation
l_filament = 0.11; % [m]
delta = 0.2; % filament expansion [%]. Find study exact one
x = l_filament*delta; % required spring displacement [m]
k = F_t / x; % spring stiffness [N/m]

disp(['The spring stiffness is ', num2str(k), ' [N/m]']);
```

Listing 1: Spring Specifications Calculation

E Modeling in COMSOL Multiphysics

This appendix section explains how the COMSOL model of the PME reactor setup from this study can be replicated.

Modeling instructions

From the **File** menu, choose **New**

NEW

In the **New** window, click **Model Wizard.**

MODEL WIZARD

1. In the **Model Wizard** window, click **3D.**
2. In the Select Physics tree, select **Heat transfer** > **Conjugate Heat Transfer** > **Laminar Flow.**
3. Click **Add.**
4. Click **Study.**
5. In the **Select Study** tree, select **General Studies** > **Stationary.**
6. Click **Done.**

GEOMETRY

The geometry sequence for the model is available in a file. If you want to create it from scratch yourself, you can follow the tutorial in Appendix F. Otherwise, insert the geometry sequence as follow:

1. In the **Geometry** toolbar, click **Insert Sequence** and choose **Insert Sequence**.
2. Browse to the model's **Application Libraries** folder and double-click the file `HFCVD_reactor_geom_sequence.mph`.
3. In the **Geometry** toolbar, click **Build All**.
   The imported sequence contains all required selections in addition to the actual geometry. Selections facilitate the work of assigning materials, setting boundary conditions, and plotting the results.
4. Click the **Zoom Extents** button in the **Graphics** toolbar. You should now see the geometry shown in **Figure 41**.

GLOBAL DEFINITIONS

Parameters 1

1. In the **Model Builder** window, under **Global Definitions** click **Parameters 1.**
2. In the **Settings** window for **Parameters**, locate the **Parameters** section.
3. In the table, enter the following settings:

Name	Expression	Value	Description
T_f	2200[degC]	2473.15 K	Filament temperature
T_{amb}	25[degC]	298.15 K	Ambient temperature
P	10[kPa]	10000 Pa	Pressure
U_0	0.1[m/s]	0.1 m/s	Inlet velocity
r	0.5[mm]	0.0005 m	Radius
H	8[mm]	0.008 m	Height
D	16[mm]	0.016 m	Diameter

LAMINAR FLOW (SPF)

1. In the **Model Builder** window, under Component 1 click **Laminar Flow (spf).**
2. In the **Settings** window for **Laminar Flow**, locate the **Domain Selection** section.
3. From the **Selection** list, choose **Hydrogen.**

HEAT TRANSFER IN SOLIDS AND FLUIDS (HT)

1. In the **Model Builder** window, under Component 1 click **Laminar Flow (spf).**
2. In the **Settings** window for **Laminar Flow**, locate the **Domain Selection** section.
3. From the **Selection** list, choose **Hydrogen.**

Fluid 1

1. In the **Model Builder** window, under **Component 1 > Heat Transfer in Solids and Fluids (ht)** click **Fluid 1**.
2. In the **Settings** window for **Fluid**, locate the **Domain Selection** section
3. From the **Selection** list, choose **Hydrogen.**

ADD MATERIAL

1. In the **Home** toolbar, click **Add Material** to open the **Add Material** window.
2. Go to the **Add Material** window.
3. In the tree, select **Built-in>Tungsten.**
4. Click **Add to Component** in the window toolbar.

5. In the tree, select **Built-in>Steel AISI 4340.**
6. Click **Add to Component** in the window toolbar.
7. In the tree, select **Built-in>Silicon.**
8. Click **Add to Component** in the window toolbar.
9. In the tree, select **Material library>SiC (6H) Siliconcarbide.**
10. Click **Add to Component** in the window toolbar.
11. In the tree, select **Material library>Hydrogen (Gas).**
12. Click **Add to Component** in the window toolbar.

MATERIALS

Tungsten (mat1)

1. In the **Model Builder window**, under **Component I>Materials** click **Tungsten (mat1.)**
2. In the **Settings** window for **Material**, locate the **Geometric Entity Selection** section.
3. From the **Selection** list, choose **Tungsten**

Steel AISI 4340 (mat2)

1. In the **Model Builder window**, under **Component I>Materials** click **Steel AISI 4340 (mat2.)**
2. In the **Settings** window for **Material**, locate the **Geometric Entity Selection** section.
3. From the **Selection** list, choose **Steel**

Silicon (mat3)

1. In the **Model Builder window**, under **Component I>Materials** click **Silicon (mat3).**
2. In the **Settings** window for **Material**, locate the **Geometric Entity Selection** section.
3. From the **Selection** list, choose **Silicon**

SiC (6H) Siliconcarbide (mat4)

1. In the **Model Builder window**, under **Component I>Materials** click **SiC (6H) Siliconcarbide (mat4.)**
2. In the **Settings** window for **Material**, locate the **Geometric Entity Selection** section.
3. From the **Selection** list, choose **SiC**

Hydrogen (gas) (mat5)

1. In the **Model Builder window**, under **Component I>Materials** click **Hydrogen (gas) (mat5)**
2. In the **Settings** window for **Material**, locate the **Geometric Entity Selection** section.
3. From the **Selection** list, choose **Hydrogen**

LAMINAR FLOW (SPF)

The no-slip condition is the default boundary condition for the fluid. Define the inlet and outlet conditions as described below.

1. In the **Model Builder** window, under **Component 1 (comp1)** click **Laminar Flow (spf).**

Inlet 1

1. In the **Physics** tooblar, click **Boundaries** and choose **Inlet.**
2. In the **Settings** window for **Inlet**, locate the **Boundary Selection** section.
3. From the **Selection** list, choose **Inlet.**
4. Locate the **Boundary Condition** section. From the list, choose **Fully developed flow.**
5. Locate the **Fully Developed Flow** secion. In the U_{av} text field, type 1 [m/s].

Outlet 1

1. In the **Physics** tooblar, click **Boundaries** and choose **Outlet.**
2. In the **Settings** window for **Inlet**, locate the **Boundary Selection** section.
3. From the **Selection** list, choose **Outlet.**

HEAT TRANSFER IN SOLIDS AND FLUIDS (HT)

Thermal insulation is the default boundary condition for the temperature. Define the inlet temperature and the outlet condition as described below.

1. In the **Model Builder** window, under **Component 1 (comp1)** click **Heat Transfer in Solids and Fluids (ht).**

Inflow 1

1. In the **Physics** toolbar, click **Boundaries** and choose **Inflow.**
2. In the **Settings** window for **Inlet**, locate the **Boundary Selection** section.
3. From the **Selection** list, choose **Inlet.**

Outflow 1

1. In the **Physics** toolbar, click **Boundaries** and choose **Outflow.**
2. In the **Settings** window for **Inlet**, locate the **Boundary Selection** section.

3. From the **Selection** list, choose **Outlet.**

Heat Source 1

1. In the **Physics** toolbar, click **Domains** and choose **Heat source.**
2. In the **Settings** window for **Inlet**, locate the **Domain Selection** section.
3. From the **Selection** list, choose **Substrate holder.**
4. Locate the **Heat Source** section. From the **Heat source** list, choose **Heat rate.**
5. In the P_0 text field, type P0

Temperature 1

1. In the **Physics** toolbar, click **Domains** and choose **Temperature.**
2. In the **Settings** window for **Temperature**, locate the **Boundary Selection** section.
3. From the **Selection** list, choose **Heated filament (boundaries)**
4. Locate the **Temperature** section.
5. In the T_0 text field, type Tf

Temperature 2

1. In the **Physics** toolbar, click **Domains** and choose **Temperature.**
2. In the **Settings** window for **Temperature**, locate the **Boundary Selection** section.
3. From the **Selection** list, choose **Steel walls (boundaries)**
4. Locate the **Temperature** section.
5. In the T_0 text field, type Tamb

ADD PHYSICS

1. In the **Physics** toolbar, click **Add Physics** window.
2. Go to the **Add Physics** window.
3. In the tree, select **Heat transfer** > **Radiation** > **Surface-to-Surface Radiation (rad).**
4. Click the **Add to Component 1** button in the window toolbar.
5. In the **Physics** toolbar, click **Add Physics** to close the **Add Physics** window.

SURFACE-TO-SURFACE RADIATION (RAD)

1. In the **Settings** window for **Surface-to-Surface Radiation**, locate the **Boundary Selection section.**
2. From the **Selection** list, choose **Exterior Walls**

Materials

For the material boundaries, emissivity values have to be defined manually.

Tungsten (Boundaries)

1. In the **Materials** toolbar, click **Blank Material**.
2. In the **Settings** window for **Material**, type **Tungsten (Boundaries)** in the **Label** text field.
3. Locate the **Geometric Entity Selection** section. From the **Geometric entity level** list, choose **Boundary**.
4. From the **Selection** list, choose **Tungsten Boundaries**.
5. Locate the **Material Contents** section. In the table, enter the following settings:

Property	Variable	Value	Unit	Property group
Surface emissivity	epsilon_rad	0.4	1	Basic

Silicon (Boundaries)

1. In the **Materials** toolbar, click **Blank Material**.
2. In the **Settings** window for **Material**, type **Silicon (Boundaries)** in the **Label** text field.
3. Locate the **Geometric Entity Selection** section. From the **Geometric entity level** list, choose **Boundary**.
4. From the **Selection** list, choose **Silicon Boundaries**.
5. Locate the **Material Contents** section. In the table, enter the following settings:

Property	Variable	Value	Unit	Property group
Surface emissivity	epsilon_rad	0.6	1	Basic

SiC (Boundaries)

1. In the **Materials** toolbar, click **Blank Material**.
2. In the **Settings** window for **Material**, type **SiC (Boundaries)** in the **Label** text field.
3. Locate the **Geometric Entity Selection** section. From the **Geometric entity level** list, choose **Boundary**.
4. From the **Selection** list, choose **SiC Boundaries**.
5. Locate the **Material Contents** section. In the table, enter the following settings:

Property	Variable	Value	Unit	Property group
Surface emissivity	epsilon_rad	0.9	1	Basic

Steel (Boundaries)

1. In the **Materials** toolbar, click **Blank Material**.
2. In the **Settings** window for **Material**, type **Steel (Boundaries)** in the **Label** text field.

3. Locate the **Geometric Entity Selection** section. From the **Geometric entity level** list, choose **Boundary**.
4. From the **Selection** list, choose **Steel Boundaries**.
5. Locate the **Material Contents** section. In the table, enter the following settings:

Property	Variable	Value	Unit	Property group
Surface emissivity	epsilon_rad	0.7	1	Basic

Diffuse Surface 1

1. In the **Model Builder** window, under **Component 1 (comp1)** > **Surface-to-Surface Radiation**, locate the **Boundary Selection** section.
2. In the **Settings** window for **Diffuse surface**, locate the **Ambient** section.
3. In the T_{amb} section, type Tamb.

Opacity 1

1. In the **Physics** toolbar, click **Domains** and choose **Opacity**.
2. In the **Settings** window for **Opacity**, locate the **Domain Selection** section.
3. From the **Selection** list, choose **All voids**.

MESH 1

1. In the **Model Builder** window, under **Component 1 (comp1) click Mesh 1**
2. In the **Settings** window for **Mesh**, locate the **Physics-Controlled Mesh** section.
3. From the **Element size** list, choose **Fine.**
4. Click **Build all**

F Geometry

Geometry modeling instructions

If you want to create the geometry yourself, follow these steps.

ADD COMPONENT

In the **Home** toolbar, click **Add Component** and choose **3D.**

GEOMETRY 1

1. In the **Settings** window for **Geometry**, locate the **Units** section.
2. From the **Length unit** list, choose **mm.**

Substrate holder

1. In the **Model Builder** window, under **Component 1 (comp1)**, right click **Geometry 1**
2. click on the **Cylinder**
3. In the **Settings** window for **Cylinder**, locate the **Size and Shape** section.
4. In the **Radius** window, fill in **38.1 mm.**
5. In the **Height** window, fill in **109 mm.**
6. **Label** the cylinder as: **Substrate holder.**

Ceramic toplayer

1. In the **Model Builder** window, under **Component 1 (comp1)**, right click **Geometry 1**
2. click on the **Cylinder**
3. In the **Settings** window for **Cylinder**, locate the **Size and Shape** section.
4. In the **Radius** window, fill in **37.6 mm.**
5. In the **Height** window, fill in **1 mm.**
6. In the **Settings** window for **Cylinder**, locate the **Position** section.
7. In the **z** window, fil in **109 mm.**
8. **Label** the cylinder as: **Ceramic toplayer.**

Silicon wafer

1. In the **Model Builder** window, under **Component 1 (comp1)**, right click **Geometry 1**
2. click on the **Cylinder**

3. In the **Settings** window for **Cylinder**, locate the **Size and Shape** section.
4. In the **Radius** window, fill in **25.4**
5. In the **Height** window, fill in **1 mm.**
6. In the **Settings** window for **Cylinder**, locate the **Position** section.
7. In the **z** window, fill in **110 mm.**
8. **Label** the cylinder as: **Silicon wafer.**

Filament 1

1. In the **Model Builder** window, under **Component 1 (comp1)**, right click **Geometry 1**
2. click on the **Cylinder**
3. In the **Settings** window for **Cylinder**, locate the **Size and Shape** section.
4. In the **Radius** window, fill in **r**
5. In the **Height** window, fill in **70 mm.**
6. In the **Settings** window for **Cylinder**, locate the **Position** section.
7. In the **x** window, fill in **-3*D**
8. In the **y** window, fill in **-35**
9. In the **z** window, fill in **111+H**
10. In the **Settings** window for **Cylinder**, locate the **Axis** section.
11. In the **Axis type** window, choose **y-axis**
12. **Label** the cylinder as: **Filament 1.**

Repeat this process for Filament 2-7, vary the **x** window setting, with consequently -2*D,-1*D,0,D,2*D,3*D.

Reactor walls

1. In the **Model Builder** window, under **Component 1 (comp1)**, right click **Geometry 1**
2. click on the **Block**
3. In the **Settings** window for **Block**, locate the **Size and Shape** section.
4. In the **Width** window, fill in **188 mm.**
5. In the **Depth** window, fill in **188 mm.**
6. In the **Height** window, fill in **188 mm.**
7. In the **Settings** window for **Block**, locate the **Position** section.
8. In the **z** window, fill in **94 mm.**

9. **Label** the block as: **Reactor walls.**

Inlet

1. In the **Model Builder** window, under **Component 1 (comp1)**, right click **Geometry 1**
2. click on the **Cylinder**
3. In the **Settings** window for **Cylinder**, locate the **Size and Shape** section.
4. In the **Radius** window, fill in **3 mm.**
5. In the **Height** window, fill in **3 mm.**
6. In the **Settings** window for **Cylinder**, locate the **Position** section.
7. In the **z** window, fill in **185 mm.**
8. **Label** the cylinder as: **Inlet.**

Outlet

1. In the **Model Builder** window, under **Component 1 (comp1)**, right click **Geometry 1**
2. click on the **Cylinder**
3. In the **Settings** window for **Cylinder**, locate the **Size and Shape** section.
4. In the **Radius** window, fill in **50 mm.**
5. In the **Height** window, fill in **20 mm.**
6. **Label** the cylinder as: **Outlet.**

G Icons

This part of the appendix gives a brief explanation on the different icons accompanied by several figures in the report. Figure 62 shows the logo that is featured in figures from the study by Wang *et al.* [51], which was used for replication, while Figure 62 (b) represents the results of the present study on the PME HFCVD reactor.

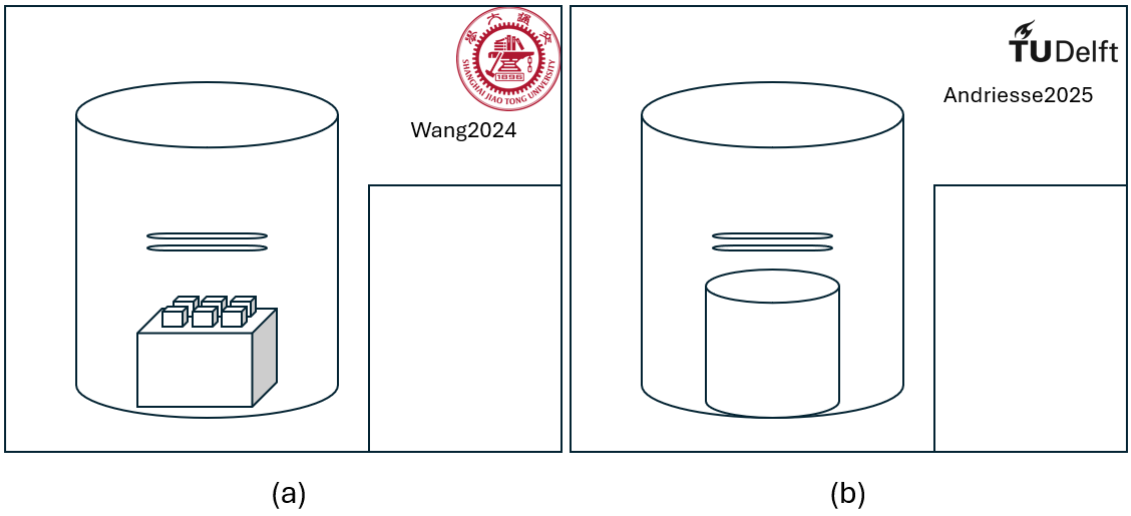

Figure 62: Visual icons of replication studies: (a) Wang *et al.* [51] and (b) the present study, which is referred to as Andriesse (2025)

The lower right corner features a blank rectangle in Figure 62. Herein, the view (i.e. directionality of sight) is mentioned. For example, Figure 63 displays a side view plot.

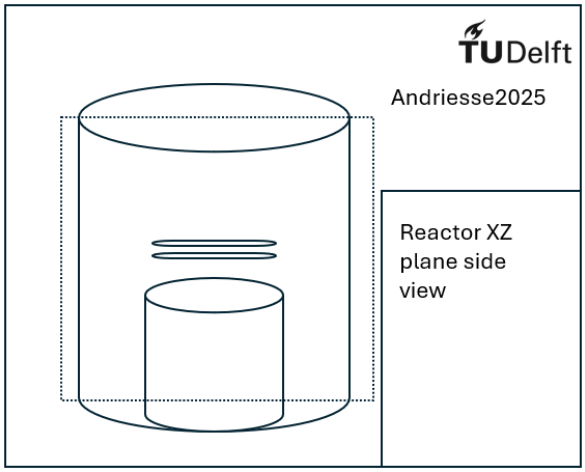

Figure 63: Icon of a side view plot along the XZ plane

H Heater stage

The real geometry of the heater stage is shown in Figure 64.

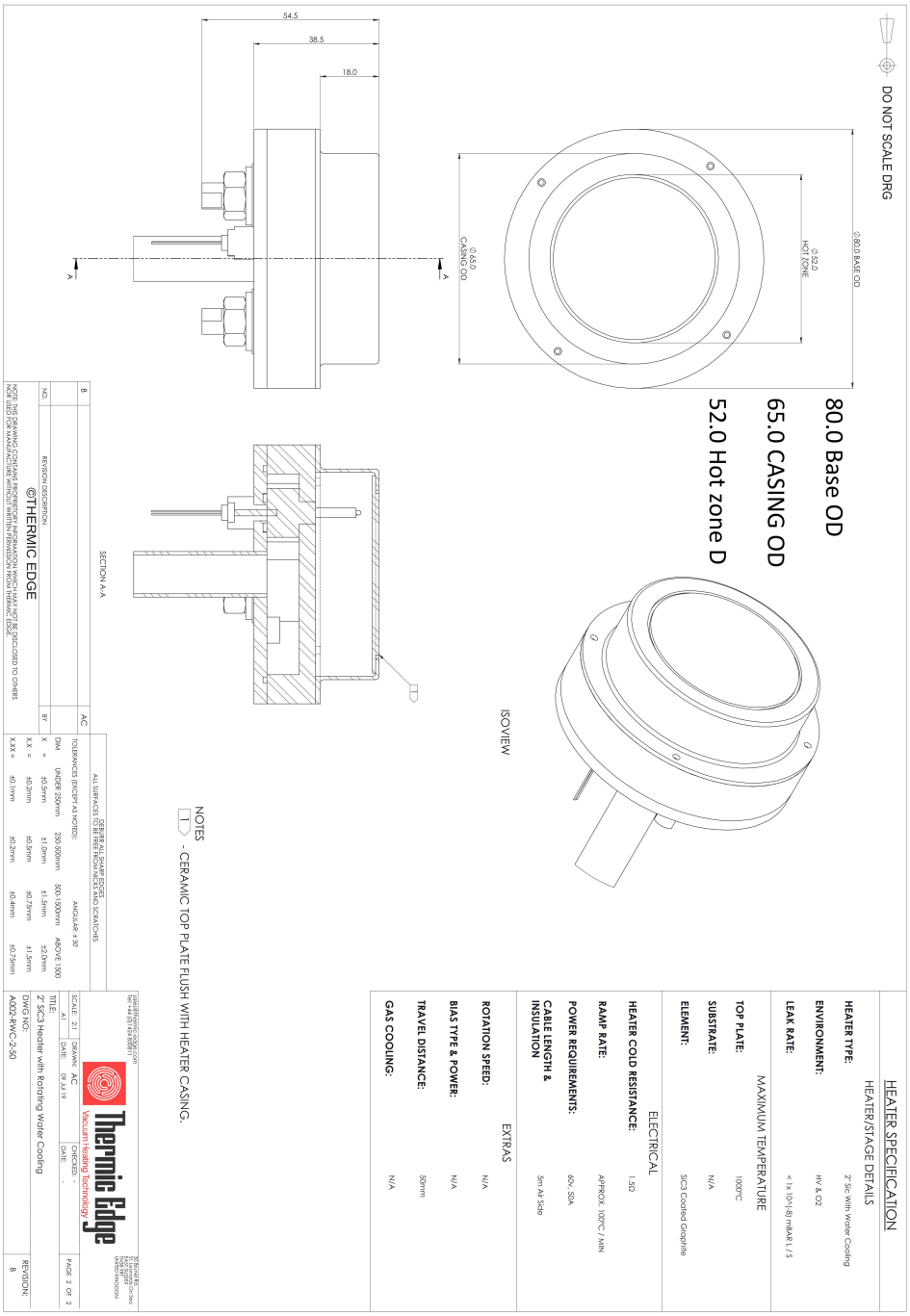

Figure 64: Schematic drawing heater stage

I Sagging measurement

The sagging geometry is measured using PowerPoint. Figures from the MSc thesis of Dilpreet Singh [29] were used. By drawing lines in PowerPoint, the distance in Powerpoint is shown in the upper right corner of the screen. The filament-substrate distance of a straight filament is known as 8 mm, using this, a scale for the image can be obtained. From this, a distance 'x' can be calculated. This distance can then be used to create a geometry of the sagged filament in COMSOL.

Distance	Sagging filament	Straight Filament - Substrate (H)
Size in PPT (cm)	2.73	4.67
Length in reality (mm)	x	8

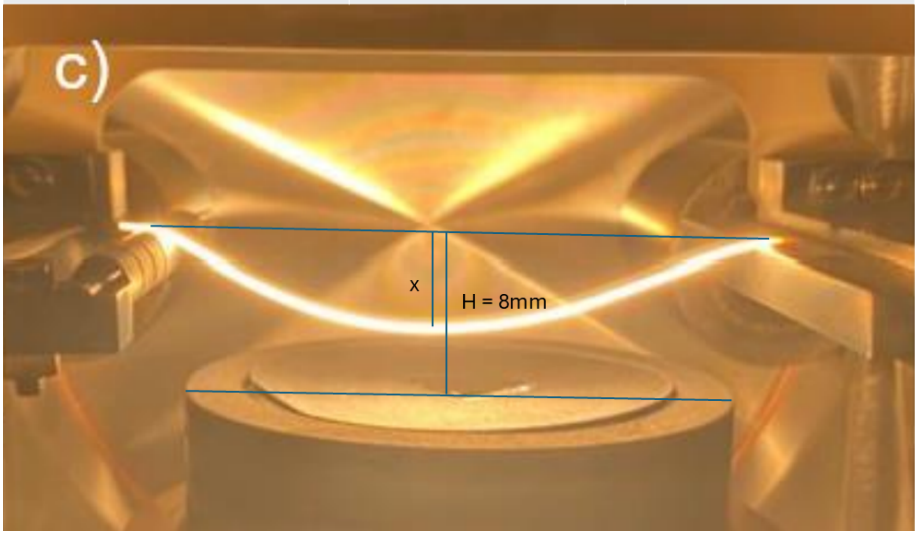

After 148 hours
x ≈ 4.67 mm

Figure 65: Sagging measurement in PowerPoint

J Design optimization

Design optimization is a standard concept in engineering which utilizes mathematical decision-making methods. The benefit over parametric sweeps is that this method can target specific performance. In the case of the HFCVD reactor, an even substrate temperature of around 800 °C is desired. Palambros *et al.* [82] described a quantitative method to define this problem.

J.1 The optimization problem

The design variables are:

$$\mathbf{x} = \begin{bmatrix} H \\ r \\ P \\ D \end{bmatrix} \tag{15}$$

In which H is the filament-substrate distance, r is the filament radius, P is the power supplied to the heater stage, and D is the filament-filament distance.

The objective function aims to get the substrate temperature to 800 °C, while maintaining a minimal variation in temperature over the substrate surface. For this, two objective functions have to be combined. One for minimizing the difference between the actual temperature and the objective temperature, and the other for minimizing the variance. This leads to the following objective function:

$$f(\mathbf{x}) = \alpha \left(T_{\text{avg}}(\mathbf{x}) - 800\right)^2 + \beta \int_A \left(T(\mathbf{x}, \mathbf{r}) - T_{\text{avg}}(\mathbf{x})\right)^2 \, dA \tag{16}$$

where:

- α, β are weighting coefficients
- A is the surface area
- T_{avg} is the average temperature of the substrate surface
- $T(\mathbf{x}, \mathbf{r})$ is the temperature of a location on the substrate surface, dependent on the radius and x coordinate,

The full optimization problem can be written as:

$$\begin{aligned} \underset{\mathbf{x}}{\text{minimize}} \quad & f(\mathbf{x}) = \alpha \left(T_{\text{avg}}(\mathbf{x}) - 800\right)^2 + \beta \int_A \left(T(\mathbf{x}, \mathbf{r}) - T_{\text{avg}}(\mathbf{x})\right)^2 \, dA \\ \text{subject to} \quad & H_{\min} \leq H \leq H_{\max}, \\ & R_{\min} \leq R \leq R_{\max}, \\ & D_{\min} \leq D \leq D_{\max}, \\ & P_{\min} \leq P \leq P_{\max}. \end{aligned} \tag{17}$$

J.2 COMSOL optimization

This part will explain how to setup the optimization problem in COMSOL. For the arbitrary α, and β are set to 1. Now define the $H_{\min}$, $H_{\max}$, $R_{\min}$, $R_{\max}$, $D_{\min}$, $D_{\max}$, $P_{\min}$, and $P_{\max}$. Do this by plugging the desired values under Geometrical Definitions → Parameters.

After this, T_{avg} has to be defined. This is done by adding an average operator to the substrate surface. Go to Component → Definitions → Average, and name it aveop1. To get the average temperature over the silicon substrate, select the substrate top surface boundary.
To get the integral over the surface, necessary for the variance, go to Component → Definitions → Integration, and name it intop1.
For the continuously updated boundary probe, go to Component → Definitions → Probes → Boundary probe, select the silicon substrate surface boundary.

All the variables needed are now defined for optimization. To get to the optimization module, go to Study → Optimization. Fill in the formulas shown in Table 18, which correspond to the formulas in Section J.1:

Table 18: Objective function in COMSOL

Expression	**Description**
`comp1.intop1((T - comp1.aveop1(T))^2)`	variance
`(comp1.dom1 - 800)^2`	temperature to 800

The software will now try to minimize the sum of these objective functions by varying the defined control variables (such as r,D,H,P) and try to find an optimized set of geometrical parameters. For this study, it has not been performed yet, because the model in Section 5.2 has not been validated successfully.
If parameter optimization is applied successfully, this could lead to a second version of the new clamp, with the hot filaments spaced at the optimal geometrical configuration. This version will be able to minimize hot filament sagging while also improving diamond quality.